# Quantum transport in nanostructures

From the effects of decoherence on localization to
magnetotransport in two-dimensional electron systems

Von der Fakultät für Physik
der Universität Duisburg-Essen
genehmigte Dissertation
zur Erlangung des Grades
Dr. rer. nat.
von

Thomas Stegmann
aus Bottrop

The cover image shows Hofstadter's butterfly and has been awarded as the best scientific image of the CENIDE photo contest 2012. The physical meaning of this image is discussed in Chapter 5 of this thesis.

Summary

In this thesis, quantum transport in nanostructures is studied theoretically by means of the nonequilibrium Green's function (NEGF) method. Starting with coherent systems, we discuss ballistic transport and conductance quantization in homogeneous tight-binding lattices. We show that disorder gives rise to transmission resonances. A short introduction to Anderson localization is given and a compact analytical formula for the disorder averaged resistance is derived by means of generating functions.

Transport in nanostructures generally takes place in an intermediate regime between quantum and classical transport due to decoherence. We study the effects of decoherence on electron transport by a statistical model. The essential idea of our model is to distribute spatially over the system decoherence regions, where phase and momentum of the electrons are randomized completely. The transport in between these regions is assumed as phase coherent. Afterwards, the transport quantity of interest is ensemble averaged over spatial decoherence configurations, which are generated according to a given distribution function. We discuss how homogeneous tight-binding lattices are driven by decoherence from the quantum-ballistic to the classical-Ohmic regime. We show that the transport through disordered tight-binding lattices is affected significantly by the spatial distribution of the decoherence regions. If the decoherence is homogeneously distributed, Ohmic conduction is found for any finite degree of decoherence. In contrast, for randomly distributed decoherence, we find an insulator-metal transition from the localized to the Ohmic regime at a critical degree of decoherence, which corresponds to a critical phase coherence length. We also discuss how transport in disordered tight-binding lattices can be enhanced by decoherence. The decoherence model is extended to obtain pure dephasing. We show that transmission resonances are suppressed by pure dephasing, but the average transmission is conserved. The insulator-metal transition is independent of whether phase randomization goes along with momentum randomization or not.

Magnetotransport in two-dimensional electron systems is considered. We study how electrons, coherently injected at one point on the boundary of a two-dimensional electron gas (2DEG), are focused by a perpendicular magnetic field onto another point of that boundary. At weak magnetic field, the generalized 4-point Hall resistance shows equidistant peaks, which can be explained by classical cyclotron motion. When the magnetic field is increased, we observe anomalous resistance oscillations superimposed upon the quantum Hall plateaus. We show that all resistance oscillations can be explained by the interference of the occupied edge channels. The anomalous oscillations are beatings, which appear when only some few edge channels are occupied. By introducing decoherence and partially diffusive boundary scattering, we show that this effect is quite robust. The resistance oscillations can be observed not only in a nonrelativistic 2DEG, but also in the relativistic 2DEG found in graphene. We also report a finite current at armchair edges of graphene ribbons, which is not present at zigzag edges. This edge current can be traced back to the fact that at armchair edges carbon atoms of both graphene sublattices are present, whereas at zigzag edges only atoms of one sublattice appear. The thesis is concluded with some notes on Hofstadter's butterfly shown on the cover page.

Zusammenfassung

In dieser Dissertation wird Quantentransport in Nanostrukturen mit Hilfe der Methode der Nichtgleichgewichts-Green-Funktionen (NEGF) theoretisch untersucht. Es wird mit kohärenten Systemen begonnen und ballistischer Transport und Leitwertquantisierung in homogenen tight-binding Gittern diskutiert. Es wird gezeigt, dass durch Unordnung im System Transmissionsresonanzen hervorgerufen werden. Nach einer kurzen Einführung in Anderson-Lokalisierung, wird eine kompakte Formel für den unordnungsgemittelten Widerstand mit Hilfe von erzeugenden Funktionen hergeleitet.

Transport in Nanostrukturen findet auf Grund von Dekohärenz im Allgemeinen in einem intermediären Regime zwischen Quanten- und klassischem Transport statt. Die Effekte von Dekohärenz auf den Elektronentransport werden im Rahmen eines statistischen Modells untersucht. Grundlegende Idee dieses Modells ist es Dekohärenzregionen, an denen vollständige Phasen- und Impulsrandomisierung stattfindet, räumlich über das Nanosystem zu verteilen. Der Transport zwischen diesen Regionen ist phasenkohärent. Anschließend wird ein Ensemble-Mittel der untersuchten Transportgröße über räumliche Dekohärenzkonfigurationen berechnet, die gemäß einer Wahrscheinlichkeitsverteilung erstellt werden. Es wird diskutiert, wie homogene tight-binding Ketten durch Dekohärenz vom quantenballistischen zum klassisch Ohmschen Regime getrieben werden. Anschließend wird gezeigt, dass der Transport durch ungeordnete Systeme signifikant von der räumlichen Verteilung der Dekohärenzregionen beeinflusst wird. Wenn die Dekohärenz homogen verteilt ist, dann ist der Transport Ohmsch für jeden endlichen Dekohärenzgrad. Wenn im Gegensatz die Dekohärenz zufällig verteilt ist, dann lässt sich ein Isolator-Metall Übergang vom lokalisierten zum Ohmschen Regime bei einem kritischen Dekohärenzgrad beobachten, der einer kritischen Phasenkohärenzlänge entspricht. Es wird auch diskutiert, wie sich Transport in ungeordneten Gittern durch Dekohärenz optimieren lässt. Das Dekohärenzmodell wird um pure Dephasierung erweitert. Es wird gezeigt, dass Resonanzen in der Transmission durch pure Dephasierung unterdrückt werden, aber die Transmission im Mittel erhalten ist. Obiger Isolator-Metall Übergang ist unabhängig davon, ob mit der Phasenrandomisierung auch Impulsrandomisierung einhergeht, oder nicht.

Magnetotransport entlang des Randes zweidimensionaler Elektronensysteme wird studiert. Es wird untersucht wie Elektronen, kohärent injiziert an einem Punkt auf dem Rand eines zweidimensionalen Elektronengases (2DEG), durch ein senkrechtes Magnetfeld auf einen anderen Punkt auf dem Rand fokussiert werden. Im schwachen Magnetfeld zeigt der 4-Punkt-Hall-Widerstand äquidistante Peaks, die sich durch klassische Zyklotronbahnen erklären lassen. Wenn das Magnetfeld verstärkt wird, dann treten anomale Oszillationen auf, die den Quanten-Hall-Plateaus überlagert sind. Es wird gezeigt, dass sich alle Oszillationen im Hall-Widerstand durch die Interferenz der besetzten Randkanäle erklären lassen. Die anomalen Oszillationen sind Schwebungen, die auftreten, wenn nur einige wenige Randkanäle besetzt sind. Die Robustheit dieses Effekts wird demonstriert, indem Dekohärenz sowie partiell diffusive Streuung am Rand eingeführt wird. Die Widerstandsoszillationen lassen sich sowohl in einem nichtrelativistischen 2DEG beobachten, wie auch in dem relativistischen 2DEG von Graphen. Es wird auch gezeigt, dass endlicher Strom auf armchair-Kanten von Graphenstreifen fließt, wohingegen der Strom auf zigzag-Kanten verschwindet. Dieser Randstrom lässt sich darauf zurückführen, dass auf armchair-Kanten Kohlenstoffatome beider Graphenuntergitter auftreten, wohingegen auf zigzag-Kanten nur Atome eines Untergitters liegen. Die Dissertation endet mit einigen Bemerkungen zu Hofstadters Schmetterling, der auf der Titelseite abgebildet ist.

Contents

1 Introduction and outline

In the last 50 years, the development of microprocessors has changed our daily lives. The computational power, which has been offered years ago by supercomputers of size of a warehouse, is provided nowadays by a smartphone carried in our pockets. This remarkable development can be expressed by Moore's law [125], which says that the number of transistors, the basic unit of each microprocessor, is doubled every two years. The validity of Moore's law is proven in Figure 1.1 (left) for microprocessors offered by the company Intel since 1970. As depicted in Figure 1.1 (right), this development has been achieved by continuous miniaturization from the scale of several microns to a few nanometers. However, it is clear that miniaturization cannot be continued further, when structures of individual atoms are reached, which is expected around 2030 according to the ITRS roadmap.[1] Therefore, novel concepts are necessary in order to increase the computational power of microprocessors also in the next decades.
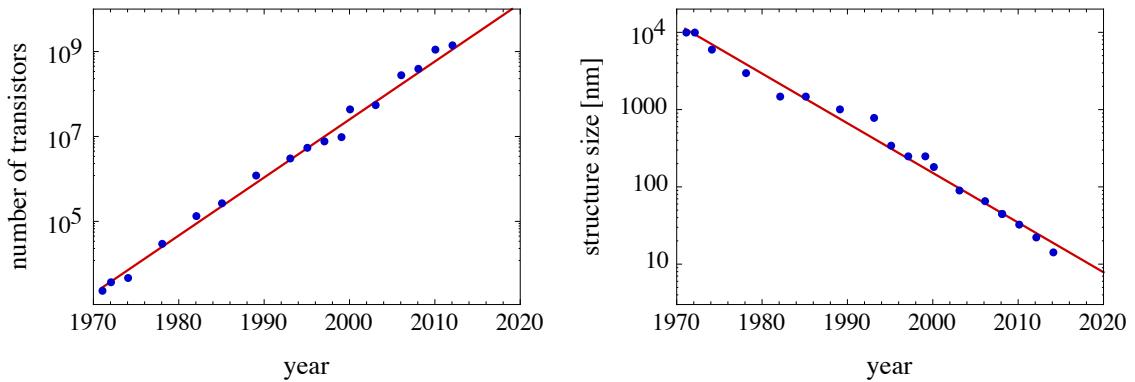
Figure 1.1: Development of the number of transistors (left) and structure size (right) of microprocessors since 1970. In agreement to Moore's law the number of transistors is doubled every second year, which is achieved by continuous miniaturization. However, as this approach cannot be continued arbitrarily, novel concepts are necessary. Data are taken from www.intel.com/museum.

One of these new ideas is to build up the transistors not in silicon but in graphene [13, 129, 159]. However, as such transistors are difficult to realize due to the absence of a band gap in pristine graphene, it has been suggested to use the negative differential resistance of graphene and non-Boolean logic circuits for a novel computational architecture [114]. Recently, also the first working microprocessor based on carbon nanotubes has been reported [162]. Another major issue of today's microprocessors is their energy consumption, which is converted to large extend solely into heat. To overcome this issue topological insulators, in which dissipationless current flow is possible, are considered as

---

[1]Further information to the International Roadmap for Semiconductors can be found at: www.itrs.net

a building block of novel electronic devices [34, 81, 116]. In this thesis, we study theoretically quantum transport trough nanostructures. Our aim is to increase the knowledge of the transport properties of these systems and to contribute at least a tiny part to the development of future technologies.

The outline of this thesis is as follows: In Chapter 2, we start with a short but self-contained introduction into the nonequilibrium Green's function (NEGF) method, which allows to calculate electron transport in nanostructures on the basis of quantum theory. In Chapter 3, we apply the NEGF method to study quantum coherent transport through tight-binding lattices. Ballistic conduction, conductance quantization, resistance oscillations due to interference, and Anderson localization are discussed. As the transport in nanosystems takes place in an intermediate regime between classical-Ohmic and quantum-coherent transport, in Chapter 4 the effects of decoherence on electron transport are studied by means of a statistical model. In particular, we discuss if Anderson localization can survive a finite degree of decoherence and show that the spatial distribution of decoherence has significant effects on the transport. In Chapter 5, magnetotransport in two-dimensional electron systems is studied. We discuss how electrons, coherently injected at one point on the boundary of a two-dimensional electron gas (2DEG), can be focused by a perpendicular magnetic field on another point of that boundary. We investigate how the system properties change, when the magnetic field strength is increased, and report anomalous resistance oscillations in intermediate fields. We consider a nonrelativistic 2DEG, as it can be realized in semiconductor heterostructures, as well as a relativistic 2DEG found in graphene. In Chapter 6, the conclusions and a brief outlook are given. The Appendix contains some calculation and derivations, which are not included in the main text.

2 Basics of quantum transport

On the long way of transport theory in solid state materials, one of the first milestones was the Drude-Sommerfeld model [52, 164], which allows to understand electric and thermal conduction in metals. Its main ideas are that the electrons follow the Fermi-Dirac distribution and only electrons close to the Fermi energy contribute to the conduction. These conduction electrons are scattered randomly after a given relaxation time. This gives rise to Ohm's law in metals. Further significant steps were Bloch's theorem [20] and the band structure theory [24, 141, 190, 191], which allow to understand the difference between metals, semiconductors and insulators.

However, when the system size is reduced to the nanometer scale, several characteristic lengths have the same order of magnitude:

- Mean free path ℓ_m: The average distance after which an electron is scattered and its momentum is randomized. The mean free path is determined by both inelastic scattering, which goes along with phase randomization, as well as elastic scattering for which the transport is still coherent.

- Phase coherence length ℓ_ϕ: The average distance after which the electron phase is randomized. Phase randomization can go along with momentum randomization if the electrons are scattered inelastically. However, both processes can also appear independently from each other.

- Fermi wavelength λ_F: Wavelength of the electrons at the Fermi energy. The Fermi wavelength gives the length scale at which quantum effects emerge.

- Localization length λ: Average spatial extent of the exponentially decaying electron eigenstates in a disordered quantum system, see Section 3.2.2.

- System size L

This gives rise to novel conduction properties. An electron can propagate *ballistically* through a homogeneous nanosystem without any scattering event, which results in a length-independent resistance caused solely by the contacts [42]. Ballistic transport is found, for example, in carbon nanotubes [14, 62] and graphene [21, 53]. It has also been utilized, for example, to build ballistic rectifiers [105, 165]. Moreover, when not only the momentum of the electrons is preserved but also its phase information, *interference effects* may influence the transport drastically, as it can be seen for example in Aharonov-Bohm experiments [15, 76] and in the coherent electron focusing [6, 169, 181], which will be discussed in detail in Chapter 5. In contrast, in disordered nanosystems *Anderson localization* [9, 56, 109] is found, which is indicated by an exponential increase of the resistance with the system size. Therefore, in order to describe the transport processes on the nanometer scale correctly, a completely different approach is necessary, which starts with a microscopic quantum description of the system.

In this Chapter, we give a short but self-contained introduction into quantum transport using the non-equilibrium Green's function (NEGF) approach. Instead of applying many-body perturbation theory [97, 102, 117], we follow the textbooks by Datta [42–44] and motivate physically the required equations. However, the given equations are exact for the systems studied in this thesis.
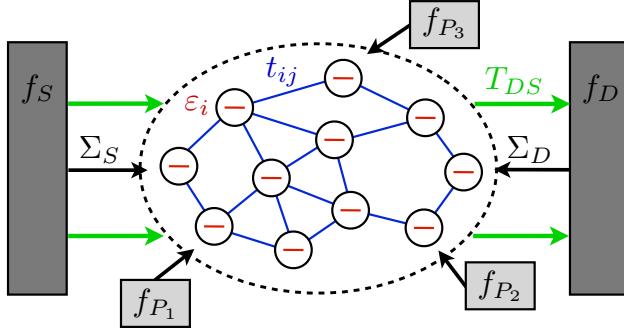
Figure 2.1: The transport of electrons from the source S to the drain D through a nanosystem is studied in this thesis. The nanosystem is described by the Hamiltonian (2.1) and can be visualized by a network of sites ε_i and bonds t_{ij}, see the region enclosed by the dashed ellipse. It is also assumed that additional voltage probes P_i are attached to the system. All reservoirs are characterized by energy distribution functions f_p with $p \in \{S, P_1, P_2, P_3, D\}$.

2.1 Definitions and concepts

2.1.1 Hamiltonian of the nanosystem

The nanosystem is described by a Hamiltonian H, which in this thesis has the form

$$H = \sum_i \varepsilon_i \left|i\right\rangle \left\langle i\right| + \sum_{j<i} \left(t_{ij} \left|i\right\rangle \left\langle j\right| + \text{H.c.}\right). \tag{2.1}$$

This Hamiltonian can be visualized by a network of sites and bonds, see the region enclosed by the dashed ellipse in Figure 2.1. The onsite energy ε_i represents the potential energy, which is necessary to occupy the state $\left|i\right\rangle$ (the ith site) by an electron. The coupling matrix element t_{ij} is proportional to the transition rate of electrons from state $\left|j\right\rangle$ to state $\left|i\right\rangle$ (from the jth site to the ith site).

2.1.2 Effect of a magnetic field

The effect of a magnetic field $\boldsymbol{B}$ can be taken into account by

$$t_{ij}(\boldsymbol{B}) = t_{ij}(\boldsymbol{B} = 0)\, e^{i\frac{e}{\hbar}\int d\boldsymbol{l}\cdot\boldsymbol{A}}, \tag{2.2}$$

where $\boldsymbol{A}$ is the vector potential of the magnetic field. The path integral is along the straight connection between the position of sites j and i in space. Citing Feynman's famous lectures, this substitution is "a basic statement of quantum mechanics" [58, Chapter 21-1], which expresses the principle of minimal gauge invariant coupling. In the literature it is also often referred to as Peierls substitution [87, 142].

2.1.3 The spectral function A

The spectral function is defined as[1]

$$A(E) \equiv 2\pi\delta(E - H). \tag{2.3}$$

In real space the expansion in terms of eigenfunctions $\psi_k(\boldsymbol{r})$ and eigenenergies ϵ_k of the Hamiltonian H

$$A(\boldsymbol{r}, \boldsymbol{r}', E) = 2\pi \sum_k \psi_k(\boldsymbol{r})\delta(E - \epsilon_k)\psi_k^*(\boldsymbol{r}') \tag{2.4}$$

shows that the diagonal elements of the spectral function (apart from the factor 2π) give the local density of states $D(\boldsymbol{r}, E)$ (LDOS). The total density of states $D(E)$ (DOS) is then obtained by integration over space, or more generally, by the trace of (2.3)

$$D(E) = \frac{1}{2\pi}\text{Tr}\left(A(E)\right) = \sum_k \delta(E - \epsilon_k). \tag{2.5}$$

2.1.4 The Green's functions G and G^+

The δ distribution can be represented by

$$2\pi\delta(E - \epsilon_k) = \frac{2\nu}{(E - \epsilon_k)^2 + \nu^2} = \text{i}\left[\frac{1}{E - \epsilon_k + \text{i}\nu} - \frac{1}{E - \epsilon_k - \text{i}\nu}\right], \tag{2.6}$$

where ν is an infinitesimal positive number. Using this representation of the δ distribution, the spectral function can be written as

$$A(E) = 2\pi\delta(E - H) = \text{i}\left[\underbrace{(E - H + \text{i}\nu)^{-1}}_{\substack{\text{retarded} \\ \text{Green's function } G}} - \underbrace{(E - H - \text{i}\nu)^{-1}}_{\substack{\text{advanced} \\ \text{Green's function } G^+}}\right] = -2\,\text{Im}\,(G), \tag{2.7}$$

where we have introduced the (retarded) Green's function G and the advanced Green's function G^+. As the DOS has to be positive, we also learn from (2.7) that the diagonal matrix elements of the Green's function fulfill $\text{Im}\,(G_{ii}) < 0$.

2.1.5 The correlation function G^n

Using the language of second quantization, the correlation function G^n is defined as[2]

$$G_{ij}^\text{n}(t, t') \equiv \langle c_j^+(t')c_i(t)\rangle, \tag{2.8}$$

where c_i^+ and c_i are the creation and annihilation operators for an electron at the ith site, respectively. In the steady state G^n depends only on the time difference and after a Fourier transform to the energy domain, the above definition shows that G^n is nothing but the

---

[1]For clarity we omit unit matrices, which match scalars (energy E) to matrices (Hamiltonian H).

[2]Instead of the correlation function G^n, the lesser Green's function $G^<$ is also commonly used in the literature, see e.g. [51]. These functions are connected by $G^< = \text{i}G^\text{n}$.

energy resolved density matrix (times 2π). In the single particle picture, this definition motivates the substitution rule

$$|i\rangle \langle j| \rightarrow \frac{1}{2\pi} G_{ij}^{\mathrm{n}}, \tag{2.9}$$

which allows to introduce advanced many-particle concepts in a single particle description.

In equilibrium the electron density is determined by the occupation of the density of states according to the Fermi distribution $f(E - \mu)$ with chemical potential μ. Therefore, we conclude that in equilibrium the correlation function is related to the spectral function by

$$G_{\mathrm{eq}}^{\mathrm{n}}(E) = A(E)f(E - \mu). \tag{2.10}$$

2.2 Open quantum systems: Σ and Σ^{in}

In order to study transport of electrons through the nanosystem, we have to connect it to a source S and a drain D reservoir, see the dark gray rectangles in Figure 2.1. The source and drain are in equilibrium and characterized by Fermi distributions $f_{S/D} \equiv f(E - \mu_{S/D})$ with chemical potentials $\mu_{S/D}$. Their difference drives the system out of equilibrium and causes the current flow. The effect of additional voltage probes, sketched by the light gray rectangles in Figure 2.1, is discussed in Section 2.4.

The isolated reservoirs are described by the Hamiltonians $H_{S/D}$, which fulfill the Schrödinger equations

$$(E - H_S)|\Phi_S\rangle = 0, \tag{2.11a}$$
$$(E - H_D)|\Phi_D\rangle = 0. \tag{2.11b}$$

These equations can be rewritten in the form

$$(E - H_S + \mathrm{i}\nu)|\Phi_S\rangle = |Q_S\rangle, \tag{2.12a}$$
$$(E - H_D + \mathrm{i}\nu)|\Phi_D\rangle = |Q_D\rangle, \tag{2.12b}$$

where ν is an infinitesimal positive number. The term $\mathrm{i}\nu|\Phi_{S/D}\rangle$ represents the extraction of electrons from the contact, whereas $|Q_{S/D}\rangle$ represents the reinjection of electrons from external sources. Extraction and reinjection are necessary to maintain the reservoirs in equilibrium. The Schrödinger equation is mathematically unchanged, if we identify $\mathrm{i}\nu|\Phi_{S/D}\rangle = |Q_{S/D}\rangle$. However, the transition from (2.11) to (2.12) is not only a formal modification of the Schrödinger equation but a change in the point of view. In the latter, E is no longer an eigenenergy of the Hamiltonian but an independent variable, which gives the energy of excitations $|Q_{S/D}\rangle$ from external sources. Whereas in (2.11) the $|\Phi_{S/D}\rangle$ are non-zero only for the eigenenergies, in (2.12) the $|\Phi_{S/D}\rangle$ are non-zero for any energy and represent the response of the reservoirs to external excitations.

Now, what happens when the reservoirs are connected to the nanosystem by coupling matrices $\tau_{S/D}$? The states $|\Phi_{S/D}\rangle$ in the reservoirs spill over and excite states $|\psi\rangle$ in the nanosystem, which in return also excite states $|\chi_{S/D}\rangle$ in the reservoirs. The Schrödinger equation of the coupled system reads

$$\begin{pmatrix} E - H_S + \mathrm{i}\nu & -\tau_S^+ & 0 \\ -\tau_S & E - H & -\tau_D \\ 0 & -\tau_D^+ & E - H_D + \mathrm{i}\nu \end{pmatrix} \begin{pmatrix} \Phi_S + \chi_S \\ \psi \\ \Phi_D + \chi_D \end{pmatrix} = \begin{pmatrix} Q_S \\ 0 \\ Q_D \end{pmatrix}. \tag{2.13}$$

As it can be assumed that the reinjection $|Q_{S/D}\rangle$ is unchanged by the coupling, the first and the last row of (2.13) lead with (2.12) to

$$|\chi_S\rangle = G_S \tau_S^+ |\psi\rangle , \qquad (2.14a)$$
$$|\chi_D\rangle = G_D \tau_D^+ |\psi\rangle , \qquad (2.14b)$$

where

$$G_S \equiv (E - H_S + \mathrm{i}\nu)^{-1} , \qquad (2.15a)$$
$$G_D \equiv (E - H_D + \mathrm{i}\nu)^{-1} \qquad (2.15b)$$

are the Green's functions of the reservoirs. By means of (2.14) the middle row of (2.13) reads

$$(E - H - \Sigma_S - \Sigma_D) |\psi\rangle = |Q\rangle , \qquad (2.16)$$

where we defined the so-called **self-energies**

$$\Sigma_S \equiv \tau_S G_S \tau_S^+ , \qquad (2.17a)$$
$$\Sigma_D \equiv \tau_D G_D \tau_D^+ \qquad (2.17b)$$

and the total excitation of the nanosystem

$$|Q\rangle \equiv \tau_S |\Phi_S\rangle + \tau_D |\Phi_D\rangle . \qquad (2.18)$$

Finally, we can write for its states

$$|\psi\rangle = G |Q\rangle , \qquad (2.19)$$

where we defined the **Green's function of the nanosystem**

$$G \equiv (E - H - \Sigma_S - \Sigma_D)^{-1} . \qquad (2.20)$$

Therefore, the Schrödinger equation of the coupled system has been transformed to a single equation for the nanosystem, which is "open" to the environment by self-energies. This approach simplifies the problem drastically because the dimension of the Fock space of the nanosystem is much smaller than the dimension of the Fock space of the coupled system. The self-energies represent a non-Hermitian modification of the Hamiltonian, which shift its eigenenergies from the real axis into the complex plane. The imaginary part of the eigenenergies is inversely proportional to the lifetime of the states in the nanosystem and causes an energy broadening, see Figure 2.2.

With the definition of the **broadening matrix**

$$\Gamma \equiv \mathrm{i} \left(\Sigma - \Sigma^+ \right) \qquad (2.21)$$

we obtain[3] for the spectral function of the nanosystem

$$A \equiv \mathrm{i} \left(G - G^+ \right) = G \left(\Gamma_S + \Gamma_D \right) G^+ = A_1 + A_2. \qquad (2.22)$$

---

[3]To obtain (2.22), we use $\mathrm{i} \left((G^{-1})^+ - G^{-1} \right) = \Gamma_S + \Gamma_D$ and by multiplication with G from the left and G^+ from the right, we arrive at $\mathrm{i} \left(G - G^+ \right) = G \left(\Gamma_S + \Gamma_D \right) G^+$.
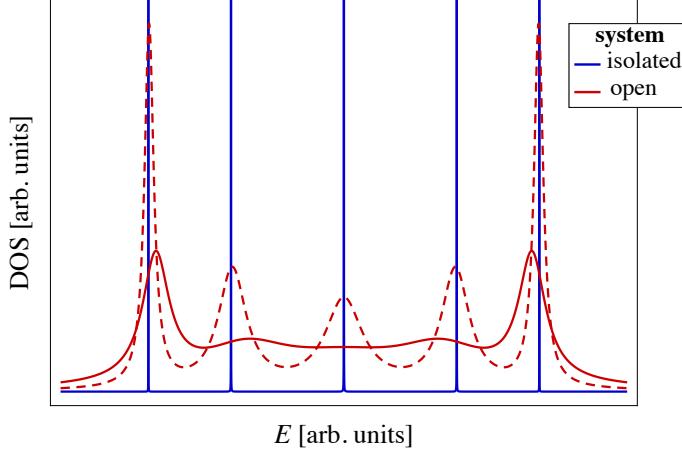
Figure 2.2: Energy resolved density of states (DOS) of a typical nanosystem. The DOS of the isolated system shows peaks at the (discrete) eigenenergies of the Hamiltonian. These peaks are broadened, if the system is opened increasingly (dashed to solid red curve) to reservoirs.

These spectral functions $A_{1/2} \equiv G\Gamma_{S/D}G^+$ give the density of states for electrons originating S/D and should not be confused with the spectral functions $A_{S/D} = \mathrm{i}(G_{S/D} - G_{S/D}^+)$, which give the density of states in the reservoirs. In order to calculate the correlation function, we study the projector

$$
\begin{aligned}
|\psi\rangle \langle\psi| \;\overset{(2.19)}{=}&\; G\,|Q\rangle\,\langle Q|\,G^+ \\
\overset{(2.18)}{=}&\; G\tau_S\,|\Phi_S\rangle\,\langle\Phi_S|\,\tau_S^+ G^+ \;+\; G\tau_D\,|\Phi_D\rangle\,\langle\Phi_D|\,\tau_D^+ G^+ \\
&+ \underbrace{G\tau_S\,|\Phi_S\rangle\,\langle\Phi_D|\,\tau_D^+ G^+ \;+\; G\tau_D\,|\Phi_D\rangle\,\langle\Phi_S|\,\tau_S^+ G^+}_{=\,0,\ \text{because no direct coupling between the reservoirs}}.
\end{aligned}
\tag{2.23}
$$

Applying the substitution (2.9) and using (2.10) for the reservoirs, in which equilibrium is assumed, we obtain for the non-equilibrium **correlation function of the nanosystem**

$$
\begin{aligned}
G^{\mathrm{n}} &= G\underbrace{\tau_S A_S \tau_S^+}_{\Gamma_S} G^+ f(E-\mu_S) + G\underbrace{\tau_D A_D \tau_D^+}_{\Gamma_D} G^+ f(E-\mu_D) \\
&= A_1 f(E-\mu_S) + A_2 f(E-\mu_D) \tag{2.24a} \\
&= G\Sigma^{\mathrm{in}}G^+, \tag{2.24b}
\end{aligned}
$$

where we defined the **inscattering function**

$$
\Sigma^{\mathrm{in}} \equiv \Sigma_S^{\mathrm{in}} + \Sigma_D^{\mathrm{in}} = \Gamma_S f_S + \Gamma_D f_D. \tag{2.25}
$$

As it could be expected for non-interacting electrons, the correlation function of the nanosystem, which gives the electron density, is the sum of the spectral functions occupied by the Fermi distributions of the corresponding contacts.

The equations for the Green's function (2.20) and for the correlation function (2.24b) are two essential results of the non-equilibrium Green's function approach. We have motivated them physically, but arrived essentially at the same result as in Keldysh's seminal paper [102, eqs. (75)–(77)], where many-body perturbation theory is applied. In fact the strength of the non-equilibrium Green's function approach is more profound because it allows to include arbitrary interactions in the system by suitable self-energies and inscattering functions, see e.g. [42, 51] for details. These interactions can formally be considered as additional virtual reservoirs attached to the system.

2.3 Current equations

In order to define the current operator, we start with the isolated nanosystem. By means of the time-dependent Schrödinger equation, we obtain for the time evolution of the projector

$$\frac{\mathrm{d}}{\mathrm{d}t} |\psi\rangle \langle\psi| + \frac{\mathrm{i}}{\hbar} \big[H, |\psi\rangle \langle\psi| \big] = 0. \tag{2.26}$$

In the same way as the continuity equation of quantum mechanics,[4] this equation reflects the conservation of probability density. However, when the nanosystem is connected to reservoirs, electrons can enter and leave it and thus, the probability density in the system is not conserved. In steady state, the first term of (2.26) vanishes and the remaining commutator tells us the rate, at which electrons are lost in the system. Therefore, applying the substitution rule (2.9), the current operator can be defined as

$$I^{\mathrm{op}} \equiv \frac{\mathrm{i}e}{h} \big[H, G^{\mathrm{n}} \big], \tag{2.27}$$

where e is the electron charge. Its off-diagonal elements

$$I^{\mathrm{op}}_{ij} = \frac{\mathrm{i}e}{h} \big(t_{ij} G^{\mathrm{n}}_{ji} - t_{ji} G^{\mathrm{n}}_{ij} \big) = \frac{2e}{h} \mathrm{Im} \big(t^*_{ij} G^{\mathrm{n}}_{ij} \big) \tag{2.28}$$

give the local energy resolved current flowing from the ith to the jth site [30, 37], whereas its diagonal elements correspond to direct tunneling between the reservoirs and the sites.

The total flow of electrons with energy E through the dashed ellipse in Figure 2.1 is then given by[5]

$$I(E) \equiv \mathrm{Tr} \left(I^{\mathrm{op}} \right) = \frac{e}{h} \mathrm{Tr} \left(\Sigma^{\mathrm{in}} A - \Gamma G^{\mathrm{n}} \right). \tag{2.30}$$

As the number of electrons is conserved, the inflow of electrons equals the outflow and hence, the total flow is exactly zero. Taking into account the invariance of the trace under

---

[4]Indeed, when we go to local space by multiplying (2.26) with $\langle\boldsymbol{r}|$ from left and $|\boldsymbol{r}\rangle$ from right, we obtain the continuity equation in its common form.

[5]The current operator can be rewritten by means of

$$[H, G^{\mathrm{n}}] \overset{(2.24\mathrm{b})}{=} HG\Sigma^{\mathrm{in}}G^+ - G\Sigma^{\mathrm{in}}G^+ H \tag{2.29a}$$

$$\overset{(2.20)}{=} G\Sigma^{\mathrm{in}} - \Sigma^{\mathrm{in}}G^+ + \underbrace{G\Sigma^{\mathrm{in}}G^+}_{G^{\mathrm{n}}} \Sigma^+ - \Sigma \underbrace{G\Sigma^{\mathrm{in}}G^+}_{G^{\mathrm{n}}}. \tag{2.29b}$$

Using (2.21), (2.22) and the invariance of the trace under cyclic permutations, we obtain (2.30).

cyclic permutations, this can be seen already by means of the definition of the current operator (2.27). However, separating the inscattering function and the broadening function into the individual contributions of each reservoir, we obtain for the non-zero current at the drain

$$I_D(E) = \frac{e}{h} \text{Tr} \left(\Sigma_D^{\text{in}} A - \Gamma_D G^{\text{n}} \right).$$ (2.31)

This current equation is another key result of the non-equilibrium Green's function approach. For non-interacting electrons it can be further simplified by means of (2.24a) and (2.25). Integrating over energy, we arrive finally at the famous **Landauer formula** [110, 111] for the total current through the system[6]

$$I_D = \frac{e}{h} \int \mathrm{d}E \, T_{DS}(E) \big(f(E - \mu_S) - f(E - \mu_D) \big),$$ (2.32)

where we defined the **transmission function**

$$T_{DS} \equiv \text{Tr} \left(\Gamma_D G \Gamma_S G^+ \right).$$ (2.33)

The transmission function T_{DS} gives the probability that an electron injected by the source will transmit to the drain. For an isolated system[7], the transmission is perfect ($T_{DS} = 1$) at its eigenenergies, whereas it vanishes elsewhere, see Figure 2.3. These transmission peaks are broadened, if the system is increasingly opened to reservoirs. Note that for sufficiently strong coupling to the reservoirs, the transmission in the band center is perfect and nearly constant. The transmission through various tight-binding lattices is discussed in detail in Chapter 3.

In the following, we study mostly electron transport in the limit of an infinitesimal bias voltage $\mu_S \to \mu_D = \mu$ at zero temperature. In this case the transmission function at the Fermi energy gives directly the zero-bias conductance

$$\mathcal{G} = \frac{e^2}{h} T_{DS}(E = \mu).$$ (2.34)

The prefactor e^2/h is the conductance quantum, which may be multiplied by a factor of 2 if spin degeneracy can be assumed. The **zero-bias resistance** is defined accordingly as the inverse of the transmission at the Fermi energy

$$R = \frac{h}{e^2} \frac{1}{T_{DS}(E = \mu)}.$$ (2.35)

2.4 Multi-terminal systems

Now, what happens when more than two reservoirs are attached to the nanosystem? These additional reservoirs could be real voltage probes as well as virtual reservoirs, which represent interactions in the system. For such multi-terminal system, the formulae given in the preceding Sections can still be applied, when we take into account the self-energies

---

[6]If not stated otherwise, integration boundaries extend from $-\infty$ to $+\infty$.

[7]In order to define the transmission function, the isolated system is still infinitesimally weakly coupled to reservoirs.
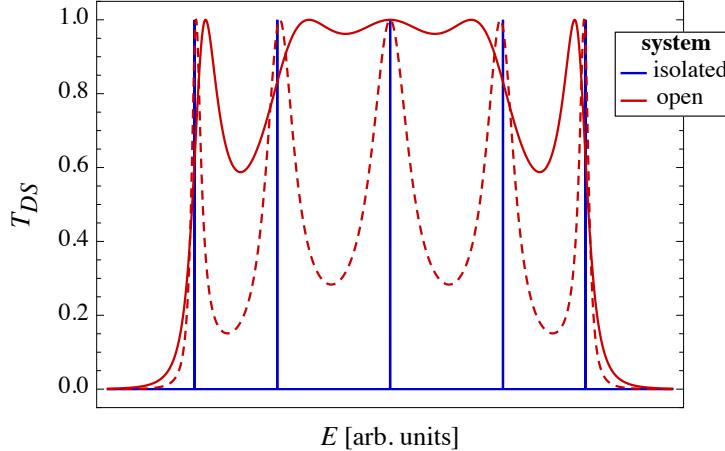
Figure 2.3: Transmission through the same nanosystem as in Figure 2.2. In the same way as the DOS, the transmission of the isolated system is perfect ($T_{DS} = 1$) at its eigenenergies, whereas it vanishes elsewhere. These transmission peaks are broadened, if the system is opened increasingly (dashed to solid red curve) to reservoirs.

Σ_i and inscattering functions Σ_i^{in} of all reservoirs, see for example Figure 2.1 where $i \in \{S, P_1, P_2, P_3, D\}$ reservoirs are attached.

For the (energy resolved) current at the ith reservoir, we have to sum up the contributions of all reservoirs to obtain the **Landauer-Büttiker formula** [25, 27]

$$I_i(E) = \frac{e}{h} \sum_j T_{ij} \left(f_j - f_i \right). \tag{2.36}$$

The energy distribution functions $f_{S/D}$ of the source and the drain are Fermi functions with given chemical potential and bias voltage. The distribution functions of the additional reservoirs are determined by the condition that the total current at these reservoirs has to vanish. This condition applies for real voltage probes as well as for virtual reservoirs. Voltmeters are supposed to have an infinitely high internal resistance, which suppresses the current flow. Also at virtual reservoirs, which exist only conceptually, no real particle can be lost and therefore, no current can flow. Applying the Landauer-Büttiker formula (2.36), we obtain a system of linear equations for the unknown energy distribution functions[8]

$$\sum_j \mathcal{T}_{ij} \left(f_j - f_D \right) = T_{iS} \left(f_S - f_D \right), \tag{2.38}$$

---

[8]For example, in the case shown in Figure 2.1 this system of linear equations for the unknown distribution functions f_i, $i \in \{1, 2, 3\}$ reads:

$$\begin{pmatrix} T_{1S} + T_{12} + T_{13} + T_{1D} & -T_{12} & -T_{13} \\ -T_{21} & T_{2S} + T_{21} + T_{23} + T_{2D} & -T_{23} \\ -T_{31} & -T_{32} & T_{3S} + T_{31} + T_{32} + T_{3D} \end{pmatrix} \begin{pmatrix} f_1 - f_D \\ f_2 - f_D \\ f_3 - f_D \end{pmatrix} = \begin{pmatrix} T_{1S} \\ T_{2S} \\ T_{3S} \end{pmatrix} (f_S - f_D)$$

$$\tag{2.37}$$

where

$$\mathcal{T}_{ij} \equiv \mathcal{R}_{ij}^{-1} \equiv \begin{cases} -T_{ij} & i \neq j, \\ \sum_{k \neq i} T_{ik} & i = j. \end{cases} \tag{2.39}$$

The current through the nanosystem is then given by

$$I_D(E) = \frac{e}{h} \left[T_{DS} + \sum_{ij} T_{Di} \mathcal{R}_{ij} T_{jS} \right] (f_S - f_D). \tag{2.40}$$

Comparing with (2.32) and (2.34) shows that the term in square brackets gives the zero-bias conductance. The sums in (2.38) and (2.40) are over the reservoirs with unknown energy distribution function, whereas the sum in (2.39) is over all reservoirs including the source and drain. The above equations reflect Kirchhoff's law for a network of quantum resistances $1/T_{ij}$. Applications of (2.40) will be discussed in the following Chapters.

2.5 Units

In order to keep the following discussion as clear and short as possible, we use the natural units of the system:

- The energy is measured in multiples of a typical coupling matrix element t_{ij} of the tight-binding Hamiltonian (2.1). The energy origin is defined by a typical onsite energy ε_i. We will study usually systems, for which (in absence of a magnetic field) the coupling between neighboring sites is homogeneous, i.e. $t_{ij} = t = \text{constant}$.

- The conductance is measured in multiples of the conductance quantum e^2/h. The resistance in multiples of h/e^2, accordingly.

On occasion, we will indicate the used units also in the following Chapters (in particular within the figures), in order to increase the accessibility and readability.

2.6 Further reading

In this Chapter, we have motivated physically the essential formulae required to study quantum transport at the nanoscale. However, to get a deeper understanding, it is indispensable to study the existing literature in detail. From the numerous textbooks, we would like to recommend a few, which could be helpful to understand this thesis.

Maybe the best starting point are the textbooks by Datta [42–44], who gives a didactically brilliant introduction into the physics of nanosystems. A mathematically more rigorous and yet readable introduction can be found in the book by Di Ventra [51]. The usage of Green's function in quantum mechanics is nicely explained in the book by Economou [55]. To get started the reader may also find useful the books by Heikkilä [84], Ihn [90] and Ferry, Goodnick and Bird [57]. We can also recommend the book on molecular electronics by Cuevas and Scheer [39].

3 Tight-binding lattices: Electronic properties and coherent transport

In this Chapter, we study tight-binding lattices, like one-dimensional (1D) chains, quasi-one-dimensional ribbons and two-dimensional (2D) grids. After discussing the band-structure and density of states (DOS), we show how reservoirs can be modeled by semi-infinite lattices or by the wide-band approximation. In Section 3.2, we study the coherent transport in tight-binding lattices. Ballistic conduction and conductance quantization are discussed. We also show that interference of the coherent electrons can give rise to resistance oscillations. The effect of the reservoir model on the transport is studied. Finally, Anderson localization of coherent electrons in disordered lattices is introduced and an analytical closed formula for the disorder averaged coherent resistance of 1D chains is given.

3.1 Electronic properties

3.1.1 The infinite tight-binding chain

The infinitely long homogeneous 1D tight-binding chain is described by the Hamiltonian

$$H = \sum_{i=-\infty}^{\infty} \varepsilon \left| i \right\rangle \left\langle i \right| + t \big(\left| i \right\rangle \left\langle i+1 \right| + \text{H.c.} \big). \tag{3.1}$$

As the onsite energies ε and the coupling matrix elements t are constant in a homogeneous chain, we use them to define the energy origin and the energy scale in our system, i.e. $\varepsilon = 0$ and $t = 1$. The Schrödinger equation can be solved by a plane wave ansatz for the eigenfunctions $\left| k \right\rangle = \sum_j \mathrm{e}^{\mathrm{i}kj} \left| j \right\rangle$, to obtain a cosine energy band

$$\epsilon(k) = 2\cos(k), \tag{3.2}$$

see Figure 3.1 (left). The DOS (per site) can be calculated directly from its definition

$$D(E) = \sum_k \delta\left(E - \epsilon(k)\right) = \int_0^\pi \frac{\mathrm{d}k}{\pi} \delta\left(E - 2\cos(k)\right) = \frac{\theta\left(1 - |E/2|\right)}{2\pi\sqrt{1 - (E/2)^2}}, \tag{3.3}$$

where $\theta(x)$ is the Heaviside function.[1] It has van Hove singularities at $E = \pm 2$, which correspond to the band edges (or the extrema) of the cosine band, see Figure 3.1 (right). Note that $\int \mathrm{d}E\, D(E) = 1$ is fulfilled, as every site can be occupied by a single electron.

---

[1] We can also calculate at first the Green's function of the tight-binding chain [55, Section 5.3.1]

$$G_{ij}(E) = \frac{-\mathrm{i}}{2\sqrt{1 - (E/2)^2}} \left(\mathrm{i}\sqrt{1 - (E/2)^2} - E/2 \right)^{|i-j|}. \tag{3.4}$$

Calculating the LDOS by $D_i(E) = -\text{Im}\left(G_{ii}(E)\right)/\pi$, we arrive at (3.3).
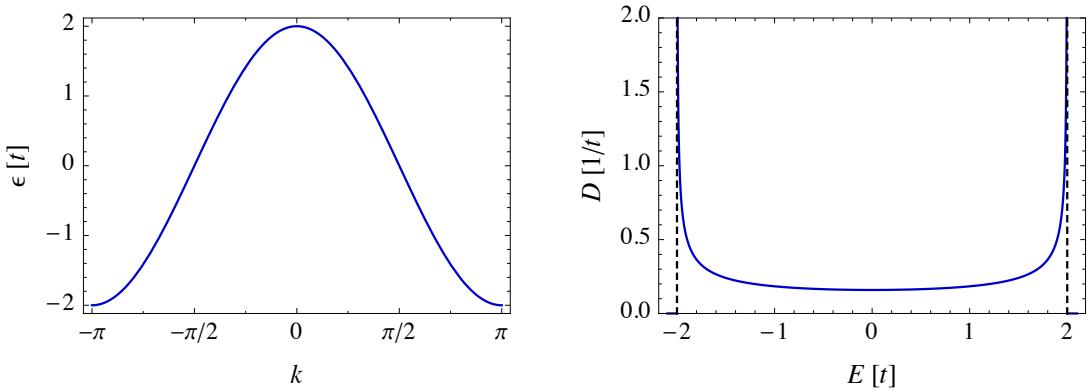
Figure 3.1: The homogeneous infinite tight-binding chain has a cosine band structure (left) and thus, band edges at $\epsilon = \pm 2$. Its DOS (right) shows van Hove singularities at the band edges.

3.1.2 The infinite tight-binding ribbon and grid

The homogeneous infinitely long quasi-1D tight-binding ribbon of width M is described by the Hamiltonian

$$H = \sum_{i=-\infty}^{\infty} \sum_{j=1}^{M} \varepsilon \left|i,j\right\rangle \left\langle i,j\right| + t\left(\left|i,j\right\rangle \left\langle i+1,j\right| + \text{H.c.}\right) + \sum_{i=-\infty}^{\infty} \sum_{j=1}^{M-1} t\left(\left|i,j\right\rangle \left\langle i,j+1\right| + \text{H.c.}\right). \quad (3.5)$$

For simplicity we use again $\varepsilon = 0$ and $t = 1$. By means of a Fourier sine transformation

$$\left|i,j\right\rangle = \sqrt{\frac{2}{M+1}} \sum_{j'=1}^{M} \sin\left(\frac{\pi j j'}{M+1}\right) \left|\widetilde{i,j'}\right\rangle \quad (3.6)$$

the ribbon can be decoupled into M independent tight-binding chains

$$H = \sum_{i=-\infty}^{\infty} \sum_{j'=1}^{M} 2\cos\left(\frac{\pi j'}{M+1}\right) \left|\widetilde{i,j'}\right\rangle \left\langle \widetilde{i,j'}\right| + t\left(\left|\widetilde{i,j'}\right\rangle \left\langle \widetilde{i+1,j'}\right| + \text{H.c.}\right), \quad (3.7)$$

which are shifted in energy by $2\cos\left(\frac{\pi j'}{M+1}\right)$. Therefore, the ribbon has M shifted cosine energy bands, and the DOS (per site) reads

$$D(E) = \frac{1}{2\pi M} \sum_{j=1}^{M} \frac{\theta\left(1 - \left|\frac{E}{2} - \cos\left(\frac{\pi j}{M+1}\right)\right|\right)}{\sqrt{1 - \left(\frac{E}{2} - \cos\left(\frac{\pi j}{M+1}\right)\right)^2}}. \quad (3.8)$$

The 2D tight-binding grid, which is obtained by taking the limit $M \to \infty$, can be diagonalized by the plane wave ansatz $\left|k,q\right\rangle = \sum_{l,m} e^{i(kl+qm)} \left|l,m\right\rangle$. The band structure

$$\epsilon(k,q) = 2\left(\cos(k) + \cos(q)\right) \quad (3.9)$$

is shown in Figure 3.2 (left). The DOS (per site), which can be calculated by using its definition or by converting in (3.8) the sum into an integral, is given by

$$D(E) = \frac{1}{2\pi^2} \mathcal{K}\left(1 - (E/4)^2\right) \theta\left(1 - |E/4|\right), \quad (3.10)$$

where $\mathcal{K}(x) = \int_0^{\pi/2} \mathrm{d}\phi \left(1 - x\sin^2(\phi)\right)^{-1/2}$ is the complete elliptic integral of first kind [3].[2] The DOS of the 2D tight-binding grid as well as the DOS of a ribbon of width $M = 7$ are shown in Figure 3.2 (right). The DOS of the ribbon shows the characteristic van Hove singularities of the shifted 1D chains. These singularities can be observed experimentally, for example, in carbon nanotubes [135] and in narrow graphene ribbons [173]. However, when the limit to the 2D grid is taken, only the van Hove singularity in the band-center survives, which corresponds to the saddle points in the energy bands, see the intersection points of the black lines in Figure 3.2 (left).
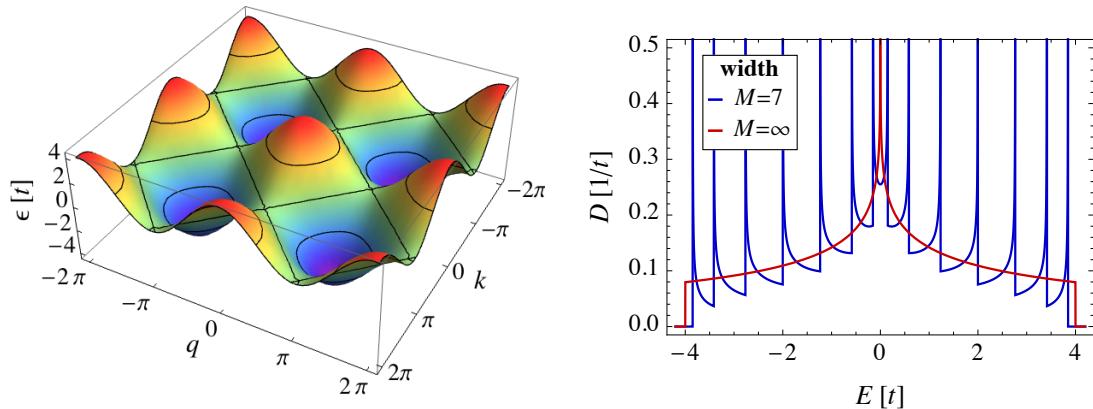

Figure 3.2: The 2D tight-binding grid has a cosine band structure (left). Its saddle points in the $\epsilon = 0$ plane cause a van Hove singularity in the band-center of the DOS (right, red). The DOS of a ribbon with width $M = 7$ (right, blue) shows $2M = 14$ van Hove singularities of the isolated 1D chains, see Figure 3.1.

3.1.3 Reservoir models: Semi-infinite lattices, wide-band approximation

When we truncate the chain at an arbitrary site, we obtain the homogeneous semi-infinite tight-binding chain

$$H = \sum_{i=1}^{\infty} \varepsilon \left|i\right\rangle \left\langle i\right| + t\left(\left|i\right\rangle \left\langle i+1\right| + \mathrm{H.c.}\right), \tag{3.11}$$

which can be diagonalized by the ansatz $\left|k\right\rangle = \sum_{j=1}^{\infty} \sin\left(kj\right)\left|j\right\rangle$. It has the same cosine energy band and the same DOS as the infinite chain, because effectively both systems are infinitely long. We have truncated the chain, because it can be used as a simple model for reservoirs, which we have to connect to the nanosystem in order to study transport, see Figure 3.3. Reservoirs have to provide a continuous DOS, which is occupied with electrons according to an energy distribution function $f(E)$, see [43, Section 8.4]. These requirements can be fulfilled with semi-infinite lattices.

The effect of the semi-infinite chain on the nanosystem is taken into account by its self-energy. Analyzing the matrix product in (2.17), we find that for the calculation of the self-energy we do not need to know the complete (infinite dimensional) Green's function of

---

[2]We could also calculate at first the Green's function of the tight-binding grid. However, as the expressions are quite large, we refer to [55, Section 5.3.2].
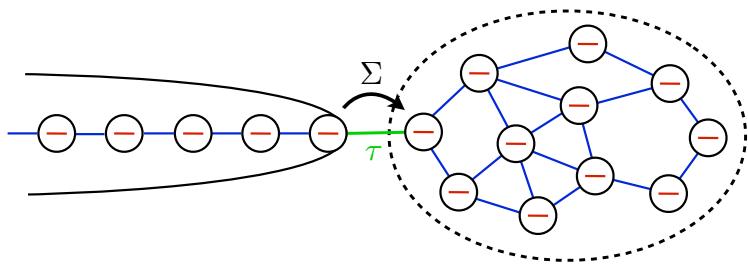
Figure 3.3: Semi-infinite tight-binding chains (left) can be used as a simple model for reservoirs, which we have to connect to the nanosystem (right) in order to study transport. For the self-energy of the chain, we have to calculate only the surface Green's function, i.e. the G_{11} matrix element of the Green's function, which is connected to the nanosystem by the coupling matrix τ.

the chain but only the matrix elements which are connected by the coupling matrix τ to the nanosystem. As shown in Figure 3.3, we have to calculate only the G_{11} matrix element to obtain the *surface Green's function* of the semi-infinite tight-binding chain

$$G_{11}(E) = \begin{cases} x + \sqrt{x^2 - 1} & \text{for } x \leq -1 \\ x - i\sqrt{1 - x^2} & \text{for } |x| < 1 \\ x - \sqrt{x^2 - 1} & \text{for } x \geq 1 \end{cases} \quad \text{with} \quad x = \frac{E}{2}. \tag{3.12}$$

A proof by means of Dyson's equation can be found in Appendix A.1 and A.2. The LDOS at the surface of the chain $D_1(E) = -\mathrm{Im}\,(G_{11}(E))/\pi$ is a semi-circle within the energy band $|E| < 2$ and vanishes outside, see the plot of the surface Green's function in Figure 3.4.
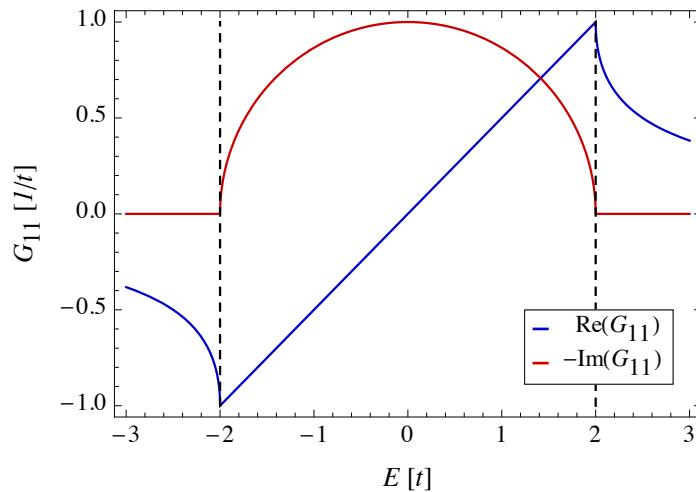

Figure 3.4: Surface Green's function $G_{11}(E)$ of the semi-infinite tight-binding chain. The LDOS at the surface of the chain $D_1 = -\mathrm{Im}\,(G_{11}(E))/\pi$ is a semi-circle within the energy band $|E| < 2$ and vanishes outside.

The self-energy of the semi-infinite chain reads

$$\Sigma_{\mathrm{ch}} = |\tau_{11}|^2 \, G_{11}, \tag{3.13}$$

where τ_{11} is the coupling matrix element between the chain and the nanosystem, see Figure 3.3. This contact model has been introduced by Caroli et al. in 1971 [30] but is still applied nowadays, see [5, 29, 39, 42, 72, 94, 153] for some recent work.

In the same way, a semi-infinite tight-binding ribbon of width M can be used as a reservoir model. Reminding us that the ribbon can be decoupled into independent 1D chains (3.7), we obtain by means of (3.12) for the surface Green's function of the decoupled ribbon

$$G'_{kk}(E) = \begin{cases} x_k + \sqrt{x_k^2 - 1} & \text{for } x_k \leq -1 \\ x_k - \mathrm{i}\sqrt{1 - x_k^2} & \text{for } |x_k| < 1 \\ x_k - \sqrt{x_k^2 - 1} & \text{for } x_k \geq 1 \end{cases} \quad \text{with } x_k = \frac{E}{2} - \cos\left(\frac{\pi k}{M+1}\right). \tag{3.14}$$

Applying again a Fourier sine transformation, the surface Green's function of the semi-infinite tight-binding ribbon of width M reads

$$G_{ij}(E) = \frac{2}{M+1} \sum_{k=1}^{M} \sin\left(\frac{\pi i k}{M+1}\right) \sin\left(\frac{\pi j k}{M+1}\right) G'_{kk}, \qquad i, j = 1, 2 \ldots M. \tag{3.15}$$

The surface Green's function of a ribbon of width $M = 7$ is shown in Figure 3.5. On the left, the diagonal matrix elements at the ribbon's edge G_{11} (solid curve) and in its center G_{44} (dashed curve) are shown as a function of energy. On the right, the imaginary part of the diagonal matrix elements is shown along the ribbon's end. Note that the imaginary part of these matrix elements is the LDOS at the surface of the ribbon (apart from the factor $-1/\pi$). From the surface Green's function of the ribbon, we can calculate the self-energy

$$\Sigma_{\mathrm{rb}} = \tau G \tau^+, \tag{3.16}$$

where the coupling matrix τ connects the surface of the nanosystem with the surface of the reservoir.
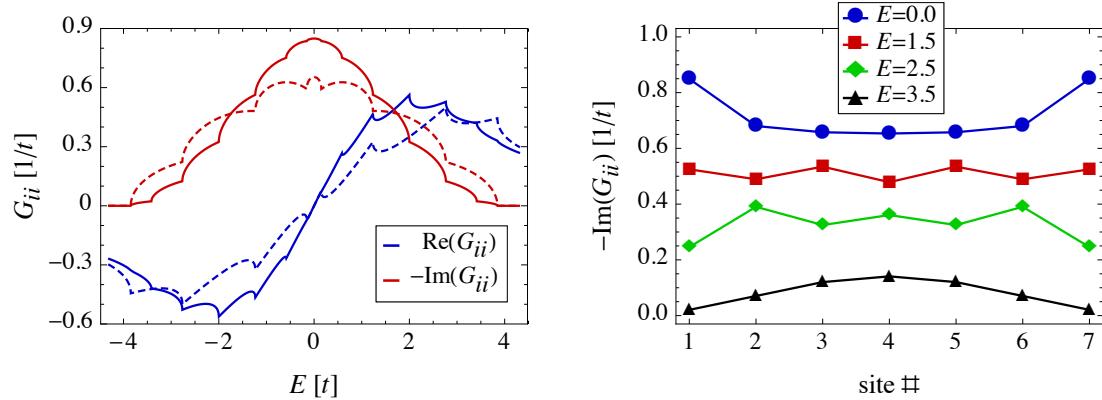

Figure 3.5: Surface Green's function for a ribbon of width $M = 7$. Left: diagonal matrix elements at the ribbons edge G_{11} (solid curve) and in its center G_{44} (dashed curve). Right: imaginary part of the diagonal matrix elements G_{ii} along the ribbon's end for four different energies.

Another contact model, which is commonly used [61, 115, 134, 184] and also applied in this thesis, is the *wide-band approximation* for the reservoir's self-energy

$$\Sigma_{\mathrm{wb}} = -\mathrm{i}\eta, \tag{3.17}$$

where $\eta > 0$ is a constant. This self-energy corresponds to a constant LDOS at the surface of the reservoir, which is in particular a reasonable approximation, when the bias voltage is infinitesimally small and only energies infinitesimally close to the Fermi energy have to be taken into account. The advantage of wide-band reservoirs is that they require less computational effort than semi-infinite lattices, while the results are qualitatively in many cases the same, as discussed in the following Section.

3.2 Coherent transport

3.2.1 Tight-binding chains

We study the quantum coherent transport through 1D tight-binding chains of length N

$$H = \sum_{i=1}^{N} \varepsilon_i \, |i\rangle \, \langle i| + \sum_{i=1}^{N-1} t\big(|i\rangle \, \langle i+1| + \mathrm{H.c.}\big). \tag{3.18}$$

The first and the last site of the chain are connected to reservoirs ($\Sigma_S = \Sigma_D = \Sigma$), which are modeled either by semi-infinite chains (3.13) or by the wide-band approximation (3.17). In this case, the transmission function

$$T_N(E) \stackrel{(2.33)}{=} 4\mathrm{Im}\,(\Sigma)^2 \, |G_{1N}|^2 \tag{3.19}$$

is determined by a single matrix element of the Green's function, which can be calculated efficiently by a recursion, see Appendix A.3.1.
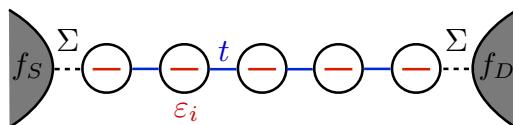
Figure 3.6: Tight-binding chain of length $N = 5$, which is connected to reservoirs. The inter-site coupling $t = 1$ is used as the energy unit.

The transmission through homogeneous chains ($\varepsilon_i = 0$) of length $N = \{5, 10, 15, 40\}$ as a function of the Fermi energy is shown in Figure 3.7. When homogeneous semi-infinite chains ($\varepsilon_{\mathrm{ch}} = 0$, $t_{\mathrm{ch}} = \tau_{11} = 1$) are used as the reservoirs, the transmission T_∞ is independent of the chain length because effectively an infinitely long homogeneous tight-binding chain is studied. Inside the conduction band $|E| < 2$ the transmission is perfect, because no scattering centers or grain boundaries exist, which would give rise to backscattering. Outside the conduction band the transmission vanishes, because tunneling through an infinitely long system is impossible. However, when the wide-band approximation ($\eta = 1$) is used for the reservoirs, the transmission oscillates as a function of energy, because the reservoirs can be considered as potential barriers, which give rise to backscattering and

Fabry-Perot-like interference effects [39, Section 11.8]. The transmission shows resonances whenever the Fermi energy approaches one of the eigenenergies of the system, which are located approximately at $E_i = 2\cos\left(\pi i/(N+1)\right)$ for $i = 1, 2 \ldots N$. Therefore, the number of resonances equals the length of the chain. This can also be seen in Figure 2.3, where the 5-site chain was studied for $\eta = \{0, 0.3, 1.0\}$. These oscillations, which may be unrealistic for longer chains, can be suppressed by decoherence, see Chapter 4.
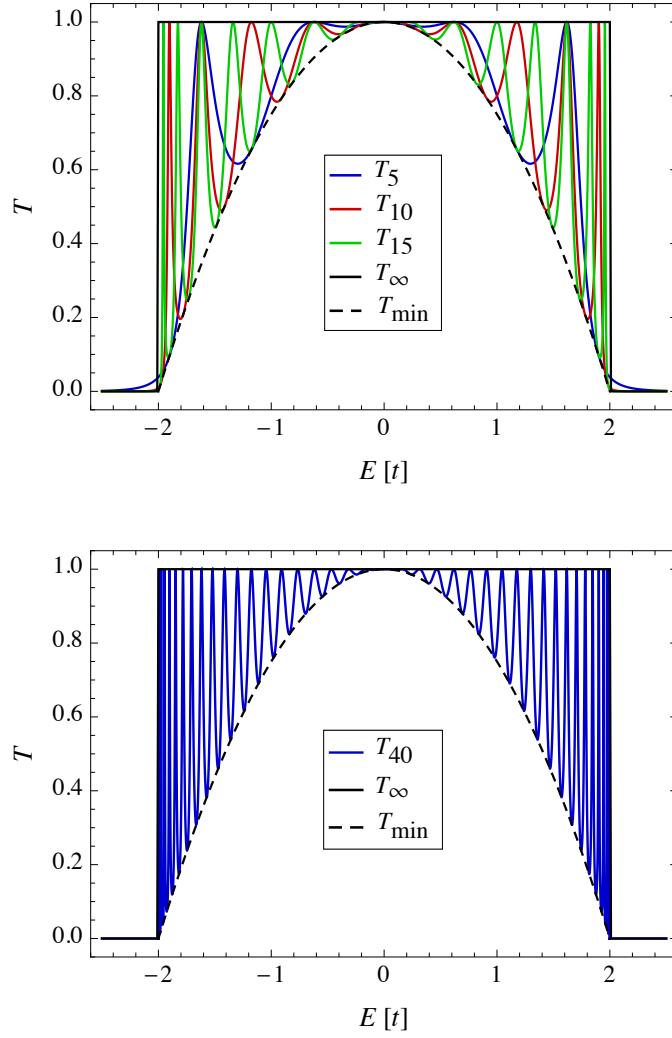
Figure 3.7: Transmission through homogeneous 1D tight-binding chains ($\varepsilon_i = 0$) of length $N = \{5, 10, 15\}$ (top) and $N = 40$ (bottom). When homogeneous semi-infinite chains ($\varepsilon_{\text{ch}} = 0$, $t_{\text{ch}} = \tau_{11} = 1$) are used as the reservoirs, the transmission T_∞ is independent of the chain length. Inside the conduction band it is perfect, outside it vanishes, because effectively an infinitely long perfect conductor is studied. When wide-band reservoirs ($\eta = 1$) are used, the transmission shows oscillations due to interference between the chain ends. Transmission resonances can be observed whenever the energy approaches an eigenenergy of the chain and thus, their number equals the chain length. The minimal conductance of homogeneous chains T_{min} is a reversed parabola.

Moreover, we learn from Figure 3.7 that the minimal transmission

$$T_{\min}(E) = \begin{cases} 1 - \left(\frac{E}{2}\right)^2 & \text{for } |E| \leq 2 \\ 0 & \text{for } |E| > 2 \end{cases} \qquad (3.20)$$

is a reversed parabola [201, Section 3.9.2.3]. In the band-center, we have perfect transmission independent of the chain length and independent of the contact model, because for the used parameters the self-energies are the same at $E = 0$. However, when we de-tune the parameters or leave the band-center $0 < |E| < 2$, the transmission (or the resistance) as a function of the chain length shows oscillations, see Figures 3.8 and 3.9. These oscillations, which have been observed experimentally in molecular wires [163], are caused by the increasing number of transmission resonances within the conduction band. Anyway, in contrast to a classical Ohmic conductor for which the resistance increases linearly with its length, we find that the quantum coherent resistance of a homogeneous tight-binding chain is length independent, apart from periodic oscillations. For wide-band reservoirs, the resistance increases exponentially outside the band $|E| > 2$, because the electrons can tunnel directly form the source to the drain, see Figure 3.9. For reservoirs modeled by semi-infinite chains, the resistance outside the band is infinite, because the reservoir's surface DOS vanishes there or, in other words, tunneling through an infinitely long system is impossible.
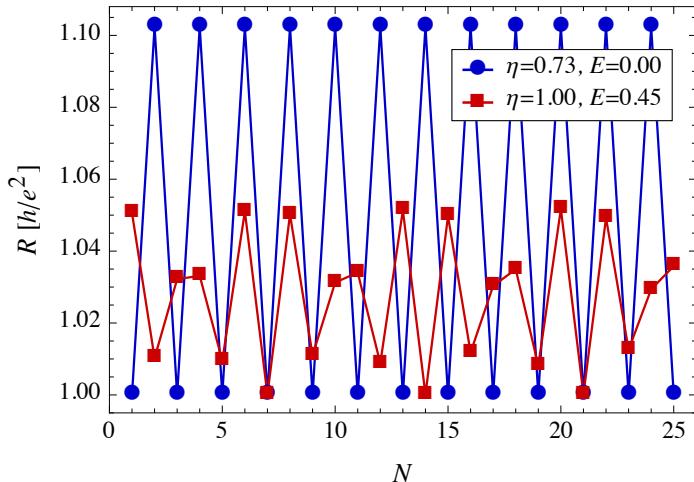
Figure 3.8: Resistance (inverse transmission) as a function of the chain length. When the parameters of the reservoirs are de-tuned $\eta \neq 1, t_{\text{ch}} \neq 1$ or when the band-center is left $E \neq 0$, the resistance oscillates with the chain length, which is due to the increasing number of resonances in the conduction band, see Figure 3.7.

Depending on the physical situation both contact models are useful. A constant length independent resistance is found in ballistic conductors as carbon nanotubes [14, 62], whereas transmission resonances appear when the current flow through single molecules is studied [39]. Moreover, the two contact models are not as different as it may appear. The transmission of a disordered chain in Figure 3.10 shows that both contact models give qualitatively the same result. The disorder, which is sketched in the inset by red bars, is

not necessarily random but may represent the electronic structure of the modeled system, see [39, Chapter 9]. The role of the contact models is discussed in detail in [184].
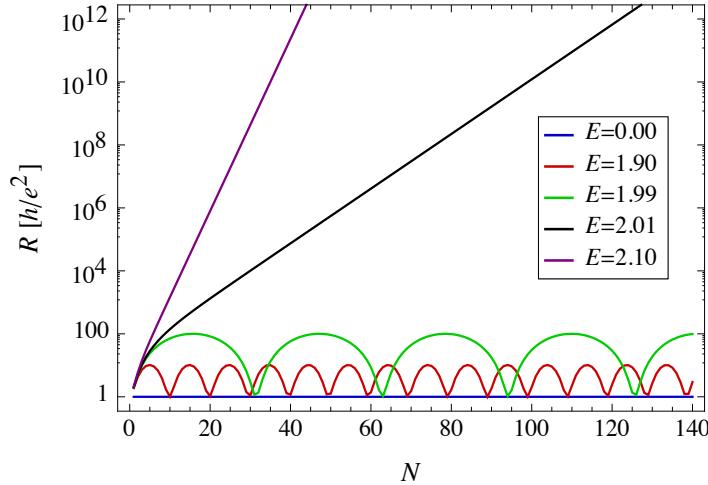
Figure 3.9: Resistance as a function of the chain length. Wide-band reservoirs with $\eta = 1$ are used. In the band-center $E = 0$ the resistance is length independent. Outside the band-center $0 < |E| < 2$ periodic oscillations are superimposed upon the constant resistance. Outside the conduction band $|E| > 2$, the resistance is increasing exponentially, because electrons can tunnel directly from the source to the drain.
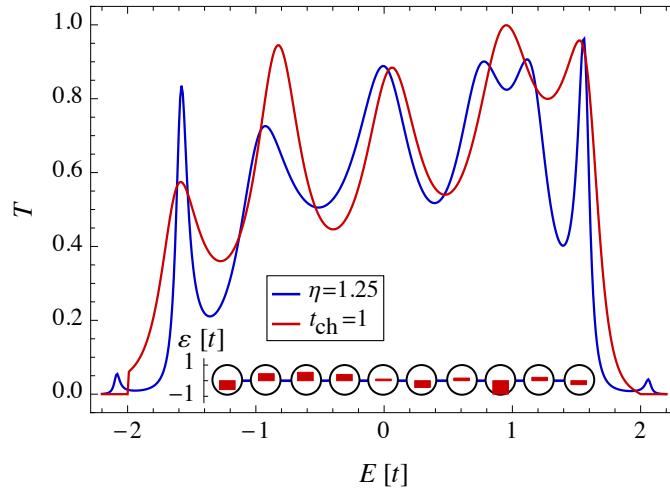
Figure 3.10: Transmission through a disordered 10 sites long chain. The onsite disorder is indicated in the inset by means of the red bars. Both, wide-band reservoirs (blue) as well as semi-infinite chains (red) show qualitatively the same behavior.

3.2.2 Anderson localization in disordered chains

We study the disorder averaged resistance of coherent tight-binding chains. The onsite energies ε_i are distributed independently according to a probability distribution $w(\varepsilon)$ with mean 0 and variance σ^2. In order to keep the equations clear and simple, we consider only the band-center $E = 0$ and use wide-band reservoirs with $\eta = 1$. The disorder averaged resistance (measured in multiples of h/e^2) of the coherent tight-binding chain of length N is given by the compact analytical formula

$$\langle R_N \rangle \equiv \left\langle \frac{1}{T_N} \right\rangle = \int \frac{1}{T_N} \prod_{i=1}^{N} w(\varepsilon_i) \mathrm{d}\varepsilon_i = \frac{1}{2} \left(1 + \alpha_+ \mathrm{e}^{N/\xi} + \alpha_- \mathrm{e}^{-N/\xi} (-1)^N \right), \quad (3.21)$$

where $\langle \cdot \rangle$ denotes disorder averaging and

$$2\alpha_\pm = 1 \pm \mathrm{sech}\left(\xi^{-1} \right), \quad (3.22)$$

$$\xi^{-1} = \ln \left(\frac{\sigma^2}{2} + \sqrt{\frac{\sigma^4}{4} + 1} \right). \quad (3.23)$$

A proof, which also includes the general case of arbitrary energies and arbitrary self-energies, can be found in the Appendix A.3.2. We published this proof in [167, 168].

In contrast to a classical disordered conductor, which is described in many cases by Ohm's law, we find that the resistance is increasing exponentially with the chain length. The contributions from a constant term as well as from an exponentially suppressed oscillatory term are irrelevant for $N \to \infty$. This exponentially increasing resistance is nothing but *Anderson localization* [9], which has been awarded by the Nobel prize in 1977. It can be explained by the destructive interference of the coherent electrons in the disorder potential, which traps the electrons and suppresses diffusion. Although Anderson localization has been studied for more than 50 years [56, 109], it is still an active field of research, see for example its recent experimental realization with ultracold atoms in optical lattices [12, 124].

The exponent $\xi^{-1} = \lim_{N\to\infty} \ln \langle R_N \rangle / N$ in (3.21) is the second-order generalized Lyapunov exponent. When not the resistance is averaged over disorder but its logarithm, which is the statistically well behaving quantity [10, 171], one also finds an exponentially increasing resistance, where the exponent $\lambda^{-1} = \lim_{N\to\infty} \langle \ln R_N \rangle / N$ is the localization length. Both quantities characterize the localization of the eigenstates in the disordered quantum system. They can be related to each other when single parameter scaling holds [202]. Note that when the disorder is switched off $\sigma \to 0$, we find the constant length independent resistance of a ballistic conductor. In the Section 4.5 the effect of decoherence on Anderson localization is studied.

3.2.3 Tight-binding ribbons and grids

We study the transport through tight-binding ribbons of length N and width M, which are described by the Hamiltonian

$$H = \sum_{i=1}^{N} \sum_{j=1}^{M} \varepsilon_{ij} |i,j\rangle \langle i,j| + \sum_{i=1}^{N-1} \sum_{j=1}^{M} t \big(|i,j\rangle \langle i+1,j| + \mathrm{H.c.} \big) + \sum_{i=1}^{N} \sum_{j=1}^{M-1} t \big(|i,j\rangle \langle i,j+1| + \mathrm{H.c.} \big).$$

$$(3.24)$$

The transmission[3] through a homogeneous tight-binding ribbon ($\varepsilon_{ij} = 0$) of width $M = 7$ and length $N = \{5, 10, 40\}$ is shown in Figure 3.11.
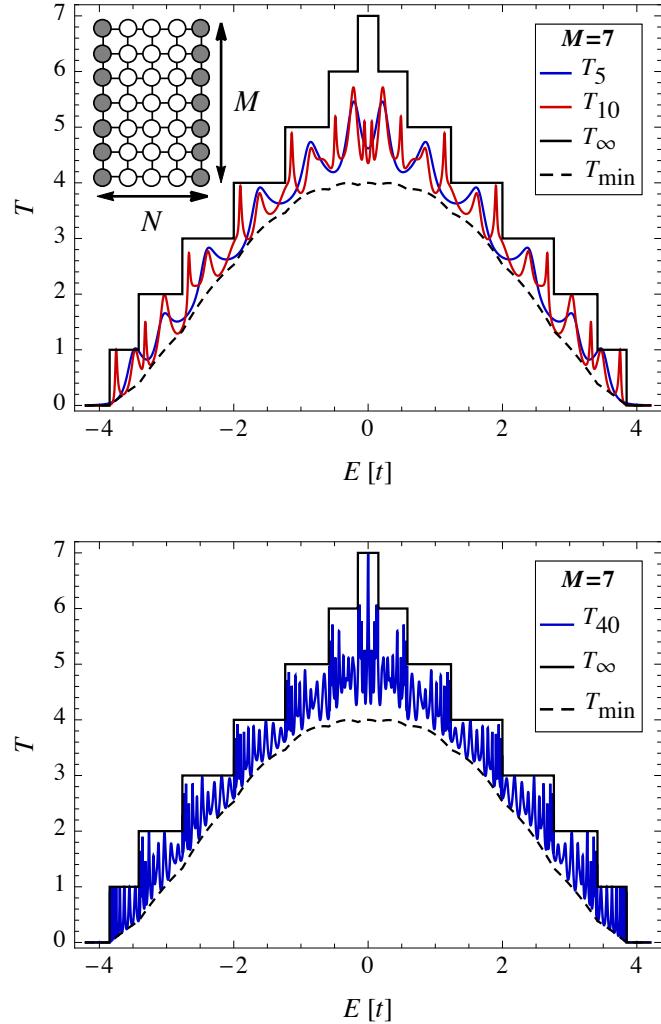
Figure 3.11: Transmission through a homogeneous tight-binding ribbon ($\varepsilon_{ij} = 0$) of width $M = 7$ and length $N = \{5, 10\}$ (top), $N = 40$ (bottom). The 5 sites long ribbon is sketched in the inset, where the gray shaded sites at the edges are connected to the reservoirs. When homogeneous semi-infinite ribbons ($\varepsilon_{\mathrm{ch}} = 0$, $t_{\mathrm{ch}} = \tau = 1$) are used as the reservoirs, the transmission T_∞ is independent from the ribbon's length. As a function of energy, T_∞ changes in steps, whose number equals $2M$. This conductance quantization as well as the minimal transmission T_{min} (of a ribbon with any length N but fixed width M) can be understood by decoupling the ribbon into independent, energy shifted 1D chains. When wide-band reservoirs ($\eta = 1$) are used, the transmission shows multiple resonances due to interference.

---

[3]Note that the transmission through a ribbon is in general not determined by a single matrix element of the Green's function, like in the case of 1D chains (3.19), but by a few of them according to (2.33). Also in this case, it is computationally more efficient to calculate these matrix elements by solving linear equation systems instead of inverting a whole matrix.

When homogeneous semi-infinite ribbons ($\varepsilon_{\text{ch}} = 0$, $t_{\text{ch}} = \tau = 1$) of the same width are used as the reservoirs, we find a staircase behavior. This *conductance quantization* can be understood easily, when we remind ourselves that the ribbon can also be considered as M independent, energy shifted 1D chains, see (3.7). The transmission $T_j = 1$ of each chain is perfect in its conduction band $|E - 2\cos(\pi j/(M+1))| < 2$ and vanishes outside. Thus, the transmission of the ribbon is given by the number of individual chains for which the Fermi energy lies in the conduction band

$$
T_\infty^M(E) = \begin{cases} \left\lceil \frac{M+1}{\pi} \arccos\left(\frac{|E|}{2} - 1\right) \right\rceil - 1 & \text{for } |E| \leq E_{\text{max}}^M, \\ 0 & \text{for } |E| > E_{\text{max}}^M, \end{cases} \tag{3.25}
$$

where $E_{\text{max}}^M = 2 + 2\cos(\pi/(M+1)) \xrightarrow{M \to \infty} 4$ is the edge of the ribbon's conduction band. These staircases have been observed in quantum point contacts [18, 177, 182], in quantum wires [45, 189] realized in semiconductor heterostructures, in chains of individual atoms [138] and in graphene ribbons [176]. When wide-band reservoirs are used, the transmission shows multiple resonances, which are an interference effect as in the 1D case. In the same way, summing up the minimal transmission (3.20) of each of the independent 1D chains, gives the minimal transmission of a ribbon with any length N but fixed width M

$$
T_{\text{min}}^M(E) = \sum_{j=1}^M T_{\text{min}}\left(E - 2\cos\left(\frac{\pi j}{M+1}\right)\right). \tag{3.26}
$$

Taking the limit $M \to \infty$, the transmission per width of the 2D tight-binding grid reads

$$
T^{2\text{D}}(E) \equiv \lim_{M \to \infty} \frac{T_\infty^M}{M} = \frac{1}{\pi} \arccos\left(\frac{|E|}{2} - 1\right) \tag{3.27}
$$

and its minimal transmission per width is given by

$$
T_{\text{min}}^{2\text{D}}(E) \equiv \lim_{M \to \infty} \frac{T_{\text{min}}^M}{M} = \frac{1}{\pi} \int_0^\pi d\phi \, T_{\text{min}}\left(E - 2\cos(\phi)\right)
$$

$$
= \begin{cases} \frac{2+3|E|}{4\pi} \sqrt{1 - \left(\frac{|E|}{2} - 1\right)^2} + \frac{2-|E|^2}{4\pi} \arccos\left(\frac{|E|}{2} - 1\right) & \text{for } |E| \leq 4, \\ 0 & \text{for } |E| > 4. \end{cases} \tag{3.28}
$$

Figure 3.12 shows the maximal and minimal transmission per width of the homogeneous tight-binding grid, as well as the transmission per width through a ribbon of length $N = 600$ and width $M = 200$ connected to wide-band reservoirs. The resonances are much less pronounced compared to the ribbon with $N = 40$, $M = 7$ shown in Figure 3.11 (bottom), because the wide-band reservoirs at the 200 sites long edges of the ribbon add some energy broadening to the system and thereby, suppress interference. This effect is used in Chapter 5 to suppress spurious interference by additional virtual reservoirs at the boundaries of the system.

The resistance of a 7 sites wide ribbon as a function of its length is shown in Figure 3.13. It confirms that quasi 1D ribbons show essentially the same behavior as 1D chains. For

homogeneous ribbons ($\sigma = 0$) connected to wide-band reservoirs (solid curves), the resistance is constant apart from periodic oscillations due to interference. These oscillations vanish, if semi-infinite ribbons are used as the reservoirs (dashed curve). For disordered ribbons ($\sigma > 0$), the resistance shows Anderson localization. Note that also disordered 2D tight-binding grids show Anderson localization, although the localization length can be quite large at weak disorder, which makes numerical studies demanding [2, 56, 74].
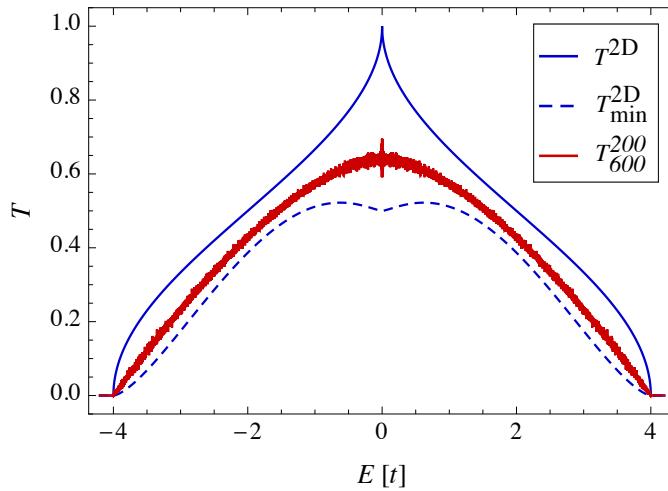

Figure 3.12: Maximal and minimal transmission per width of the homogeneous 2D tight-binding grid. The transmission per width through a ribbon of length $N = 600$ and width $M = 200$ is also shown. The resonances are suppressed by the energy broadening of the wide-band reservoirs at the 200 sites wide edges of the ribbon. The energy resolution is $\Delta E = 10^{-4}$.

3.3 Conclusions

In this Chapter, we have studied tight-binding lattices, like 1D chains, quasi-1D ribbons and 2D grids. Starting with electronic structure calculations, we have shown that these lattices have cosine energy bands. The critical points in the cosine bands can lead to van Hove singularities in the DOS, see Figures 3.1 and 3.2. Reservoirs for transport studies have to provide a continuous DOS, which is occupied according to an energy distribution function. We have shown that semi-infinite lattices can be used as a reservoir model and have calculated the self-energy for chains (3.13) and ribbons (3.16). For studies of tight-binding ribbons, it has been proven to be useful to decouple the ribbon into independent, energy shifted 1D chains. Also the computationally less expensive wide-band reservoirs (3.17) have been introduced, which assume an energy independent DOS at the reservoir's surface. Both contact models give physically reasonable results for many systems.

In the second part of this Chapter, coherent transport has been studied. We have shown that the transport through homogeneous lattices is ballistic within the conduction band. The resistance is length independent, even though periodic oscillations can be superimposed, see Figures 3.9 and 3.13. These oscillations are due to interference of the coherent
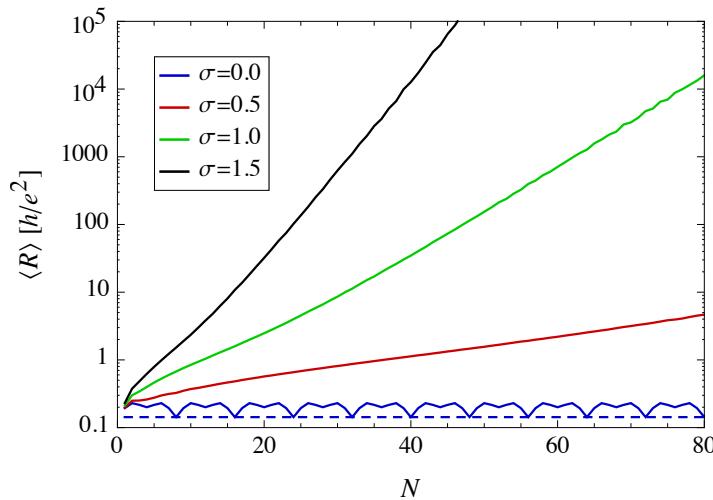
Figure 3.13: Disorder averaged resistance of a tight-binding ribbon of width $M = 7$ as a function of its length ($E = 0$). For homogeneous ribbons ($\sigma = 0$) connected to wide-band reservoirs (solid curves), periodic oscillations are superimposed upon the constant resistance. These oscillations vanish, if semi-infinite ribbons are used as the reservoirs (dashed curve). When disorder ($\sigma > 0$) is introduced, Anderson localization is indicated by an exponentially increasing resistance. Averages were taken over $N \cdot 10^4$ disorder configurations.

electrons, which also causes resonances in the energy resolved transmission, see Figure 3.7 and 3.11. When infinitely long homogeneous ribbons are studied (by using semi-infinite homogeneous lattices as the reservoirs), the oscillations and resonances vanish. The energy resolved transmission shows then quantized plateaus. In disordered lattices the coherent electrons are Anderson localized, which is indicated by an exponential increase of the resistance with the system length. We have derived a compact analytical formula for the disorder averaged coherent resistance of a 1D chain (3.21).

All these novel quantum effects – ballistic transport, conductance quantization, transmission resonances, and Anderson localization – can be observed experimentally. However, the common Ohm's law cannot be observed in quantum coherent systems. In the following Chapter, we study if these novel quantum transport properties are stable under the effect of decoherence and, if Ohm's law can be reached.

4 Effects of decoherence on transport

In this Chapter, the effects of decoherence on electron transport in nanosystems are studied. We start with a short introduction, in which we address the question, why it is necessary to take into account decoherence in nanosystems. An overview of existing decoherence approaches is also given. In Section 4.2, we introduce a novel statistical model for the effects of decoherence. This model is applied in the following Sections to tight-binding lattices in order to study its properties and advantages. We show that these lattices go from the quantum to the classical regime, when decoherence is introduced. We also test some model variations and compare the model with existing approaches. In Section 4.5, the effects of decoherence on Anderson localization are investigated. We show that the spatial distribution of decoherence has observable effects on transport. In Section 4.6, we introduce an extension of the decoherence model, which allows to tune the degree of phase and momentum randomization independently and hence, to obtain pure dephasing. The Chapter is closed with an outlook on how our model can be used to study the effects of decoherence on the transport of spin polarized electrons. We have published partially the results of this Chapter in [167, 168, 170].

4.1 Decoherence in nanosystems

The transport through nanosystems takes place in an intermediate regime between classical and quantum transport, because several relevant lengths – mean free path, phase coherence length, Fermi wavelength, localization length, system size – can have the same order of magnitude. The essential mechanism for the transition from the quantum to the classical regime is the decoherence of the conduction electrons, i.e. the randomization of their phase and momentum. When the phase coherence is lost, the electrons cannot interfere anymore and behave as classical particles. Therefore, in order to describe the transport through nanosystems correctly, it is necessary to take into account some degree of decoherence. Decoherence is caused by interactions of the conduction electrons with the environment. This could be, for example, a surrounding phonon bath, which causes phase breaking scattering in the system. From another point of view, the interactions with the environment can be understood as an increasing entanglement of the conduction electrons. When the environmental degrees of freedom are traced out in order to obtain a reduced density matrix for the electron systems, this goes along with a loss of information and the decoherence of the electrons. A detailed discussion on "decoherence and the appearance of a classical world in quantum theory" can be found in [95].

There are many decoherence models in the literature. Basically already the nonequilibrium Green's function approach, as introduced in Chapter 2, allows to take into account arbitrary phase breaking interactions by suitable self-energies. Datta proposed, for example, self-energies for the electron-phonon and electron-electron interaction by using the first-order self-consistent Born approximation, see [36, 72] and [43, Chapter 10]. Work in this direction

has also been done in [19, 38, 80]. However, as this approach requires generally high computational effort, it is limited to relatively small systems.

Büttiker proposed to use virtual reservoirs as a model for the effects of decoherence [26, 28], where the electrons are absorbed and reinjected after randomization of their phase and momentum. As the electrons in the decoherence reservoirs are considered as uncorrelated, they can be characterized by single-particle energy distribution functions $f_i(E)$. The distribution functions are determined by the condition that virtual reservoirs cannot provide a net current flow. Conceptually, these so-called *Büttiker probes* can be considered as additional voltage probes and can be handled by the multi-terminal formula (2.40) derived in Section 2.4. Note that this apparently phenomenological approach can be justified from microscopic theories, see [85], [121, Section III.C], and [42, Section 8.7]. In order to model a continuous loss of the electron phase, D'Amato and Pastawski [40] used Büttiker's idea and attached a homogeneous distribution of these decoherence reservoirs to the system, see Figure 4.1. Roy and Dahr [156] extended this model to a finite bias voltage and finite temperature bias in order to study current and heat transport under the effect of decoherence. Homogeneous distributions of attached Büttiker probes are used in several publications, see e.g. [5, 32, 64, 65, 77, 115, 133, 134, 194]. Büttiker's original idea is also used [104, 113, 119, 120, 161, 195]. A drawback of Pastawski's model is that a coherent transmission between every pair of the N reservoirs has to be calculated and a $N \times N$ system of linear equations has to be solved, see (2.40). Thus, the computational effort increases quadratically with the system size.

Other decoherence models use the Lindblad master equation and take into account the effects of decoherence by suitable Lindblad operators [51, 95, 145, 151, 205, 206]. Also stochastic absorption through an attenuating factor [96] or random phase factors [139, 140, 199] are used, which are still controversially discussed [16]. However, a common feature of all of these decoherence models is that they assume a continuous loss of the electron phase.
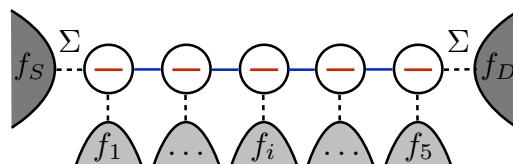
Figure 4.1: In Pastawski's decoherence model, virtual reservoirs (Büttiker probes) are attached to all sites of a tight-binding chain in order to model a continuous loss of the electron phase.

4.2 Statistical model for the effects of decoherence

We introduce a novel statistical model for the effects of decoherence on electron transport, which has been proposed recently by M. Zilly et al. [201–203]. In this thesis, the model is developed further and applied to various nanosystems. Our aim is a simple phenomenological model, which on the one hand takes into account decoherence correctly but on the other hand is computationally less expensive than existing approaches in order to be applicable to realistic systems. We will also see that its simplicity allows to solve some transport problems analytically and to gain deeper understanding of the system properties.

The statistical decoherence model is the following:

- *Decoherence regions* are distributed spatially over the quantum system according to a given probability distribution function. We focus on random distributions without spatial correlations, which correspond not only to spatially fixed phase breaking scatterers but also to dynamical decoherence processes like electron-phonon scattering, see below. In general, we allow for arbitrary spatial decoherence distributions, depending on the considered microscopic decoherence process.

- The electron phase is randomized *completely* at these decoherence regions, which are modeled by Büttiker probes and characterized by energy distribution functions f_i. In general, the momentum of the electrons is also randomized, while we assume that no energy relaxation takes place, which is justified for electron transport at the Fermi energy. In one-dimensional systems the model can be extended to obtain *pure dephasing* [170], i.e. randomization of the phase but conservation of energy and momentum, see Section 4.6.

- The transport in between these decoherence regions is assumed as quantum coherent. As virtual Büttiker probes can be handled computationally in the same way as real voltage probes, for a given decoherence configuration, the current through the system can be calculated by the multi-terminal formula (2.40).

- *Statistical approach*: Afterwards, the transport quantity of interest, e.g. the resistance or the conductance, is ensemble averaged over spatial decoherence configurations. According to the ergodic hypothesis, averaging the resistance corresponds to experiments where the current through the system is fixed and the voltage drop is measured. When the conductance is ensemble averaged it is vice versa.

- The phase coherence length is determined by the average distance of the decoherence regions.

In order to make our model more transparent, we apply it in the next Sections to tight-binding lattices. Its properties and advantages are studied in detail. We also test some model variations and compare our model with other approaches.

4.3 Application of the statistical decoherence model to tight-binding chains

The statistical decoherence model is applied to 1D tight-binding chains of length N. Assuming complete phase and momentum randomization at the decoherence reservoirs, we replace bonds of the chain by couplings to virtual completely phase and momentum randomizing reservoirs. This limits the coherent transmission to nearest neighbors and subdivides the chain into smaller coherent subsystems, see Figure 4.2. Simplifying (2.40) under this constraint, the resistance of a fixed decoherence configuration is the sum of the quantum coherent subsystem resistances (measured in multiples of h/e^2)

$$R = \sum_{i=0}^{N_d} \frac{1}{T_{i+1,i}}, \tag{4.1}$$

where N_d is the number of decoherence reservoirs. Afterwards, an ensemble average $\{\cdot\}$ over the spatial decoherence configurations is calculated.
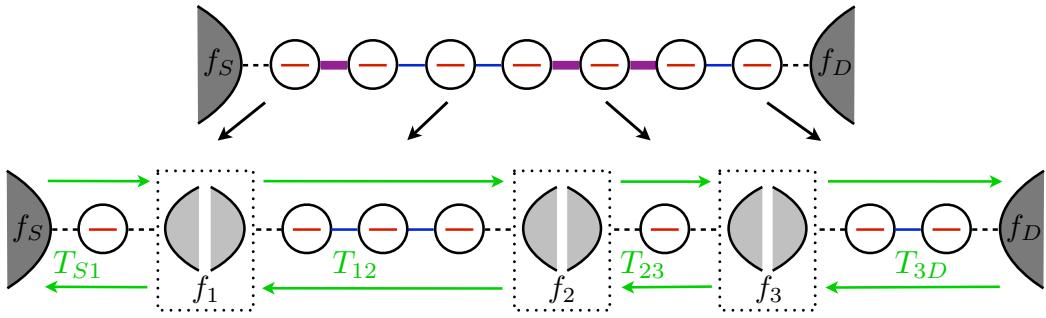
Figure 4.2: In our statistical decoherence model, bonds of the tight-binding Hamiltonian are replaced by couplings to completely phase and momentum randomizing reservoirs, which limits the coherent transmission to nearest neighbors (green arrows) and subdivides the chain into smaller coherent subsystems.

For reasons, which will become clear later, let us derive (4.1) also explicitly. As the energy resolved current is conserved at the N_d virtual decoherence reservoirs, their distribution functions f_i are determined by

$$T_{i,i-1}\left(f_{i-1}-f_i\right) - T_{i+1,i}\left(f_i - f_{i+1}\right) \overset{!}{=} 0. \tag{4.2}$$

The solution of this system of N_d linear equations reads

$$f_i - f_D = \frac{\sum_{k=i}^{N_d} \frac{1}{T_{k+1,k}}}{\sum_{k=0}^{N_d} \frac{1}{T_{k+1,k}}}\left(f_S - f_D\right). \tag{4.3}$$

Using this result in the Landauer-Büttiker formula (2.32)

$$I = \frac{e}{h}\int \mathrm{d}E\, T_{D,N_d}\left(f_{N_d} - f_D\right) = \frac{e}{h}\int \mathrm{d}E\, \frac{f_S - f_D}{\sum_{k=0}^{N_d}\frac{1}{T_{k+1,k}}} \tag{4.4}$$

and taking the limit of an infinitesimal bias voltage, we arrive at (4.1).

Focussing on random uncorrelated decoherence distributions, we replace the bonds of the chain randomly with probability p. However, we also allow for other decoherence distributions under the constraint that on average $\{N_d\} = (N-1)\,p$ decoherence regions are introduced in the system. In this way, we will also study the homogeneous distribution of decoherence reservoirs and random distributions with a cut-off. The *degree of decoherence* p can be related to the average subsystem size and thereby, defines the phase coherence length

$$\ell_\phi = \frac{N}{1+(N-1)\,p} \xrightarrow{N\to\infty} \frac{1}{p}. \tag{4.5}$$

Our statistical decoherence model reduces the computational effort compared to other models, which attach virtual reservoirs to every site of the chain. Instead of calculating the transmission function between every pair of reservoirs, we have to evaluate it only between nearest neighbors. Moreover, instead of solving the linear equation system in (2.40), we can simply sum up the subsystem resistances. The decoherence average increases the computation time but it can be parallelized efficiently by distributing to each processor a decoherence configuration. We will also see that in some situations the transport problem can be solved analytically, which gives deeper insight into the underlying physics.

4.3.1 Homogeneous chains: The ballistic-to-Ohmic transition

Studying homogeneous chains, the resistance of a given decoherence configuration does not depend on the positions of the subsystems in the chain but only on their number of occurrence. From elementary combinatorics, we know that a chain of total length N remains coherent with probability $(1-p)^{N-1}$. A subsystem of length $j < N$ appears with probability $p(1-p)^{j-1}$ at one of the two chain ends, while inside the chain it appears with probability $p^2(1-p)^{j-1}$ at one of the $N-1-j$ possible positions. Hence, the average number of subsystems with length j in a chain of N sites is given by

$$u_j^N = e^{-(j-1)/\ell} \begin{cases} 2p + (N-1-j)\,p^2 & \text{for } j < N, \\ 1 & \text{for } j = N, \end{cases} \tag{4.6}$$

where

$$\ell^{-1} = -\ln(1-p)\,. \tag{4.7}$$

The decoherence averaged resistance reads

$$\{R\} = \left\{ \sum_{i=0}^{N_d} \frac{1}{T_{i+1,i}} \right\} = \sum_{j=1}^{N} u_j^N \frac{1}{T_j}\,, \tag{4.8}$$

where T_j is the coherent transmission through a chain of length j. In the previous Chapter 3, we found that for reservoirs modeled by homogeneous semi-infinite chains ($\varepsilon_{\mathrm{ch}} = 0$, $t_{\mathrm{ch}} = 1$) the transmission is perfect $T_j = 1$ inside the conduction band. Also for wide-band reservoirs with $\eta = 1$, the transmission is perfect in the band-center. In these cases, we obtain for the decoherence averaged resistance the simple analytical expression

$$\{R\} = \{1 + N_d\} = \sum_{j=1}^{N} u_j^N = 1 + (N-1)\,p\,. \tag{4.9}$$

The resistance increases linearly with the chain length, if a finite degree of decoherence $p > 0$ is introduced. Thus, by introducing decoherence, i.e. phase *and* momentum randomization, the system goes from the quantum-ballistic to the classical-Ohmic regime. The decoherence averaged transmission cannot be calculated analytically that easily. However, numerical averages over 10^4 decoherence configurations in Figure 4.3 show that this transition occurs for decoherence averages over the resistance as well as over the transmission. Note that the numerical averaged resistance agrees with the exact result (4.9). The resistance in the case of averaging the transmission is always less than in the case of averaging the resistance directly. The reason for this behavior are "rare events", i.e. improbable decoherence configurations with high resistance, which have a noticeable effect on the decoherence average of the resistance but negligible effect on the decoherence average of its inverse, the transmission.

We proceed our studies with tight-binding chains, which are connected to wide-band reservoirs. By means of the exact expression for the resistivity of coherent chains derived in Appendix A.3.1 and (4.6), we can calculate for arbitrary self-energies the decoherence averaged resistance. However, as the expressions are quite large, we restrain ourselves to numerical evaluations. In Figure 4.4 we show that the resistance oscillations, which are due to the interference of the coherent electrons (compare also with Figure 3.8), are suppressed by decoherence and a linearly increasing Ohmic resistance is found.
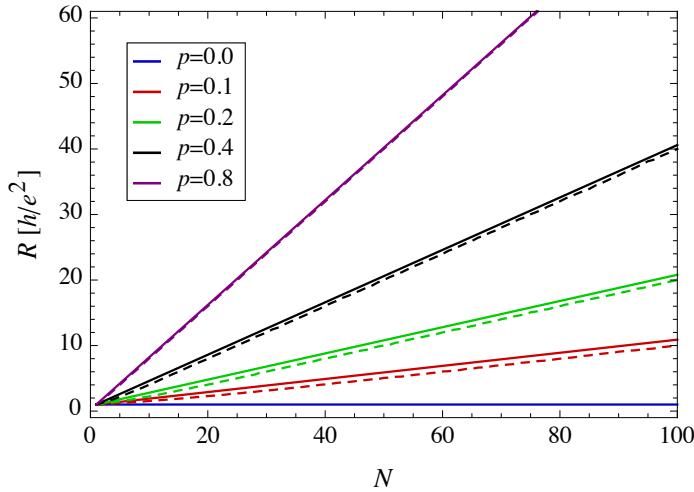
Figure 4.3: Resistance of a tight-binding chain in the band-center $E = 0$ as a function of its length. The system goes from the quantum-ballistic regime to the classical-Ohmic regime, if a finite degree of decoherence $p > 0$ is introduced. This transition occurs for the decoherence average over the resistance (solid curves, (4.9)) as well as over the transmission (dashed curves). Numerical averages are over 10^4 decoherence configurations.
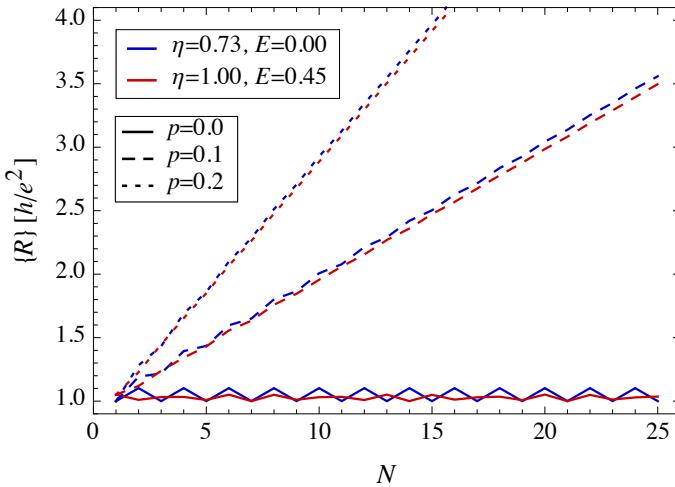
Figure 4.4: Using wide-band reservoirs, the quantum-coherent resistance oscillates with the chain length, because of interference (compare with Figure 3.8). These oscillations are suppressed by decoherence and a classical Ohmic resistance is found, which increases linearly with the chain length.

Figure 4.5 shows the decoherence averaged energy distribution function $\{f_i\}$ (4.3) along a 20 sites long homogeneous chain. The spatial evolution of $\{f_i\}$, which after averaging over spatial decoherence configurations can be assigned to every bond, corresponds to the quasi-Fermi level within the chain. In the coherent chain $p = 0$,[1] the quasi-Fermi level drops steeply at the interfaces to the source and drain reservoir but it is totally flat inside. As the electric potential follows the quasi-Fermi level,[2] we conclude that the resistance is located at the interfaces, whereas no voltage drop occurs inside. This is the so-called *contact resistance* of ballistic conductors [42, Section 2.1]. When decoherence is introduced $p > 0$, the quasi-Fermi level (or electrical potential) drops linearly along the chain, as expected for an Ohmic conductor.
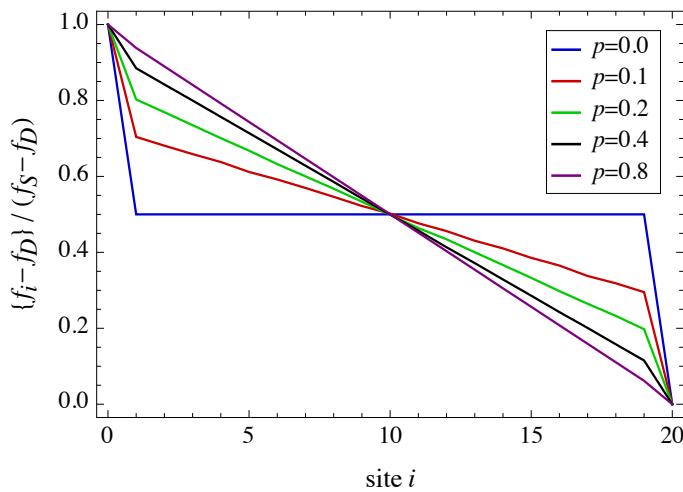

Figure 4.5: Decoherence averaged energy distribution function (or quasi-Fermi level) along a 20 sites long homogeneous chain ($E = 0$). If the transport is coherent $p = 0$, the quasi-Fermi level drops at the interfaces to the reservoirs, whereas it is flat inside. The resistance of a ballistic conductor is caused solely at the interfaces. When decoherence is introduced $p > 0$, the quasi-Fermi level drops linearly, as expected for an Ohmic conductor. Averages are over those of 10^5 decoherence configurations, for which the ith bond is replaced by a decoherence reservoir.

The resistivity $\rho \equiv \lim_{N \to \infty} R/N$ as a function of the degree of decoherence p is shown in Figure 4.6 for various energies E and wide-band parameters η. For $\eta = 1$ and $E = 0$ the resistivity increases linearly with p, as expected from (4.9). However, for $\eta \neq 1$ and $E \neq 0$, we find that the resistivity can increase non-linearly and even decrease with increasing degree of decoherence. The resistivity in the band-center as a function of η is shown in Figure 4.7. It is minimal at $\eta = 1$, because in this case the reservoirs are equivalent to homogeneous semi-infinite chains and therefore, match perfectly. For $\eta \neq 1$ the resistivity increases symmetrically around its minimum, i.e. $\{\rho(\eta)\} = \{\rho(1/\eta)\}$.

---

[1]To apply our model, we assume also in the coherent case an infinitesimal degree of decoherence $p = 10^{-3}$.

[2]The electric potential is given by the convolution of the Green's function of the Poisson equation with the charge density, which in turn is proportional to the quasi-Fermi level. As convolution means averaging, the electric potential follows the quasi-Fermi level except that it is smoothed out over some screening length, see for details [42, Section 2.3]. Using the Hartee approximation for the electron-electron interaction, the self-consistent electric potential in coherent systems is studied in [166].
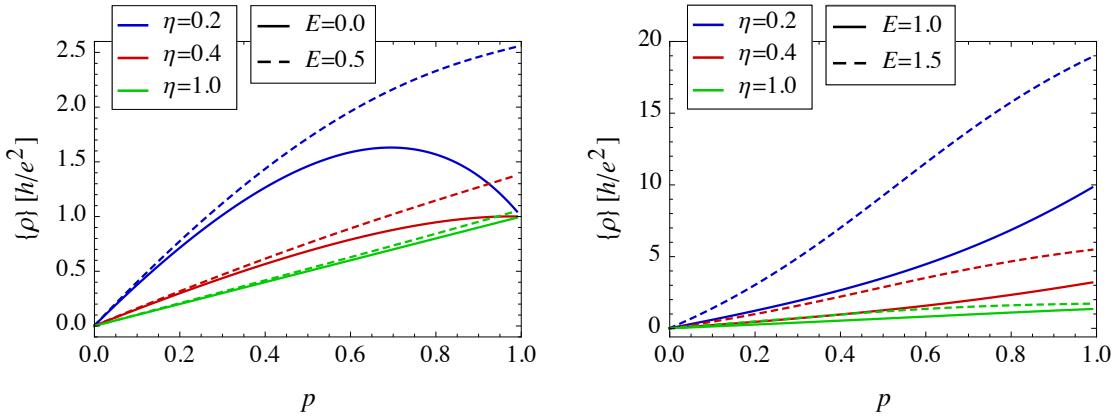
Figure 4.6: Decoherence averaged resistivity $\{\rho\}$ as a function of the degree of decoherence p for various wide-band parameters η and energies E. In the band-center and for $\eta = 1$ the resistivity increases linearly with p. For other parameters the resistivity can increase non-linearly and even decrease with p.
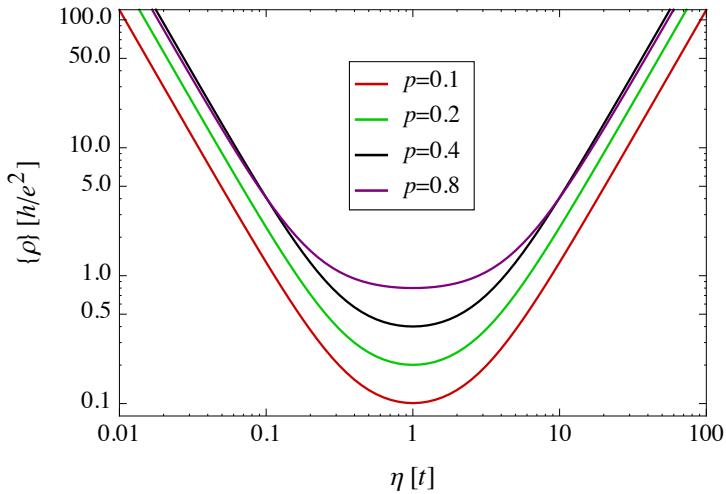
Figure 4.7: The decoherence averaged resistivity $\{\rho\}$ in the band-center $E = 0$ as a function of the wide-band parameter η. For $\eta = 1$ the resistivity is minimal, because the reservoirs match perfectly. For $\eta \neq 1$ the resistivity increases symmetrically around its minimum, i.e. $\{\rho(\eta)\} = \{\rho(1/\eta)\}$.

4.3.2 Disordered chains: Suppression of transmission resonances

Figure 4.8 shows the effect of decoherence on the transmission through a 10 sites long chain with the same disorder as in Figure 3.10. The solid curves have been obtained by averaging the resistance, whereas for the dashed curves the transmission has been averaged. Note that the results, although qualitatively the same, correspond to different experimental situations, i.e. measuring the voltage or the current. The real reservoirs and the decoherence reservoirs are modeled in the wide-band approximation with $\eta = 1$. Averages were taken over 10^4 decoherence configurations. We observe that the oscillations in the transmission

are reduced, because interference is suppressed by decoherence. However, also the average transmission is reduced, which indicates the additional resistance due to momentum randomization at the decoherence regions. A similar behavior can be found in [16, 72, 119]. In Section 4.6 we show, how momentum conserving decoherence can be obtained in a modified model.
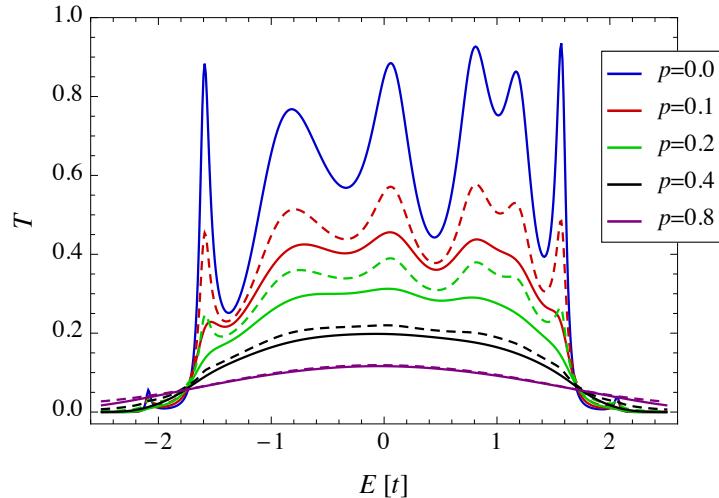
Figure 4.8: The effect of decoherence on the energy resolved transmission of a 10 sites long chain with the same disorder as in Figure 3.10. The solid curves have been obtained by averaging the resistance, whereas for the dashed curves the transmission has been averaged. 10^4 decoherence configurations have been used for the averages. When the degree of decoherence p is increased, the oscillations in the transmission are reduced as the interference of the electrons is suppressed. Also the average transmission is reduced, which indicates the additional resistance due to momentum randomization at the decoherence reservoirs. All reservoirs are modeled in the wide-band approximation with $\eta = 1$.

4.3.3 Effect of the spatial decoherence distribution and the assumption of complete phase and momentum randomization

Let us discuss, how the assumption of complete phase and momentum randomization at the decoherence reservoirs as well as their spatial distribution changes the behavior of the system. Figure 4.9 shows the energy resolved transmission through the 10 sites long disordered chain, which has already been studied in Figures 3.10 and 4.8. Averaging the resistance over 10^4 decoherence configurations, for the dashed red and black curve the bonds of the Hamiltonian have been replaced with decoherence reservoirs as discussed before. Using the same ensemble, for the solid red and black curve we have attached the decoherence reservoirs only to the chain, see Figure 4.10. As phase and momentum are randomized only partially at these attached reservoirs, the coherent transmission between all reservoirs has to be taken into account. In general, this increases the computational effort and restricts us to numerical calculations by means of the multi-terminal formula (2.40). The green and purple curve have been obtained by attaching at every site of the

chain a wide-band reservoir with η', which corresponds to Pastwaski's decoherence model, see Figure 4.1. We find that all decoherence models show qualitatively the same behavior, i.e. suppression of the transmission resonances and a reduction of the average value.
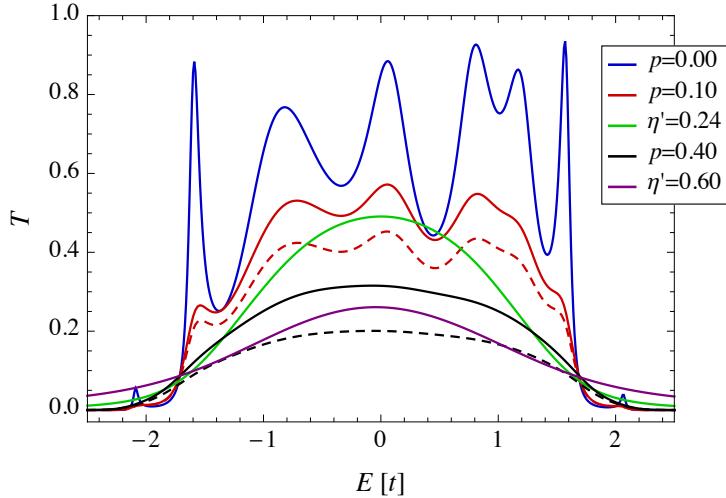
Figure 4.9: Effect of decoherence on the energy resolved transmission of the 10 sites long disordered chain, studied already in Figures 3.10 and 4.8. Averaging the resistance over an ensemble of 10^4 decoherence configurations, for the solid red and black curve we have attached the decoherence reservoirs ($\eta = 1.0$) only to the chain, whereas for the dashed curves the bonds have been replaced. For the green and purple curve we have attached to every site a wide-band reservoir with η'. All decoherence models show qualitatively the same behavior, i.e. suppression of the resonances and decrease of the average value.
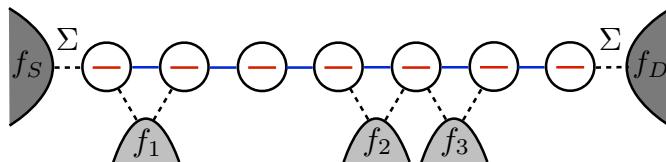
Figure 4.10: A variation of our model is to attach the decoherence reservoirs only to the chain. When the reservoirs are attached to every site, Pastawski's decoherence model is obtained, see Figure 4.1.

The effect of these decoherence models on the resistance of a homogeneous tight-binding chain as a function of its length is shown in Figure 4.11. We observe in all cases a decoherence-driven transition from the quantum-ballistic to the classical-Ohmic regime, although the precise value of the resistivity (slope of the curves) depends on the details of the models, as expected. In Section 4.3.1 we have shown that in some situations the decoherence averaged resistance of homogeneous chains can be calculated analytically, see (4.9). It turns out that in these cases the resistance is independent of the spatial distribution of the decoherence reservoirs and determined completely by their average number. However, this is true only for homogeneous chains. In Section 4.5, we show that the decoherence distribution affects the transport in disorder averaged chains.
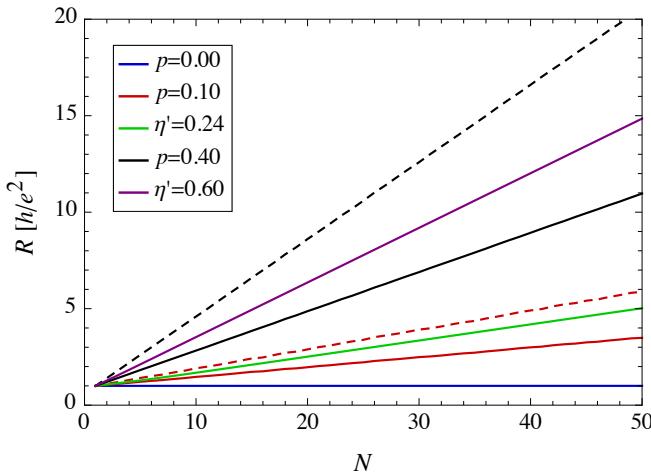
Figure 4.11: Resistance of a homogeneous tight-binding chain as a function of its length ($E = 0$). Although the resistivity (slope of the curves) depends on the details of the decoherence models, we find in all cases a decoherence-driven transition from the ballistic to the Ohmic regime. The color coding and the parameters are the same as in Figure 4.9.

4.4 Application of the statistical decoherence model to tight-binding ribbons

We discuss the application of our statistical decoherence model to tight-binding ribbons of length N and width M. In the same way as for 1D chains, completely phase and momentum randomizing regions are distributed spatially over the system by replacing randomly selected bonds of the tight-binding Hamiltonian with decoherence reservoirs, see the inset of Figure 4.12. Afterwards, an ensemble average over spatial decoherence configurations is calculated. In contrast to 1D chains, a subdivision into smaller coherent subsystems is in general not possible, which restrains us to numerical evaluation of the multi-terminal formula (2.40). However, our statistical decoherence model can still be applied more efficiently than models, which attach decoherence reservoirs to every site of the system. In our model, the decoherence reservoirs are introduced in average only at the fraction p of all bonds, which reduces the number of transmission functions to be calculated in (2.40) as well as the dimension of the linear equation system in (2.40). The decoherence average can be parallelized by distributing to each processor a decoherence configuration.

Figure 4.12 shows the effect of decoherence on a homogeneous tight-binding ribbon of length $N = 25$ and width $M = 5$. Source and drain are modeled by semi-infinite ribbons, whereas for the decoherence reservoirs the wide-band approximation is used. The transmission plateaus are suppressed with increasing degree of decoherence p. Its average value is also reduced, which indicates the additional resistance due to momentum randomization. The resistance of a homogeneous tight-binding ribbon as a function of its length is shown in Figure 4.13. As in the case of 1D chains, the ribbon goes from the ballistic to the Ohmic regime for any finite degree of decoherence. The quasi-Fermi level inside a ribbon, see Figure 4.14, drops entirely at the interfaces to the reservoirs in the case of coherent transport. Under the effect of decoherence the linearly decreasing quasi-Fermi level of an Ohmic conductor is found.
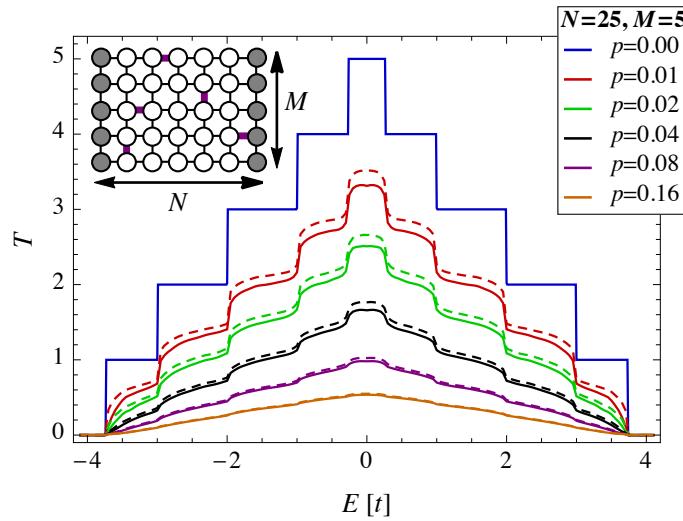
Figure 4.12: Effect of decoherence on the transmission of a homogeneous tight-binding ribbon of length $N = 25$ and width $M = 5$. Source and drain are modeled by semi-infinite ribbons ($\varepsilon_{\rm rb} = 0$, $t_{\rm rb} = 1$), whereas for the decoherence reservoirs the wide-band approximation ($\eta = 1$) is used. 10^4 decoherence configurations have been used for the numerical average of the resistance (solid curves) as well as the transmission (dashed curves). The transmission plateaus are suppressed with increasing degree of decoherence p. Its average value is reduced, which indicates the additional resistance. As sketched in the inset, a decoherence configuration is generated by replacing randomly selected bonds (marked in purple) with decoherence reservoirs.
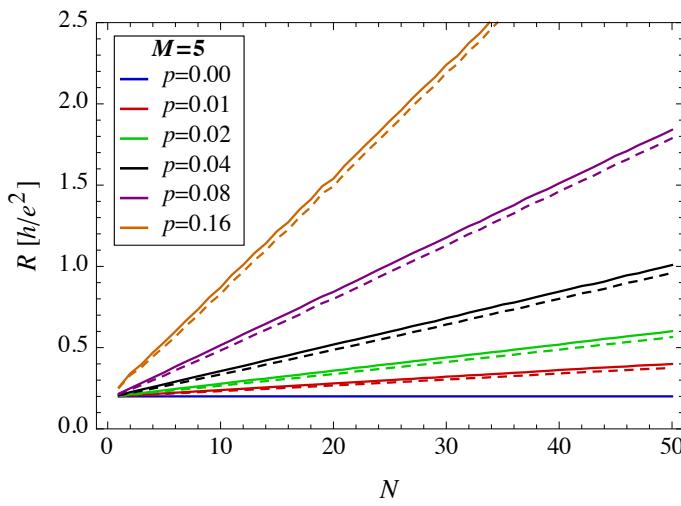
Figure 4.13: Resistance of a tight-binding ribbon ($M = 5$, $E = 0$) as a function of its length. The system goes from the ballistic to the Ohmic regime if a finite degree of decoherence $p > 0$ is introduced. The color coding and the parameters are the same as in Figure 4.12.
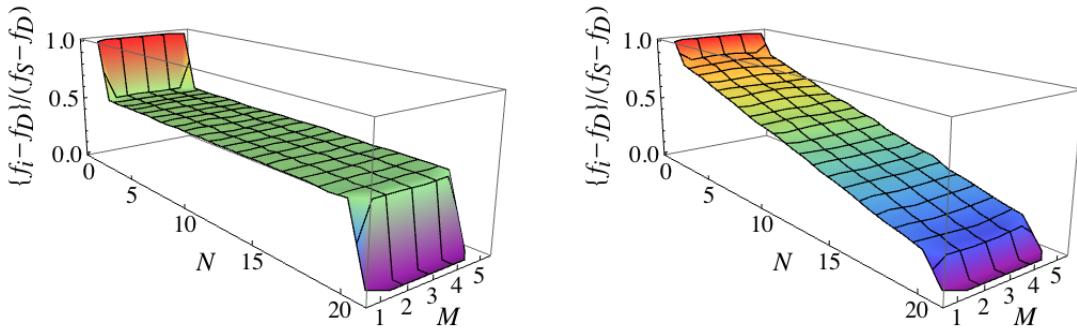
Figure 4.14: Quasi-Fermi level inside a ribbon of length $N = 20$ and width $M = 5$. In the coherent case ($p = 0$, left), the quasi-Fermi level drops entirely at the interface of the ribbon to the reservoirs. When decoherence is introduced ($p = 0.08$, right), the quasi-Fermi level decreases linearly as expected for an Ohmic conductor. The system parameters are the same as in Figure 4.12.

4.5 Effect of decoherence on Anderson localization

In the previous Sections, we found that decoherence causes in homogeneous systems a transition from the quantum-ballistic to the classical-Ohmic regime. Decoherence suppresses transport in these system, as the resistance is no longer constant but increases linearly with the chain length. This raises the fundamental, but up to now only partially answered question, if it is possible to *enhance* the transport in some systems by means of decoherence. In this respect, tight-binding chains [161, 170, 175, 202, 203, 206], molecular wires [32, 133, 134, 204] and aggregates [63, 99, 145, 151] have been studied. Recently, it has also been discussed, if Anderson localization, see Section 3.2.2, can be observed in presence of many-body interactions [17, 75, 136, 205]. As many-body interactions are a source of decoherence, this corresponds to the question, if localization is possible under the effect of decoherence. Addressing these questions, we study in this Section transport through disorder averaged tight-binding chains. In particular, we show that the spatial distribution of the decoherence has observable effects on the transport. We have published partially the results of this Section in [167, 168].

In order to keep the discussion clear and simple, we consider here only the band-center $E = 0$ and wide-band contacts with $\eta = 1$. However, we stress that the main results of this Section are still valid outside the band-center and for arbitrary reservoir self-energies. The resistivity of a tight-binding chain, ensemble averaged over uncorrelated decoherence $\{\cdot\}$ and disorder $\langle \cdot \rangle$ configurations, reads

$$\rho \equiv \frac{\{\langle R \rangle\}}{N} = \frac{1}{N} \sum_{j=1}^{N} u_j^N \left\langle \frac{1}{T_j} \right\rangle. \tag{4.10}$$

It can be evaluated by our previous results (3.21) and (4.6). We can directly see from the products $u_j^N \langle 1/T_j \rangle$ that the resistivity is determined by the relation of the characteristic lengths ξ and ℓ, see the Appendix A.4 for detailed derivations. When $\xi > \ell$ the transport

is Ohmic, i.e. the resistivity is length-independent

$$\rho_{\xi>\ell} \xrightarrow{N\to\infty} p + \frac{\sigma^2}{4}\frac{p}{p - \sigma^2\frac{1-p}{2-p}}. \tag{4.11}$$

However, when $\xi < \ell$ the system is localized, which means that its resistivity diverges exponentially with the chain length

$$\rho_{\xi<\ell} \propto e^{(1/\xi - 1/\ell)N}. \tag{4.12}$$

The root of the exponent $\xi^{-1} - \ell^{-1} = 0$ determines the critical degree of decoherence

$$p^* = 1 - e^{-1/\xi}, \tag{4.13}$$

where the transition between Ohmic and localized behavior appears. It can be related by (4.5) to a critical phase coherence length and is a function of the disorder strength σ, see (3.23). In a different way, (4.13) has been obtained already in [202]. Here, its derivation by the analytical formulae (3.21) and (4.6) allows to understand the statistical origin of the decoherence induced insulator-metal transition.

Localization is found to survive decoherence, when the exponentially increasing resistance of the long coherent subsystems (3.21) overcompensates their exponentially decreasing frequency of occurrence (4.6). Any decoherence distribution, for which the number u_j^N of coherent subsystems decreases with their length j faster than exponentially will show only Ohmic behavior. A simple example is to distribute the decoherence reservoirs randomly under the constraint that at least after $j_{\max}$ normal bonds a decoherence reservoir has to be introduced. The corresponding u_j^N has then a cut-off $u_{j>j_{\max}}^N = 0$ and thus, decreases faster than exponentially. In this case the system is Ohmic for any finite degree of decoherence. Also for a homogeneous decoherence distribution, where all subsystems have the same size ℓ_ϕ, the resistivity

$$\rho_{\text{hom}} = \frac{1}{\ell_\phi}\left\langle\frac{1}{T_{\ell_\phi}}\right\rangle \tag{4.14}$$

is Ohmic for any finite degree of decoherence. If however, u_j^N decreases with j asymptotically more slowly than exponentially, the system will always be localized, in spite of decoherence. This behavior appears for example, if the probability p_j of having coherent subsystems of length j (i.e. $j - 1$ succeeding normal bonds) decreases as $p_j \propto j^{-\gamma}$ with an arbitrary constant $\gamma > 0$.

This strong effect of the spatial distribution of decoherence on the transport is one of the main results of this thesis. It is summarized in Figure 4.15, where the resistivity of the infinitely long chain is shown as a function of the degree of decoherence. The dashed curves for homogeneous decoherence clearly show decoherence-assisted transport, and agree qualitatively well with other studies assuming homogeneous decoherence [32, 63, 99, 134, 145, 151, 161, 175, 206]. The solid curves for random uncorrelated decoherence exhibit divergencies at the critical degree of decoherence p^*, which is shown as a function of the disorder strength σ in Figure 4.16 (left). Thus, in contrast to homogeneous decoherence, where the transport is Ohmic for any $p > 0$, we find for random uncorrelated decoherence a metal-insulator transition at p^*. Moreover, Figure 4.15 shows that in both cases the resistivity of disordered chains can be reduced by decoherence or, in other words, transport

can be enhanced by decoherence. The optimal degree of decoherence p_{opt}, at which the resistivity is minimal, is shown in Figure 4.16 (right). It increases until a critical disorder strength ($\sigma^* = 1.4$ for random decoherence, $\sigma^* = 1.8$ for homogeneous decoherence), from which on completely incoherent transport $p = 1$ is optimal.
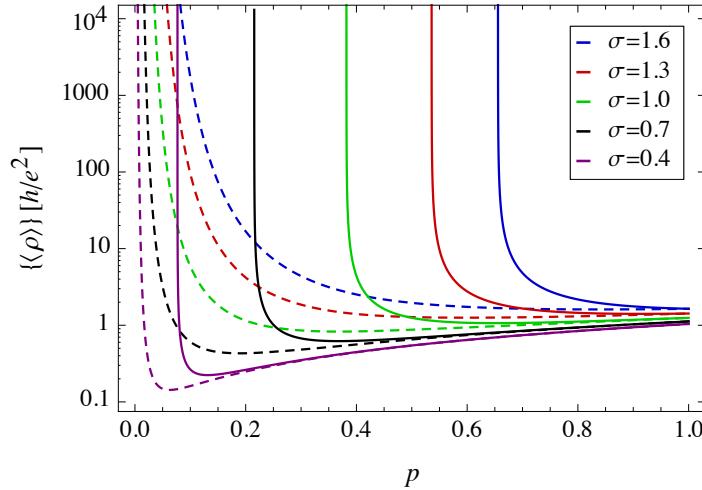
Figure 4.15: Resistivity ρ of an infinitely long disordered tight-binding chain as a function of the degree of decoherence p (inverse phase coherence length $1/\ell_\phi$). If the decoherence is distributed homogeneously (dashed curves), ρ is Ohmic for any $p > 0$. If the decoherence distribution is random and uncorrelated (solid curves), a minimal degree of decoherence p^* is necessary to obtain Ohmic conduction, whereas below this threshold the system is localized ($\rho \to \infty$).
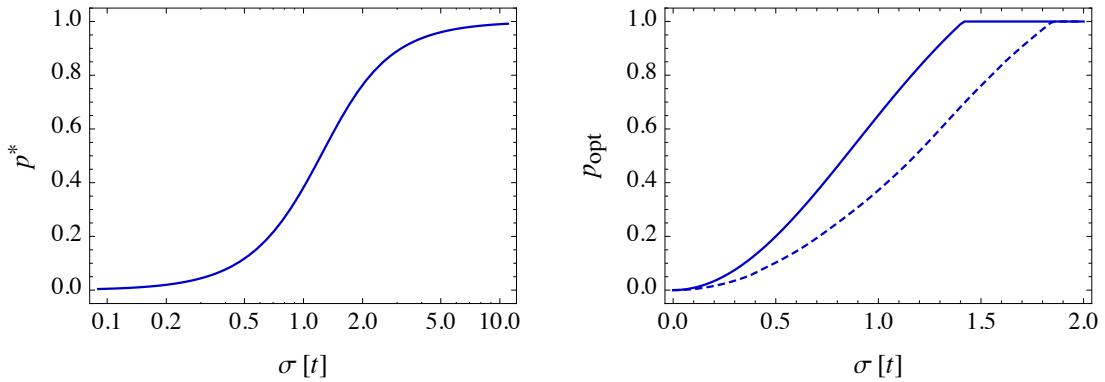
Figure 4.16: Critical degree of decoherence p^* (left) and optimal degree of decoherence p_{opt} (right) as a function of the disorder strength σ. At p^* an insulator-metal transition can be observed, if the decoherence is distributed randomly. At p_{opt} the transport is optimal, i.e. minimal resistivity for the random (solid curve) and the homogeneous decoherence distribution (dashed curve). The optimal degree of decoherence increases until a critical disorder strength, from which on completely incoherent transport $p = 1$ is optimal.

Taking many-body interactions explicitly into account, an insulator-metal transition is found at a critical temperature [17, 75], which is proportional to the degree of decoherence in the system. Experiments on various nanosystems have been performed, see e.g. [4, 69, 103, 157, 183], where a transition from Ohmic to exponential behavior is observed. It is found [69] that this transition occurs when the phase coherence length approaches the localization length[3], which agrees with our condition (4.13). However, to our knowledge these experiments have been done only for systems with a fixed length. In order to learn from an experiment how the decoherence is distributed, we propose to study the resistivity of linear nanosystems as a function of their length. When the decoherence is randomly distributed, we expect that below a critical temperature the resistivity increases exponentially with the chain length. Above the critical temperature the resistivity should be constant (Ohm's law). In contrast, for homogeneous decoherence we expect for any non-zero temperature Ohmic behavior, when the length of the system is increased.

In Section 3.2.1, we found that outside the conduction band the resistance of homogeneous chains, connected to wide-band reservoirs, increases exponentially with the length, see Figure 3.9. These chains show outside the conduction band also a decoherence induced insulator-metal transition, which is caused by the same mechanism. Thus, the critical degree of decoherence is generally a function of the disorder and the Fermi energy [202].

4.5.1 Partial phase randomization, tight-binding ribbons and the decoherence averaged transmission

In this Section, we show that our results are not model specific but appear more generally. We show that the insulator-metal transition also appears, (I) when the phase is randomized only partially at a virtual reservoir, (II) when tight-binding ribbons instead of chains are studied and, (III) when the conductance is ensemble averaged instead of the resistance.

In Figure 4.17, we show that the decoherence induced transition appears not only, if bonds are replaced by decoherence reservoirs (circles). It can also be observed, if the reservoirs are attached only to the chain (squares), which in general randomizes phase and momentum only partially at a decoherence reservoir. Contributions from the coherent transmission between next-nearest neighbors can be observed only for higher degrees of decoherence, because the transmission between two reservoirs is exponentially suppressed with their distance. The numerical averages over 10^9 decoherence and disorder configurations agree well with the analytical result (4.10) for completely phase and momentum randomizing reservoirs, see the solid curves. Combining this result with (4.14), we can conclude that attaching a homogeneous distribution of decoherence reservoirs to the chain leads to Ohmic transport for any finite degree of decoherence.

The decoherence induced transition from localized to Ohmic behavior is not restricted to 1D chains but is also found in quasi-1D ribbons, see Figure 4.18. Note that for these ribbons the critical degree of decoherence is less compared to chains. This can be understood, by recalling that localization under the effect of decoherence is caused by the long coherent subsystems. In a ribbon of length N and width M, the number of bonds is $N(2M-1)-M$ and thus, the probability of having a long section in the ribbon, which does not contain any decoherence reservoir, decreases by a factor $1/(2M-1)$ compared to chains.

---

[3]Note that our parameter ξ^{-1} is the second-order generalized Lyapunov exponent and not the localization length λ, see Section 3.2.2. However, both quantities are a measure for the localization in the system.
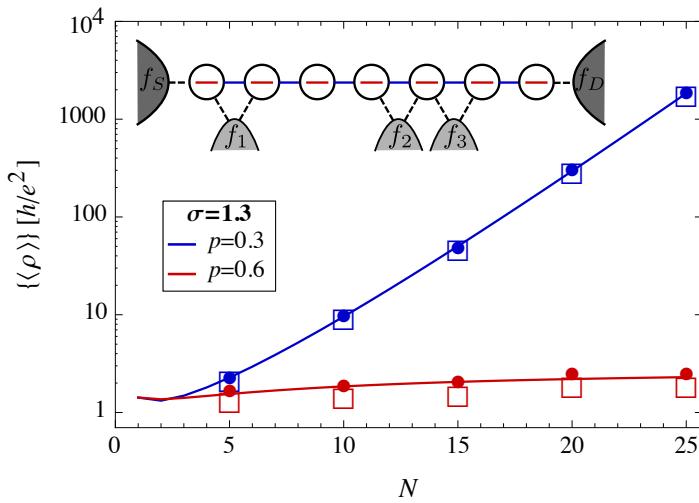
Figure 4.17: Resistivity of the disordered chain as a function of its length. The decoherence induced transition also appears, when the randomly distributed decoherence reservoirs are only attached to the chain ($\square$). Averages were calculated numerically over 10^9 decoherence and disorder configurations. Also shown is the average over the same ensemble under the assumption of complete phase randomization ($\bullet$), as well as the corresponding analytical result (4.10) (solid curves).
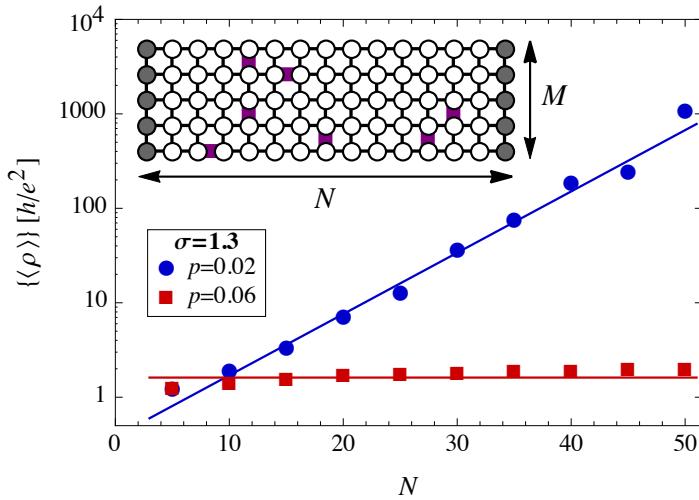
Figure 4.18: Resistivity of a tight-binding ribbon of width $M = 5$ and variable length N. The decoherence induced transition can also be observed in this quasi-1D system. The solid lines are fits with an exponential function and a constant, respectively. Numerical averages were taken over $25N \cdot 10^5$ decoherence and disorder configurations.

Finally we study, if the transition also occurs, when the decoherence average is not performed over the resistance $\{\langle R \rangle\}$ but over the conductance $\{1/\langle R \rangle\}$. In this case, analytical calculations are demanding but the numerical average over random uncorrelated decoherence configurations clearly confirms that a minimal degree of decoherence is necessary for Ohmic transport, see Figure 4.19. Below this threshold a power-law divergence is found in contrast to the exponential increase (4.12) in the case of averaging the resistance. Figure 4.19 also shows that deep in the Ohmic regime, the resistivity is independent of the averaging process, see the convergence of the solid curve for $p = 0.60$ to the dashed horizontal line, which gives the analytically known limit value (4.11) in the case of averaging the resistance. However, from the numerical data it is not clear, whether this is also true in the transitional regime and whether the critical degree of decoherence depends on the averaging process, see the curve for $p = 0.55$, which should converge to the corresponding dashed horizontal line representing (4.11), whereas the curve for $p = 0.50$ should diverge. Anyway, for our purpose it is more important that the discussed metal-insulator transition appears independently of the averaging process.
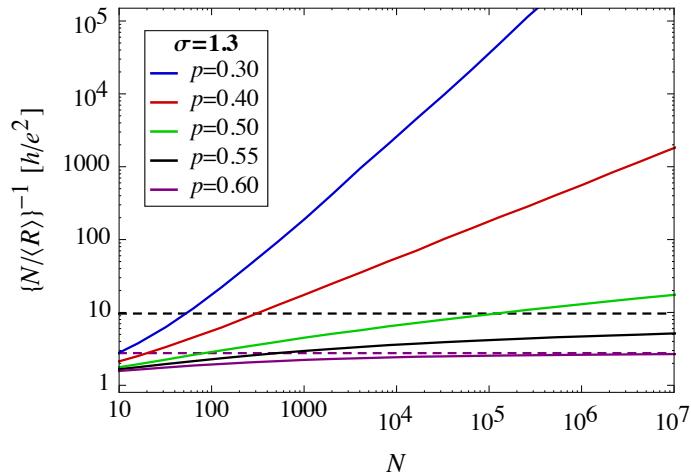
Figure 4.19: Resistivity of a tight-binding chain as a function of its length after averaging numerically the conductance over 10^4 random uncorrelated decoherence configurations. A minimal degree of decoherence is necessary for Ohmic conduction, whereas below a power-law divergence is found. Deep in the Ohmic regime, the resistivity is independent of the averaging process, see the convergence of the solid curve for $p = 0.60$ to the dashed curve, which gives the resistivity due to (4.11). However, the influence of the averaging process in the transitional regime is not clear, see the curve for $p = 0.55$, which should converge to the corresponding dashed horizontal line, and the curve for $p = 0.50$, which should diverge.

4.6 Pure dephasing: Phase randomization but momentum conservation

In our statistical decoherence model, like in many models using Büttiker probes, phase *and* momentum of the conduction electrons are randomized at the decoherence reservoirs. This assumption is reasonable in many situations, such as the interaction with a phonon bath or with localized scatterers, which exhibit additional degrees of freedom (e.g. magnetic impurities). However, in some situations only the phase is randomized but the momentum is conserved [42, p.129ff]. This *pure dephasing* can arise from electron-electron interaction, see [72] and [44, Chapter 19.4]. Also the interaction with longitudinal phonons is considered as a source of pure dephasing [104]. In this Section, we will show how our statistical decoherence model can be extended in order to allow to tune the degree of phase and momentum randomization independently. Only few decoherence models also provide this flexibility [72, 104, 113, 195, 199]. We have published partially the results of this Section in [170].

In one-dimensional systems, pure dephasing can be obtained, if we define two energy distribution functions per decoherence reservoir, see Figure 4.20. The $f_i^{\rightarrow}$ and $f_i^{\leftarrow}$ allow to distinguish between the forward moving and backward moving electrons or, in other words, to attribute to every electron a definite sign of the momentum. The absence of energy relaxation then ensures momentum conservation at the decoherence reservoirs.
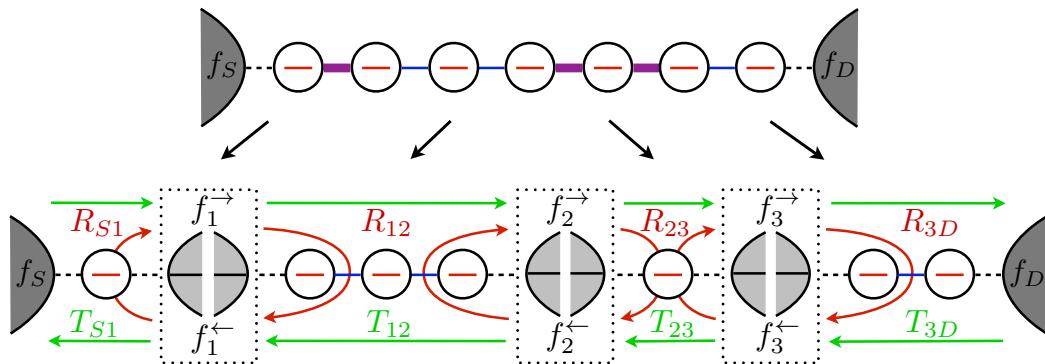
Figure 4.20: Pure dephasing, i.e. phase randomization but momentum conservation, can be obtained in 1D chains, if two energy distribution functions are assigned to each decoherence reservoir. This allows to distinguish between the forward moving $f_i^{\rightarrow}$ and backward moving $f_i^{\leftarrow}$ electrons. The absence of energy relaxation then ensures momentum conservation at the decoherence reservoirs. The transmission $T_{i+1,i}$ between neighboring reservoirs is indicated by green arrows and the reflection $R_{i+1,i} = 1 - T_{i+1,i}$ by red arrows.

Taking into account that the energy resolved current is conserved at the N_d decoherence reservoirs, the energy distribution functions are determined by $2N_d$ linear equations

$$T_{i,i-1}f_{i-1}^{\rightarrow} - T_{i+1,i}f_i^{\rightarrow} - R_{i+1,i}f_i^{\rightarrow} + R_{i-1,i}f_i^{\leftarrow} \overset{!}{=} 0, \tag{4.15a}$$

$$T_{i,i+1}f_{i+1}^{\leftarrow} - T_{i-1,i}f_i^{\leftarrow} - R_{i-1,i}f_i^{\leftarrow} + R_{i+1,i}f_i^{\rightarrow} \overset{!}{=} 0, \tag{4.15b}$$

where $R_{i+1,i} = 1 - T_{i+1,i}$ is the reflection. Solving this system of $2N_d$ linear equations, the energy distribution functions of the decoherence reservoirs read

$$f_i^{\rightarrow} - f_D = \frac{\sum_{k=i}^{N_d} \frac{1}{T_{k+1,k}} - N_d + i}{\sum_{k=0}^{N_d} \frac{1}{T_{k+1,k}} - N_d} (f_S - f_D), \tag{4.16a}$$

$$f_i^{\leftarrow} - f_D = \frac{\sum_{k=i}^{N_d} \frac{1}{T_{k+1,k}} - N_d + i - 1}{\sum_{k=0}^{N_d} \frac{1}{T_{k+1,k}} - N_d} (f_S - f_D). \tag{4.16b}$$

By means of the Landauer equation, we obtain for the zero-bias resistance

$$R = \sum_{i=0}^{N_d} \frac{1}{T_{i+1,i}} - N_d. \tag{4.17}$$

Thus, comparing (4.1) with (4.17), for pure dephasing the sum of the subsystem resistances is reduced by the constant contact resistance $R_0 = 1$ of each of the momentum conserving decoherence reservoirs.

In general, from the N_d decoherence reservoirs in a system, N_d^c reservoirs are momentum conserving and $N_d - N_d^c$ reservoirs are momentum randomizing. If we set $f_i^{\rightarrow} = f_i^{\leftarrow} = f_i$ for the momentum randomizing reservoirs, we can still use (4.15) to calculate the energy distribution functions of the momentum conserving reservoirs. For the energy distribution functions of the momentum randomizing reservoirs, we have to use the modified rate equation $T_{i,i-1}(f_{i-1}^{\rightarrow} - f_i) - T_{i+1,i}(f_i - f_{i+1}^{\leftarrow}) = 0$, which is nothing but the sum of the two equations in (4.15). Solving this system of linear equations, the zero-bias resistance $R = \sum_{i=0}^{N_d} \frac{1}{T_{i+1,i}} - N_d^c$ is reduced only by N_d^c.

Focusing on random uncorrelated distributions of the decoherence reservoirs, the bonds of a tight-binding chain are selected with probability p as a decoherence bond. These decoherence bonds are with probability p_r momentum randomizing and with probability $1 - p_r$ momentum conserving, see Figure 4.21. However, we allow also other spatial decoherence distributions, under the constraint that in a chain of length N in average $(N-1)p$ decoherence reservoirs are introduced from which $(N-1)p(1-p_r)$ are momentum conserving and $(N-1)pp_r$ are momentum randomizing.
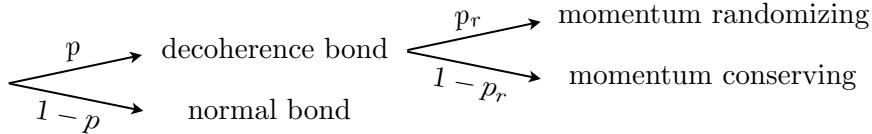
Figure 4.21: Decision tree for generating random uncorrelated decoherence configurations.

The average distance of momentum randomizing decoherence reservoirs

$$\ell_m^{\phi} = \frac{N}{1 + (N-1)pp_r} \xrightarrow{N \to \infty} \frac{1}{pp_r} \tag{4.18}$$

gives in homogeneous systems the mean free path ℓ_m. In disordered systems the spatial rates of all momentum randomization processes have to be summed up. In the Anderson

model, for example, we have to take into account the contributions from phase conserving scattering ξ (3.23) as well as from phase randomizing scattering ℓ_m^ϕ, to obtain for the mean free path

$$\frac{1}{\ell_m} = \frac{1}{\xi} + \frac{1}{\ell_m^\phi}. \tag{4.19}$$

The decoherence averaged resistance is given by

$$\{R\} = \left\{\sum_{i=0}^{N_d} \frac{1}{T_{i+1,i}}\right\} - (N-1)p(1-p_r). \tag{4.20}$$

As the first term is independent from the fact whether the decoherence is momentum randomizing or conserving, the decoherence averaged resistance can be tuned easily by the second term between the two regimes. The additional resistance due to momentum randomizing decoherence

$$\{\Delta R\} \equiv \{R(p_r)\} - \{R(p_r = 0)\} = (N-1)pp_r \tag{4.21}$$

increases linearly with the chain length and both decoherence probabilities.

4.6.1 Homogeneous chains: Ballistic conduction survives pure dephasing

We have learned in Section 3.2.1 that homogeneous chains show perfect transmission $T = 1$ inside the conduction band, if semi-infinite chains ($\varepsilon_{\text{ch}} = 0$, $t_{\text{ch}} = 1$) are used as the reservoirs. This can also be observed in the center of the conduction band, if wide band reservoirs ($\eta = 1$) are used. In these cases, the decoherence averaged resistance is given by

$$\{R\} = \{N_d + 1\} - (N-1)p(1-p_r) = 1 + (N-1)pp_r, \tag{4.22}$$

which agrees with (4.9) in the limit $p_r = 1$. However, in the case of pure dephasing $p_r = 0$, ballistic conduction $\{R\} = 1$ is retained for any degree of decoherence p, because phase randomization of the conduction electrons does not alter the fact that these electrons can propagate through the homogeneous chain without suffering backscattering. Ohmic behavior $\{R\} \propto N$ is found only, if momentum randomization takes place at some decoherence reservoirs $p_r > 0$.

When the reservoirs do not match perfectly the chain, resistance oscillations can be observed, see Figure 3.8. Under the effect of pure dephasing $p_r = 0$, interference effects like these resistance oscillations are suppressed but the transport is still ballistic, see Figure 4.22. The transport is Ohmic, if momentum randomization is introduced $p_r > 0$, as also shown in Figure 4.4 for the case $p_r = 1$. Note that for the decoherence reservoirs, semi-infinite chains with $\varepsilon_{\text{ch}} = 0$, $t_{\text{ch}} = 1$ have to be used, in order to avoid an additional contact resistance due to mismatching reservoirs.

Figure 4.23 shows the quasi-Fermi level along a 20 sites long homogeneous chain, which is given by the decoherence averaged energy distribution function $\{f_i\} = \{f_i^\rightarrow + f_i^\leftarrow\}/2$. The dashed and the dotted curves give the quasi-Fermi level of the forward moving $\{f_i^\rightarrow\}$ and backward moving $\{f_i^\leftarrow\}$ electrons, respectively. Under the effect of pure dephasing, the quasi-Fermi level is the same as for coherent transport, compare with Figure 4.5. The

forward moving electrons remain at the Fermi level of the source and the backward moving electrons at the Fermi level of the drain, as expected for ballistic transport [42, Section 2.1]. If momentum randomization is introduced, the quasi-Fermi level drops linearly, which indicates Ohmic transport. The same behavior of the quasi-Fermi level under the effect of pure dephasing is reported in [72].
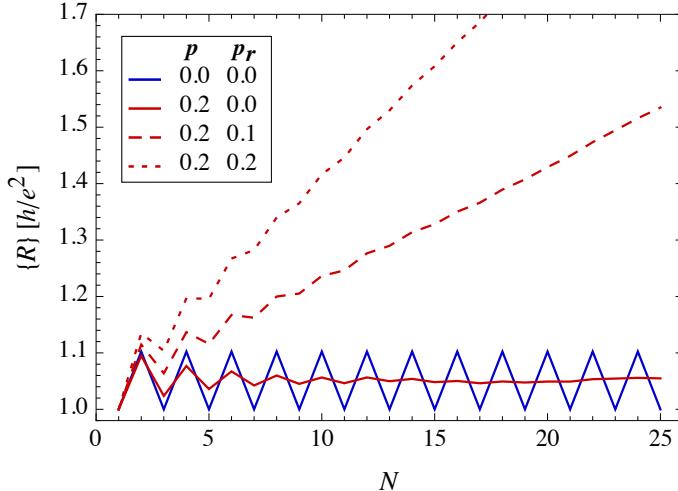
Figure 4.22: Resistance of a homogeneous chain as a function of its length ($E = 0$). For the real source and drain reservoirs the wide-band approximation with $\eta = 0.73$ is used, whereas for the virtual decoherence reservoirs semi-infinite chains with $\varepsilon_{\mathrm{ch}} = 0$, $t_{\mathrm{ch}} = 1$ have to be used in order to avoid an additional contact resistance. Pure dephasing $p_r = 0$ suppresses interference effects like the resistance oscillations but ballistic conduction is retained. If momentum randomization takes place at some decoherence reservoirs $p_r > 0$, Ohmic behavior can be observed. Averages are over $N \cdot 10^4$ decoherence configurations.

4.6.2 Disordered chains: Smoothing of transmission resonances but conservation of its average

Figure 4.24 shows the effect of pure dephasing on the energy resolved transmission of a disordered chain, studied also in Figures 3.10, 4.8, and 4.9. The coherent transmission shows several resonances due to interference between the disordered sites. When decoherence is introduced, the interference is suppressed and these oscillations vanish. For pure dephasing (solid curves), only the oscillations in the transmission are smoothed out, whereas its average is conserved. For momentum randomizing decoherence (dashed curves), the transmission itself is reduced indicating additional resistance, as also shown in Figure 4.8. This behavior of the transmission function agrees with the results reported in [16, 72, 195, 199]. Note that the curves in Figure 4.8 and Figure 4.24 differ slightly, because for the former wide-band decoherence reservoirs are used, but for the latter semi-infinite chains ($\varepsilon_{\mathrm{ch}} = 0$, $t_{\mathrm{ch}} = 1$).
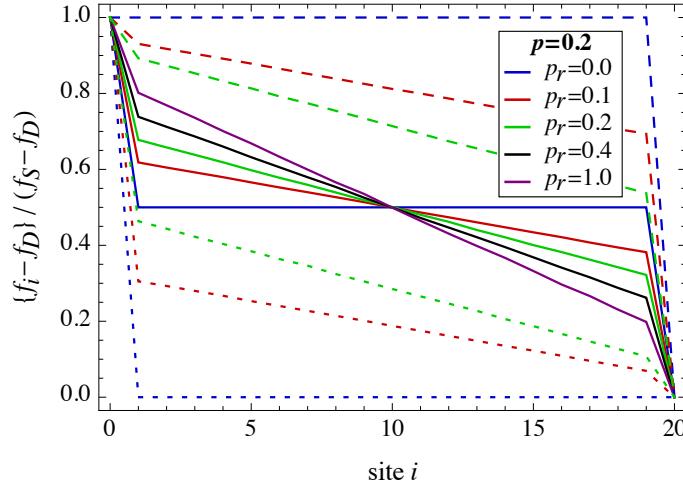
Figure 4.23: Decoherence averaged energy distribution function $\{f_i\} = \{f_i^{\rightarrow} + f_i^{\leftarrow}\}/2$ (or quasi-Fermi level) along a 20 sites long homogeneous chain (solid curves). The dashed and the dotted curves give the quasi-Fermi level of the forward moving $\{f_i^{\rightarrow}\}$ and backward moving $\{f_i^{\leftarrow}\}$ electrons, respectively. Under the effect of pure dephasing $p_r = 0$, the quasi-Fermi level is the same as for coherent transport, compare with Figure 4.5. The forward moving electrons remain at the Fermi level of the source and the backward moving electrons at the Fermi level of the drain, as expected for ballistic conduction. If momentum randomization is introduced $p_r > 0$, the quasi-Fermi level drops linearly, which indicates Ohmic transport. 10^5 decoherence configurations are used.
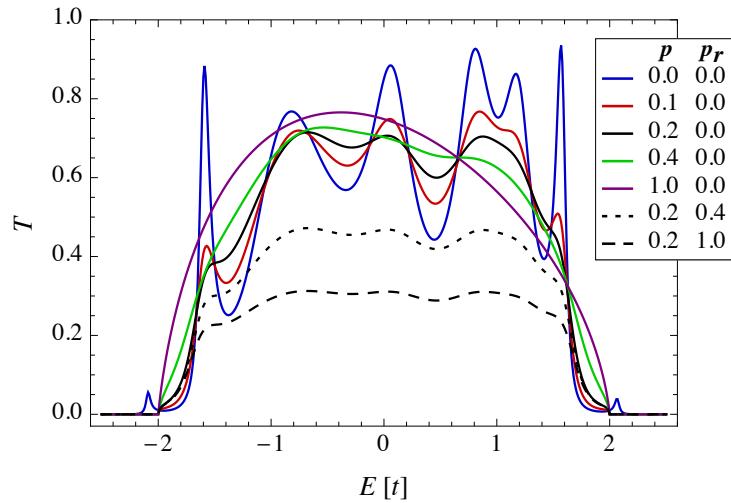
Figure 4.24: Effect of pure dephasing on the energy resolved transmission of the 10 sites long disordered chain, studied also in Figures 3.10, 4.8, and 4.9. For pure dephasing, only the transmission resonances are smoothed due to the suppression of interference. For momentum randomizing decoherence, also the average value of the transmission decreases, which indicates the additional resistance. Averages are over 10^4 decoherence configurations.

4.6.3 Anderson model: Pure dephasing enhances always transport

We discuss in this Section, if the decoherence induced insulator-metal transition in the Anderson model reported in Section 4.5, is changed in the case of pure dephasing. From (4.20) we know that the degree of momentum randomization changes the decoherence averaged resistance only by a linear term. As this linear term does not alter the fact that the resistance is exponentially increasing in the localized regime, the critical degree of decoherence, at which the transition to the Ohmic regime appears, is independent of the degree of momentum randomization. However, the Ohmic resistivity (4.11) can be reduced by pure dephasing

$$\rho_{\xi>\ell} \xrightarrow{N\to\infty} pp_r + \frac{\sigma^2}{4}\frac{p}{p - \sigma^2\frac{1-p}{2-p}}. \tag{4.23}$$

Figure 4.25 shows that the transport is optimal in the complete incoherent case, if only the phase is randomized at the decoherence reservoirs. The transport is enhanced by pure dephasing, because the momentum conserving decoherence reservoirs reduce the length of the localized subsystems but do not introduce any additional resistance.
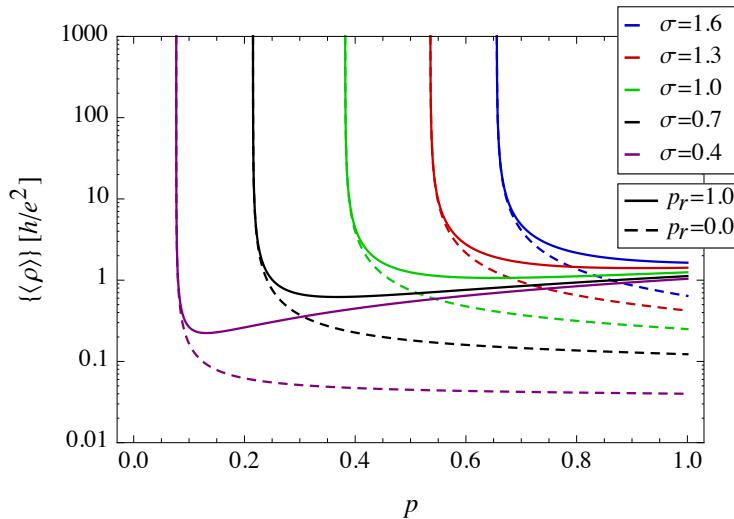
Figure 4.25: Resistivity of the infinitely long disordered chain as a function of the degree of decoherence. The critical degree of decoherence p^*, which separates the localized-exponential from the Ohmic-linear regime, is independent of p_r. However, pure dephasing $p_r = 0$ always reduces the Ohmic resistivity of the chain, because momentum conserving decoherence reservoirs reduce the length of the localized subsystems but do not introduce any additional resistance. Thus, the transport is optimal in the complete incoherent case.

4.6.4 Outlook: Spin randomizing and spin conserving decoherence

In the preceding Sections, we have learned that pure dephasing can be obtained by defining two energy distribution functions per decoherence reservoir. Obviously, this approach can be used only in 1D chains, in which the momentum of the electrons has only two possible directions. It cannot be applied in tight-binding ribbons and grids, where the momentum is a 2D vector. However, it can be used to study in every tight-binding lattice the effect of decoherence on the transport of spin polarized electrons. By means of two energy distribution functions per decoherence reservoir, we can distinguish between the spin-up and spin-down electrons. This allows to tune the degree of phase and spin randomization independently.

Spintronics, which aims at utilizing the electron spin for novel electronic devices, has gained recently further stimulation by the observation of novel *topological insulators*, see [81, 116, 160] and references therein. The quantum Hall effect [180], awarded with the Nobel prize in 1985, as well as the recently observed quantum spin Hall effect [106, 155] are topological insulating. In both cases, the current is carried in *edge channels* straight along the surface of the system, while the interior is insulating. In the quantum Hall effect, all electrons in an edge channel propagate in the same direction, whereas in the quantum spin Hall effect the edge channels are *helical*, which means that the spin-up and the spin-down electrons propagate in opposite directions. It is also discussed, if a topological insulator can be realized in graphene under the effect of heavy metal doping [98, 188]. In order to study the robustness of these novel topological insulators against the effects of spin randomizing and spin conserving decoherence, our statistical model can be helpful. First work in this direction can be found in [92, 194]. Although this closing Section is intended only as an outlook, let us discuss a simple test system.

When spin polarization is taken into account, basically all matrices become twice as large. The Hamiltonian can be partitioned into four blocks

$$H = \begin{pmatrix} H_\uparrow & t_{\uparrow\downarrow} \\ t_{\downarrow\uparrow} & H_\downarrow \end{pmatrix}, \tag{4.24}$$

where $H_\uparrow$ and $H_\downarrow$ are the Hamiltonians for isolated spin-up and spin-down systems, respectively. The coupling between the spin-up and spin-down systems is described by $t_{\uparrow\downarrow} = t_{\downarrow\uparrow}^+$. We consider a tight-binding ribbon of length $N = 15$ and width $M = 7$, as sketched in Figure 4.26. The Hamiltonian of the ribbon reads

$$
\begin{aligned}
H = &\sum_{i=1}^{N} \sum_{j=1}^{M} \begin{pmatrix} \varepsilon_{ij} + \varepsilon_z & 0 \\ 0 & \varepsilon_{ij} - \varepsilon_z \end{pmatrix} |i,j\rangle \langle i,j| \\
&+ \begin{pmatrix} t & 0 \\ 0 & t \end{pmatrix} \left[\sum_{i=1}^{N-1} \sum_{j=1}^{M} \big(|i,j\rangle \langle i+1,j| + \text{H.c.}\big) + \sum_{i=1}^{N} \sum_{j=1}^{M-1} \big(|i,j\rangle \langle i,j+1| + \text{H.c.}\big) \right].
\end{aligned}
\tag{4.25}
$$

The Zeeman spin splitting ε_z, which we have taken into account to give an example for broken spin degeneracy, as well as the inter-site couplings t are functions of the magnetic field. For simplicity, we assume the absence of a magnetic field, which implies $\varepsilon_z = 0$ and $t = 1$. In topological insulators, spin-orbit interaction is also essential, which leads to non-zero coupling matrices $t_{\uparrow\downarrow}$, see e.g. [44, Chapter 22].

A current of spin-up electrons $I_\uparrow$ is applied between the source and drain contacts, see the blue sites in Figure 4.26, which means that the self-energies due to these contacts act only on $H_\uparrow$. Additional voltage probes measure the energy distribution functions $f_\uparrow$ of spin-up electrons (light blue sites) and $f_\downarrow$ of spin-down electrons (light red sites). Figure 4.27 shows that under the effect of decoherence $p > 0$ the potential of the spin-up probes (dashed curves) increases approximately from $1/2$ to $3/4$. This indicates the transition from the ballistic to the Ohmic regime, which is independent of the degree of spin randomization p_r. This transition can also be seen in Figure 4.5 at the 5th site. If the decoherence is spin conserving $p_r = 0$, the potential at the spin-down probes (solid curves) is exactly zero, because no spin-down electrons exist in the system. If spin randomization takes place $p_r > 0$, the potential tends approximately to $1/4$ for $p \to 1$. This indicates again the transition from ballistic to Ohmic conduction and can also be seen in Figure 4.5 at the 15th site. However, for $0 < p \ll 1$ the potential tends to $1/2$, which shows that ballistic transport can sustain a weak degree of decoherence, while the spins are randomized efficiently.

Note that our results do not depend on which of the two spin-up probes and two spin-down probes we use. However, this will change in presence of a magnetic field. In the following Chapter 5, we will use such a multi-terminal geometry to study magnetotransport in 2D electron systems.
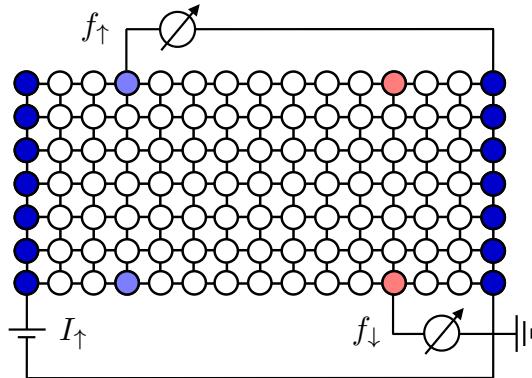
Figure 4.26: Transport of spin polarized electrons through a tight-binding ribbon of length $N = 15$ and width $M = 7$ is studied. A spin-up current $I_\uparrow$ is applied between the source and drain reservoirs (attached to the blue sites). Additional voltage probes measure the energy distribution function $f_\uparrow$ of spin-up electrons (light blue sites) and $f_\downarrow$ of spin-down electrons (light red sites). For clarity, the wiring is drawn only for two probes but calculations are performed at all of them.
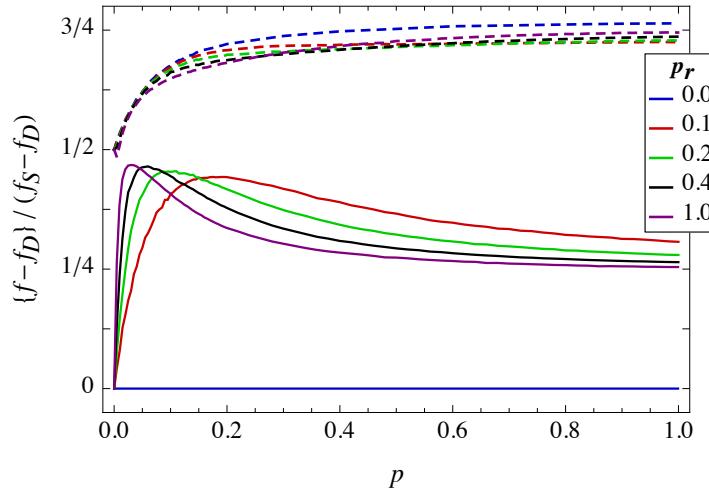
Figure 4.27: Normalized potential of the spin-up probes (dashed curves) and the spin-down probes (solid curves) as a function of the degree of decoherence p. When p is increased, the potential of the spin-up probes increases approximately from $1/2$ to $3/4$, which indicates the transition from ballistic to Ohmic conduction, compare with Figure 4.5. If the decoherence is spin conserving $p_r = 0$, the potential at the spin-down probes vanishes exactly. If spin randomization takes place $p_r > 0$, the potential tends to $1/4$ for $p \to 1$, which again indicates the ballistic-to-Ohmic transition. However, for $0 < p \ll 1$ the potential tends to $1/2$, which shows that ballistic transport can sustain a weak degree of decoherence, while the spins are randomized efficiently.

4.7 Conclusions

In this Chapter, we have studied the effects of decoherence on the transport in tight-binding lattices by means of a novel statistical model, which can be summarized briefly as follows:

- Decoherence regions are distributed spatially over the quantum system according to a given probability distribution function.

- The electron phase is randomized completely at these regions, which are modeled by Büttiker probes and characterized by energy distribution functions. The transport in between the decoherence regions is assumed as phase coherent.

- Afterwards, the transport quantity of interest is ensemble averaged over spatial decoherence configurations.

This model, proposed originally by M. Zilly et al. [201–203], has been generalized and extended in some aspects. It can be applied now to arbitrary tight-binding lattices using the multi-terminal formula (2.40). In the case of 1D chains, the multi-terminal formula reduces to the simple result that the resistance of a decoherence configuration is given by the sum of the quantum coherent subsystem resistances (4.1). However, a subdivision into smaller coherent subsystems is possible only in 1D chains. In arbitrary tight-binding lattices, generally the coherent transmission between every pair of reservoirs has to be calculated.

How such lattices can be subdivided into smaller coherent subsystems remains as an open question to be addressed in the future. Nevertheless, as in our model decoherence regions are introduced in average only at a fraction of all possible places, it is computationally still more efficient than approaches, which model the decoherence as continuously present in the system. The ensemble average can be parallelized easily by distributing to each processor a decoherence configuration.

We have discussed how homogeneous tight-binding lattices are driven by decoherence from the quantum-ballistic to the classical-Ohmic regime, see Figures 4.3 and 4.13. For 1D chains this transition has been proven analytically (4.9). We have also shown in Figures 4.5 and 4.14 that the quasi-Fermi level of a ballistic conductor drops entirely at the interfaces to the reservoirs, whereas under the effect of decoherence the linearly decreasing quasi-Fermi level of an Ohmic conductor is found. We have discussed some model variations and compared our model with other approaches, but found in all cases qualitatively the same behavior, see Figures 4.9 and 4.11.

We have also studied the effect of decoherence on Anderson localization by means of our model, generalized to arbitrary decoherence configurations. We have shown that the transport through disordered quantum systems is affected significantly by the spatial distribution of decoherence [167, 168]. When the decoherence is homogeneously distributed, Ohmic conduction is found for any finite degree of decoherence. In contrast, for random uncorrelated decoherence, a minimal degree of decoherence is necessary, whereas below the system is localized, see Figure 4.15. This insulator-metal transition is caused by the interplay of the exponentially increasing coherent resistance (3.21) and its exponentially decreasing importance (4.6). The characteristics of our model, in particular the assumption of completely phase randomizing reservoirs, are not important for this transition, but make our model simple and allow to gain insight into the transport problem by analytical calculations. To summarize in other words, we found that an Anderson insulator can be stable against decoherence effects, if these are randomly distributed. We have also seen that transport through disordered tight-binding chains can be enhanced by decoherence up to a critical disorder strength, from which the completely incoherent transport is optimal, see Figure 4.16 (right).

Studying in Figures 4.8 and 4.12 the energy resolved transmission, we found that the resonances, caused by interference of the coherent electrons, are suppressed when decoherence is introduced. However, also the average value of the transmission drops indicating the additional resistance due to momentum randomization at the decoherence regions. We have extended our decoherence model to obtain pure dephasing in 1D chains [170]. We have shown that in this case the resistance of the system is reduced by the contact resistance of the virtual decoherence reservoirs (4.17). Under the effect of pure dephasing, resonances in the transmission are suppressed but its average remains constant, see Figure 4.24. Ballistic conduction in homogeneous chains survives pure dephasing, because of the absence of backscattering during the phase randomization process, see Figure 4.22. In the same way, the quasi-Fermi level drops entirely at the interfaces, because the electrons remain at the Fermi energy of the reservoir they are originating from, see Figure 4.23. In disordered quantum systems pure dephasing always enhances transport, because the length of the localized subsystems is reduced by the decoherence regions without introducing additional contact resistance, see Figure 4.25. Our model for pure dephasing can be applied only to 1D systems. However, we have concluded this Chapter with an outlook on how to use this model to study the transport of spin-polarized electrons in arbitrary tight-binding lattices under the effect of spin conserving and spin randomizing decoherence.

5 Magnetotransport in 2D electron systems

In this Chapter, we study magnetotransport in two-dimensional electron systems. We start with a nonrelativistic two-dimensional electron gas (2DEG), as it can be realized experimentally in semiconductor heterostructures, and discuss in Section 5.1 its basic properties. In order to apply the nonequilibrium Green's function method, we also show how such a 2DEG can be approximated by finite differences. In Section 5.2, we study magnetotransport along the boundary of a finite 2DEG. In particular, we discuss how the system properties change, when the magnetic field strength is increased. In weak fields, the coherent electron flow can be described by classical cyclotron orbits. In strong magnetic fields, the quantum Hall effect can be observed, which is also introduced briefly. In intermediate fields, we find anomalous resistance oscillations, which are explained by means of a minimal model. We have published the results of this Section in [169]. Our studies are also applied to graphene's relativistic 2DEG. After a short introduction to graphene in Section 5.3, we study magnetotransport along the boundaries of graphene nanoribbons in Section 5.4. The effects found in a nonrelativistic 2DEG can also be observed in graphene. We show that the local magnetotransport is affected by the shape of the edges of the ribbons. The Chapter is concluded with some notes on Hofstadter's butterfly shown on the cover page of this thesis.

5.1 The nonrelativistic 2D electron gas

5.1.1 Hamiltonian and its finite differences approximation

The nonrelativistic two-dimensional electron gas (2DEG) is described by the Hamiltonian

$$H_{\text{2DEG}} = \frac{\boldsymbol{p}^2}{2m}, \tag{5.1}$$

where $\boldsymbol{p}$ is the momentum operator and m the (effective) electron mass. The Schrödinger equation can be solved easily by a plane-wave ansatz $\psi_{\boldsymbol{k}}(\boldsymbol{r}) = \mathrm{e}^{\mathrm{i}\boldsymbol{k}\cdot\boldsymbol{r}}$, which leads to a parabolic dispersion relation

$$\epsilon(\boldsymbol{k}) = \frac{\hbar^2 \boldsymbol{k}^2}{2m}. \tag{5.2}$$

The DOS per unit area can be calculated directly from its definition

$$D(E) = \frac{1}{S}\sum_{\boldsymbol{k}} \delta\left(E - \epsilon(\boldsymbol{k})\right) = \int \frac{\mathrm{d}^2 k}{4\pi^2}\, \delta\left(E - \frac{\hbar^2 \boldsymbol{k}^2}{2m}\right) = \frac{m}{2\pi\hbar^2}\theta(E), \tag{5.3}$$

where S is the system size.[1] It is constant above the band edge at $E = 0$.

To study transport through a 2DEG, we evaluate numerically the Green's function (2.20) and the transmission function (2.33). To do so, the derivatives in the Hamiltonian are approximated by finite differences (in first order)

$$H_{2\text{DEG}}^{\text{FDA}} = 4t\psi_{x,y} - t\left(\psi_{x+1,y} + \psi_{x-1,y} + \psi_{x,y+1} + \psi_{x,y-1}\right), \qquad (5.4)$$

with the coupling

$$t \equiv \frac{\hbar^2}{2ma^2}. \qquad (5.5)$$

$\psi_{x,y}$ denotes the wave function at discrete supporting points on a square lattice with spacing a, see Figure 5.1. In the finite differences approximation, the Hamiltonian of the 2DEG is equivalent to the Hamiltonian of a tight-binding ribbon (3.5), apart from the fact that the energy is shifted by $4t$ and the coupling has negative sign. The parabolic dispersion of the 2DEG is approximated by a cosine band (compare with (3.9))

$$\epsilon(k,q) = 4t - 2t\left(\cos(ka) + \cos(qa)\right). \qquad (5.6)$$

This approximation is justified only if k, $q \ll 1$, which corresponds to energies close to the band edge. In the same way, the DOS (3.10) is approximately constant only close to the band edge, see Figures 3.2 (right). We conclude that the finite differences approximation can be applied, if the discretization a is chosen so small that the Fermi energy (measured in multiples of $t \propto 1/a^2$) is close to the band edge.[2]

5.1.2 Effect of a magnetic field

Under the effect of a homogeneous magnetic field $\boldsymbol{B} = -Be_z$ perpendicular to the 2DEG, see Figure 5.1, the Hamiltonian reads

$$H_{2\text{DEG}} = \frac{(\boldsymbol{p} - e\boldsymbol{A})^2}{2m}, \qquad (5.8)$$

where $\boldsymbol{A} = Bye_x$ is the vector potential of the magnetic field. Using the ansatz $\psi_k(\boldsymbol{r}) = \mathrm{e}^{ikx}\chi(y)$, we obtain for $\chi(y)$ the Schrödinger equation of a shifted harmonic oscillator

$$\epsilon\,\chi(y) = \left[\frac{p_y^2}{2m} + \frac{1}{2}m\omega_c^2\left(y - y_k\right)^2\right]\chi(y) \qquad (5.9)$$

with $\omega_c = \frac{eB}{m}$, $y_k = \ell_B^2 k$, and $\ell_B^2 = \frac{\hbar}{eB}$. Note that the momentum k of the plane waves determines the apex y_k of the parabola. The eigenenergy spectrum of the harmonic oscillator reads

$$\epsilon_\nu = \hbar\omega_c\left(\nu + 1/2\right), \qquad \nu \geq 0 \qquad (5.10)$$

---

[1] We can also calculate at first the Green's function of the 2DEG [55, Section 1.2 and 3.2]

$$G(\boldsymbol{r}, \boldsymbol{r}', E) = -\mathrm{i}\frac{m}{2\hbar^2}H_0^{(1)}\left(k\left|\boldsymbol{r} - \boldsymbol{r}'\right|\right), \qquad (5.7)$$

where $k = \sqrt{2mE}/\hbar$ and $H_0^{(1)}$ is the Hankel function of first kind of zero order [3]. Using $\mathrm{Re}\left(H_0^{(1)}(0)\right) = 1$, we can calculate the DOS per unit area by $D(E) = -\mathrm{Tr}\left(\mathrm{Im}\left(G(E)\right)\right)/\pi S$ and arrive at (5.3).

[2] We could also go to higher orders in the finite differences approximation, but this would also increases the computational effort due to next-nearest neighbor interactions.

and the eigenfunctions

$$\psi_{k,\nu}(\boldsymbol{r}) = c_\nu \, \mathrm{e}^{\mathrm{i}kx} \, \mathcal{D}_\nu\left(\frac{y - y_k}{\ell_B}\right),\tag{5.11}$$

where

$$\mathcal{D}_\nu(y) \equiv \frac{D_\nu(\sqrt{2}y)}{\sqrt{\nu!}}\tag{5.12}$$

are rescaled parabolic cylinder functions [3] and c_ν is a normalization constant. When the 2DEG is infinitely extended in the whole xy-plane, the index ν has to be an integer $n = 0, 1, 2 \ldots$, because the eigenfunctions have to be normalizable. In this case, the parabolic cylinder functions can be simplified by $\mathcal{D}_n(y) = \mathrm{e}^{-y^2/2} H_n(y)/\sqrt{2^n n!}$, where $H_n(y)$ are the Hermite polynomials. The eigenenergy spectrum shows a series of equidistant Landau levels. The constant DOS of the 2DEG is condensed by the magnetic field onto these Landau levels, which can be filled with $N = 1/2\pi\ell_B^2$ electrons (per unit area). However, when the 2DEG is bounded, also non-integer values of ν are possible, as shown in Section 5.2.3.
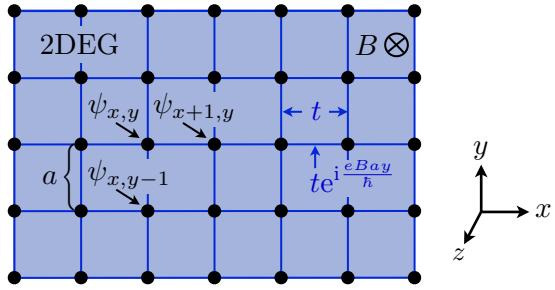
Figure 5.1: The transport through a two-dimensional electron gas (2DEG) under the effect of a homogeneous perpendicular magnetic field $\boldsymbol{B} = -B\boldsymbol{e}_z$ is studied in this Chapter. To evaluate numerically the Green's function (2.20) and the transmission function (2.33), we use a finite differences approximation of the Hamiltonian. $\psi_{x,y}$ denotes the wave function at discrete supporting points on a square lattice with spacing a. The magnetic field is taken into account by complex phase factors in the horizontal couplings.

Applying a finite differences approximation to the Hamiltonian (5.8), we obtain

$$H_{\mathrm{2DEG}}^{\mathrm{FDA}} = 4t\psi_{x,y} - t\left(\psi_{x,y+1} + \psi_{x,y-1}\right) - t_B\psi_{x+1,y} - t_B^*\psi_{x-1,y}\tag{5.13}$$

with

$$t_B = t\left(1 + \mathrm{i}\frac{eBay}{\hbar} + \frac{1}{2}\left(\mathrm{i}\frac{eBay}{\hbar}\right)^2\right) \approx t\exp\left(\mathrm{i}\frac{eBay}{\hbar}\right).\tag{5.14}$$

The last step is justified, if the magnetic flux through a discretization cell $\phi = Ba^2$ is much less than a magnetic flux quantum $\phi_0 = h/e$. In this case, also under the effect of a magnetic field, the finite differences approximation of a 2DEG is equivalent to a tight-binding ribbon, see (3.5) and Section 2.1.2.

To summarize, the finite differences approximation of a 2DEG is feasible, if the discretization a is so small that the Fermi energy (measured in multiple of $t \propto 1/a^2$) is close to the band edge and the magnetic flux through a discretization cell ($\propto a^2$) is much less than a magnetic flux quantum.

5.2 Magnetotransport along boundaries: Electron focusing and edge channels

When electrons are injected coherently at one point on the boundary of a 2DEG, they can be focused by a perpendicular magnetic field B onto another point of that boundary [178], see the blue trajectories in Figure 5.2. In the classical regime, resonances are observed when a multiple of the cyclotron diameter equals the distance between the injecting and collecting point contacts. For large Fermi wavelength and long phase coherence length, additional interference effects are observed. This regime of *coherent electron focusing* has been studied for the first time by van Houten et al. [181]. Recently, the effects of disorder [118] and spin-orbit interaction [47, 107, 152, 154, 179] were investigated and focusing experiments in graphene were performed [174]. It was also discussed to study by coherent electron focusing the structure of graphene edges [149] as well as Andreev reflections in normal-superconductor systems [82, 146, 150]. Moreover, a 2DEG in a strong magnetic field shows the quantum Hall effect, which is explained by the transport through *edge channels* straight along the boundary of the system, see the red lines in Figure 5.2.

Although the coherent electron focusing and the quantum Hall effect have been studied extensively in the last two decades, to our knowledge the two regimes have always been separated. Here, we intermix the two regimes by suitable system parameters and study theoretically the properties of the focusing experiment emerging at the transition from the classical cyclotron motion to the quantum Hall edge channel transport. We have published the results of this Section in [169].

5.2.1 System

We study a 2DEG with a size of $800\,\text{nm} \times 500\,\text{nm}$ sketched in Figure 5.2. Metallic contact regions with a width of $10\,\text{nm}$ are attached at the boundaries of the system separated by a distance $\Delta x = 500\,\text{nm}$. A finite differences approximation with discretization $a = 5\,\text{nm}$ is applied, corresponding to the coupling $t = \hbar^2/2ma^2 \approx 21.8\,\text{meV}$. We assume that the 2DEG is formed at the interface of a GaAs-AlGaAs heterostructure, for which the effective electron mass is $m = 0.07m_e$. The chemical potential is set to $\mu = 0.5t \approx 10.9\,\text{meV}$. As the corresponding Fermi wavelength $\lambda_F \approx 45\,\text{nm}$ is comparable with the characteristic dimensions of the system, we can expect to observe quantum effects due to the interference of the coherent electrons. We assume that experimentally, the influence of the temperature is negligible and thus, we set the temperature to zero. The Zeeman spin splitting $\varepsilon_z = g\mu_B B$ (with the Bohr magneton $\mu_B = e\hbar/2m_e$) is not resolved in this system, because in GaAs both the effective g-factor and the effective mass (measured in multiples of m_e) are $\ll 1$ and thus, the spin splitting is typically one order of magnitude smaller than the Landau splitting $\varepsilon_L = \hbar\omega_c$.

In order to allow better comparison of the NEGF calculations with a minimal model, we assume hard-wall boundary conditions. However, this assumption is not essential for our findings, see Section 5.2.5. We also introduce additional virtual decoherence reservoirs at those boundaries, which are not essential for the focusing experiment, see the dashed boundaries in Figure 5.2. By randomizing the electron phase and momentum, see Chapter 4, such *diffusive walls* mimic an open system and thus suppress finite size effects, like standing waves between the boundaries of the system. They also greatly reduce spurious
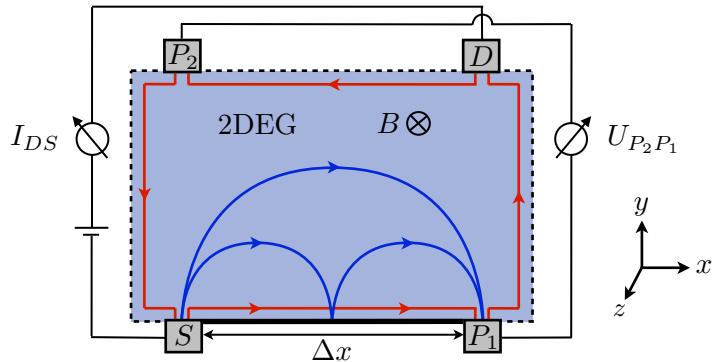
Figure 5.2: A 2DEG with a size of $800\,\text{nm} \times 500\,\text{nm}$ is studied. Contacts with a width of $10\,\text{nm}$ are attached at the boundaries separated by a distance $\Delta x = 500\,\text{nm}$. Electrons are injected by the source S and focused by a perpendicular magnetic field B onto the voltage probe P_1. We calculate the current I_{DS} between source and drain as well as the voltage drop $U_{P_2 P_1}$ between the voltage probes P_1 and P_2. Using these quantities, we study the generalized Hall resistance $R_{xy} = U_{P_2 P_1}/I_{DS}$ as a function of B. Cyclotron orbits at low magnetic field are sketched by the blue trajectories. The edge channel transport of the quantum Hall effect at high magnetic field is indicated by red lines.

focusing resonances arising from reflections at these boundaries. All reservoirs are modeled in the wide-band approximation with $\eta = 1.0t$.

Before we proceed with our magnetotransport studies, let us check briefly, if the finite differences approximation is justified for the chosen parameters. The average DOS in the system, calculated numerically by the NEGF method, is shown in Figure 5.3 by the blue curve. It agrees well with the DOS of the 2D tight-binding grid (3.10), depicted by the red curve. The numerous van Hove singularities of finite tight-binding ribbons, compare with Figure 3.2, cannot be observed, apart from some residual oscillations at the band edge. They are smoothed out efficiently by the diffusive walls. The DOS from the band edge up to the Fermi energy (dashed vertical line) is consistent with the constant DOS of a 2DEG $D(E) = 1/2\pi t a^2$ shown by the black curve. When the DOS is integrated up to the Fermi energy, a carrier density of $n_{2D} \approx 3.3 \cdot 10^{11}\,\text{cm}^{-2}$ is provided by all curves. We will apply magnetic fields up to a strength of $B = 5\,\text{T}$ corresponding to a magnetic flux $\phi/\phi_0 = 0.03 \ll 1$, as required in (5.14). Thus, for the chosen system parameters the finite differences approximation is justified to model a 2DEG.

We calculate the current I_{DS} flowing between source S and drain D due to an infinitesimal bias voltage, as well as the voltage drop $U_{P_2 P_1} = (f_{P_1} - f_{P_2})/e$ between the contacts P_1 and P_2, see Figure 5.2. By means of these two quantities, we study in the following the generalized 4-point Hall resistance [181]

$$R_{xy}(B) \equiv \frac{U_{P_2 P_1}}{I_{DS}} = \frac{h}{2e^2} \frac{\sum_j (\mathcal{R}_{P_1 j} - \mathcal{R}_{P_2 j}) T_{jS}}{T_{DS} + \sum_{ij} T_{Di} \mathcal{R}_{ij} T_{jS}}, \tag{5.15}$$

as a function of the perpendicular magnetic field B. In the last step, we applied the multi-terminal formula for the potential of the voltage probes (2.38) as well as for the current between source and drain (2.40).
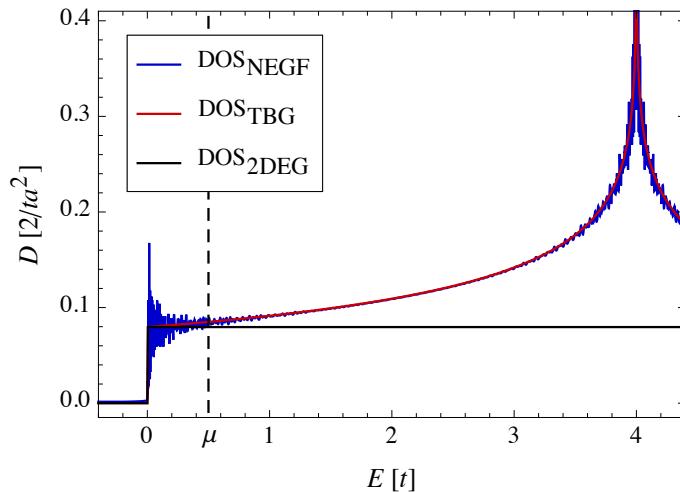
Figure 5.3: The average DOS in the magnetotransport device, calculated by the NEGF method (2.5), (blue curve), agrees well with the DOS in a tight-binding grid (3.10), (red curve). The DOS from the band edge up to the Fermi energy $\mu = 0.5t$ (dashed vertical line) is consistent with the constant DOS of a 2DEG (5.3), (black curve). The energy resolution is $\Delta E = 10^{-3}t$.

5.2.2 Cyclotron orbits

The *focusing spectrum* of the 2DEG, defined as the generalized Hall resistance R_{xy} as a function of the magnetic field B, is shown in Figure 5.4. The blue curve gives R_{xy} in the case of specular reflections at the boundary between S and P_1, while for the red curve a diffusive boundary was assumed. This figure is one of the main results of this thesis and it is discussed in detail in the following. Let us start with a low magnetic field $0\,\mathrm{T} < B < 2\,\mathrm{T}$, in which equidistant peaks at

$$B_n = \frac{\sqrt{8m\mu}}{e\Delta x}n, \qquad n = 1, 2, 3\ldots, \tag{5.16}$$

are found (vertical dashed lines). As sketched by the blue trajectories in Figure 5.2, electrons injected by the source S are guided on cyclotron orbits and end in P_1 after $n-1$ reflections at the wall in between, if a multiple of the cyclotron diameter $2\,|\boldsymbol{p}|\,/eB$ equals the distance Δx. These cyclotron orbits can be clearly seen in Figure 5.5, which shows the local current and the LDOS of electrons originating from S with energy μ. They can also be imaged experimentally by means of a scanning probe microscope [6]. Note that the local current shows caustics due to the injection of the electrons with a broad distribution of angles. Moreover, the interference of the coherent electrons gives rise to a fine structure in the focusing spectrum and the local current. These effects, which are also observed in focusing experiments [18, 181], can be suppressed, if the distribution of the injection angles is narrowed by reducing the distance of the injector to the left diffusive wall, see the focusing spectrum and the local current in Figure 5.6. In Figure 5.4, the focusing peaks cannot be observed when the magnetic field is reversed ($B < 0\,\mathrm{T}$), apart from a single peak at a low magnetic field, which arrises when the cyclotron diameter equals the distance between S and P_2.
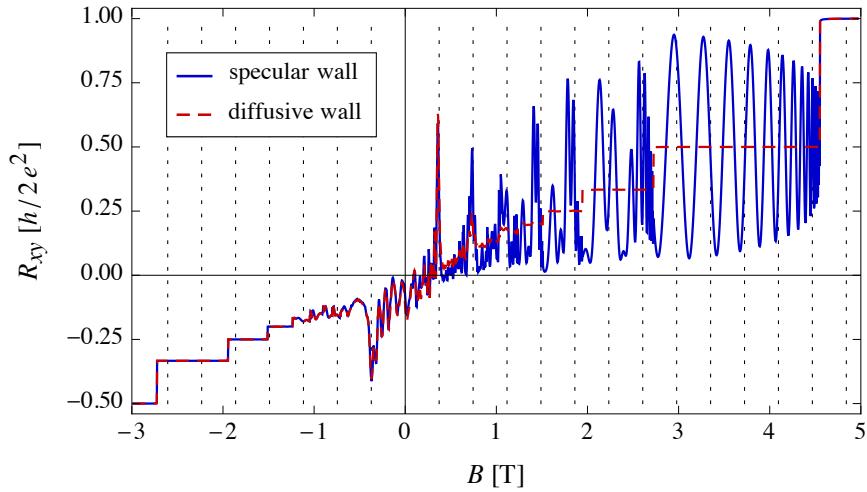
Figure 5.4: The Hall resistance $R_{xy} = U_{P_2 P_1}/I_{DS}$ as a function of the magnetic field B. In weak fields, R_{xy} shows equidistant focusing peaks indicated by dashed vertical lines, when a multiple of the cyclotron diameter equals Δx. In intermediate fields, anomalous oscillations appear, which are neither periodic in $1/B$ nor in B. A single Hall plateau is found in large fields, whereas lower Hall plateaus can only be seen when specular reflections are suppressed by an absorbing diffusive wall between S and P_1 or by reverting the magnetic field.
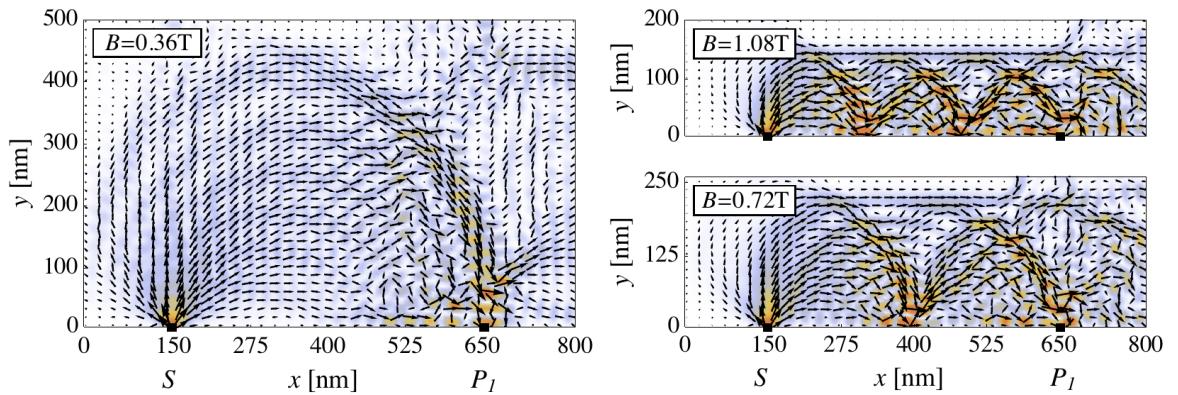
Figure 5.5: The local current (arrows) and the LDOS (color shading, increasing from white over blue to red) of the electrons originating from S with energy μ. The cyclotron orbits can be clearly seen. Also caustics are evident, which are due to the injection of electrons with a broad distribution of angles. The fine structure is caused by the interference of the coherent electrons. Note that only the relevant part of the system is shown at $B = 1.08\,\mathrm{T}$ and $B = 0.72\,\mathrm{T}$.
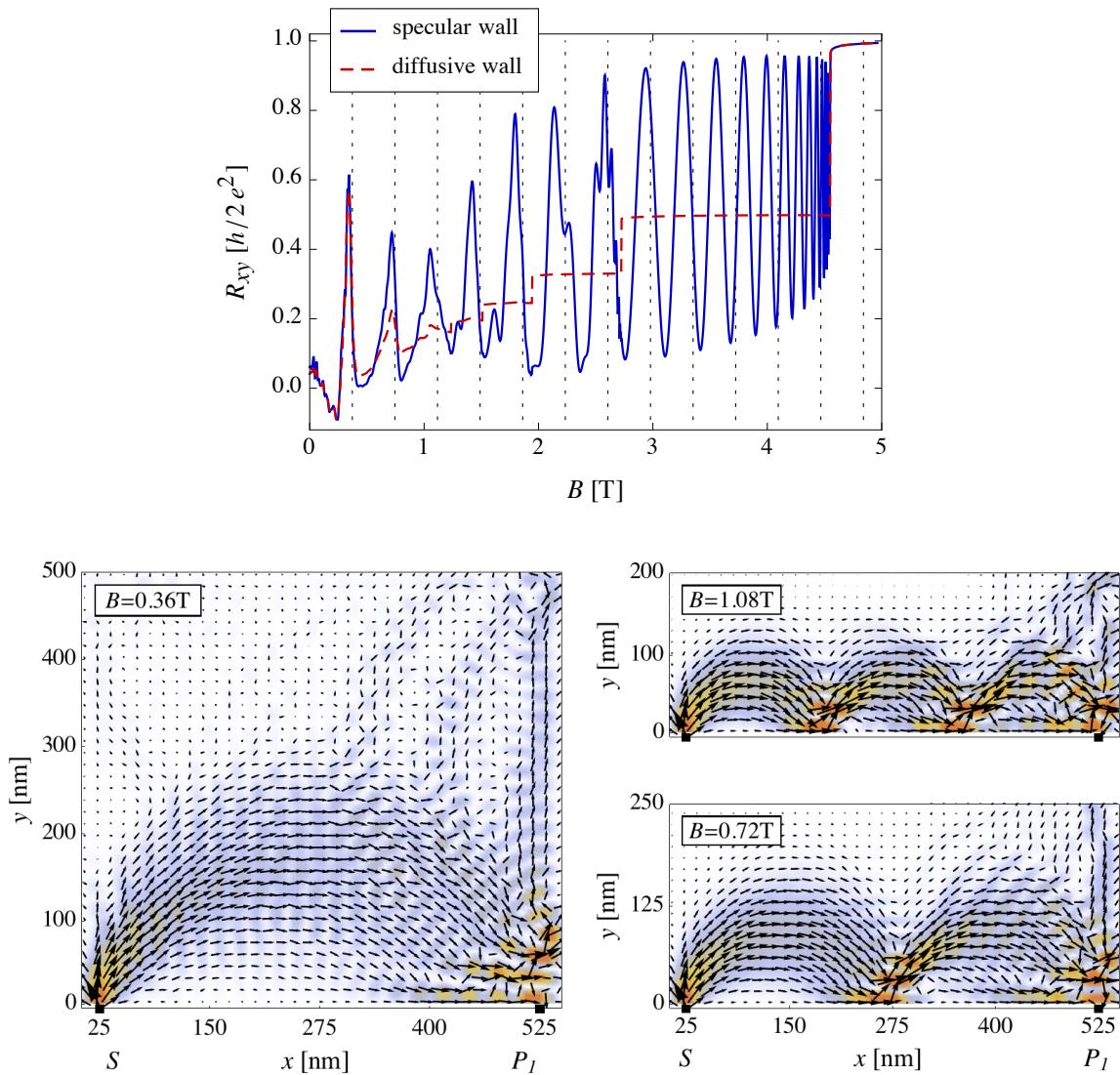
Figure 5.6: Focusing spectrum and local current, when the distribution of the electron injection angles is narrowed by reducing the distance of the injector to the left absorbing wall. Fine structure and caustics are suppressed.

5.2.3 The quantum Hall effect

For $B < -1\,\mathrm{T}$, we observe instead of focusing peaks a sequence of extended plateaus in the Hall resistance

$$R_{xy} = \frac{h}{2e^2}\frac{1}{n}, \qquad n = 1, 2, 3\ldots, \tag{5.17}$$

which indicates the quantum Hall effect. Although the discovery of the quantum Hall effect dates back to 1980 [180], it is still a hot topic as shown, for example, by the recent discovery of the quantum spin Hall effect [106, 127] and the quantum anomalous Hall effect [33, 137]. Further research is also stimulated by the fact that the quantum Hall regime is topologically insulating. All current is carried in edge channels along the boundary of the

system, while the bulk is insulating. This edge channel transport, sketched by the red lines in Figure 5.2, can be seen clearly in Figure 5.7 (first row), which shows the local current and the LDOS at the Fermi energy. It can also be seen in the second row of Figure 5.7, which shows the transverse current (red curve) and the LDOS (blue curve) at the dashed line in the figures of the first row. The magnetic field in Figure 5.7 corresponds to the resistance plateaus $R_{xy} = 1/3$ (left column) and $R_{xy} = 1/2$ (right column), respectively.

In order to understand the resistance quantization and the edge channel transport, we give an elementary introduction into the quantum Hall effect, which is based on [18, 42, 148]. We have learned in Section 5.1.2 that in a magnetic field the constant DOS of a 2DEG is condensed on equidistant Landau levels. This can also be observed in Figure 5.7 (fourth row), where the blue curve gives the numerically calculated average DOS in the magnetotransport device, while the red horizontal lines indicate the expected positions of the Landau levels (5.10). For low energies $E \lesssim \mu$, the positions of the Landau levels agree well with the numerical data. For higher energies, deviations can be observed, because the finite differences approximation of the 2DEG looses its validity, compare with Figure 5.3.

As transport in the quantum Hall regime takes place at the edges of the system, let us study a minimal model, namely an infinitely extended 2DEG bounded by a single infinite potential wall along the x-axis. In this case, the index ν in the eigenenergies (5.10) and the eigenfunctions (5.11) is determined by the hard-wall condition $\psi_{k,\nu}(x,0) = 0$. The eigenenergy spectrum in Figure 5.8 (left) shows that for sufficiently large k the influence of the infinite wall is negligible and the Landau levels for integer values of ν can be observed. However, the energy bands are bent upwards, when k is decreased and the apex of the parabola $y_k = \ell_B^2 k$ in (5.9) approaches the wall. We calculate the k_n, which agree with a given Fermi energy and a given magnetic field, see the marked intersection points in Figure 5.8 (left). The k_n as a function of the magnetic field are shown in Figure 5.8 (right). The energy resolved LDOS in Figure 5.9, calculated by means of the k_n and the corresponding eigenfunctions (5.11),

$$D(E, \boldsymbol{r}) = \sum_{i=1}^{n} |\psi_{k_i,\nu}(\boldsymbol{r})|^2, \qquad \nu = \frac{E}{\hbar\omega_c} - \frac{1}{2} \tag{5.18}$$

shows clearly the bending of the energy bands in vicinity of a boundary. It looks very similar to the dispersion relation, because of the identity $y_k = \ell_B^2 k$. However, the LDOS is nonzero only for $x > 0$ (hard wall), whereas for the dispersion all values of k are allowed (apex of the parabola can be located behind the wall). The same behavior can be seen in Figure 5.7 (third row), where the NEGF method is applied to calculate the LDOS in the magnetotransport device. Note that in this case the LDOS is slightly larger than in the minimal model, because the contacts induce additional states in the system, see the blue and green curves in Figure 5.7 (second row).

Let us assume that the Fermi energy is in between two Landau levels. In this case, we learn from the LDOS that the eigenstates are localized close to the edge of the system. As the slope of the eigenenergy bands in Figure 5.8 is negative at all k_n, the group velocity of all these edge states points in the same direction. Thus, all edge states at a boundary of the system carry the current in the same direction. At the opposite boundary the slope of the eigenenergy bands is reversed and the current flows in the opposite direction. Inside the system no allowed states exist, which hence is insulating. This spatial separation of the states carrying current in one direction from the states carrying current in the opposite direction makes the quantum Hall effect so exceptional.
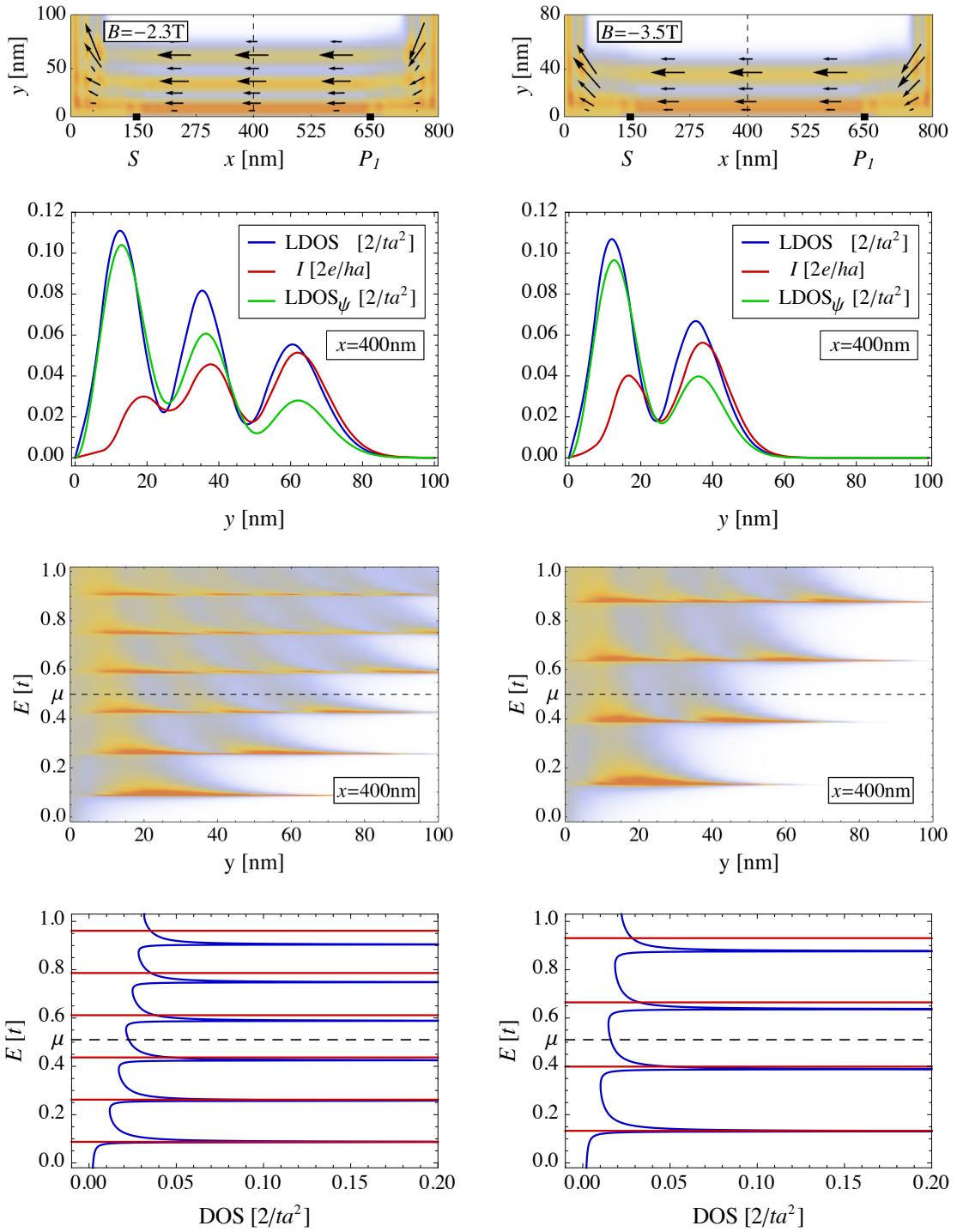
Figure 5.7: Quantum Hall effect at $B = -2.3\,\text{T}$ (left column) and $B = -3.5\,\text{T}$ (right column) corresponding to $R_{xy} = 1/3$ and $R_{xy} = 1/2$, respectively. First row: Local current and LDOS. Edge channels can be clearly seen. Second row: Transverse current and LDOS at the dashed line in the figures of the first and third row. The green curve gives the LDOS due to (5.18). Third row: Energy resolved LDOS. The Landau levels are bent upwards close to the system edge, which causes the edge channels. Fourth row: Average DOS (blue curve) and expected positions of the Landau levels (red horizontal lines).
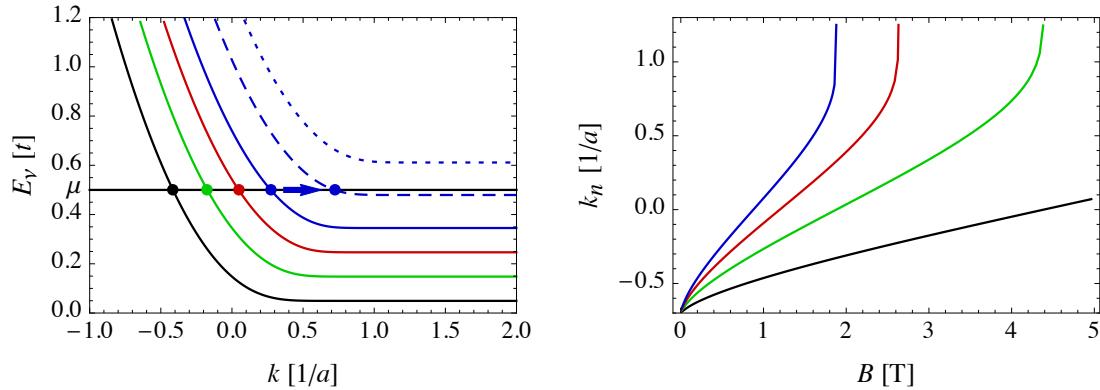
Figure 5.8: Left: Eigenenergy bands of an infinitely extended 2DEG bounded by an infinite potential wall at $y = 0$. The solid curves give the first four energy bands at $B = 1.3\,\mathrm{T}$, while the dashed and the dotted curves give the fourth energy band at $B = 1.8\,\mathrm{T}$ and $B = 2.3\,\mathrm{T}$, respectively. The dots indicate the k_n at the Fermi energy. The arrow points out the increase of k_4, when the corresponding Landau level approaches μ. Right: The k_n as a function of the magnetic field.
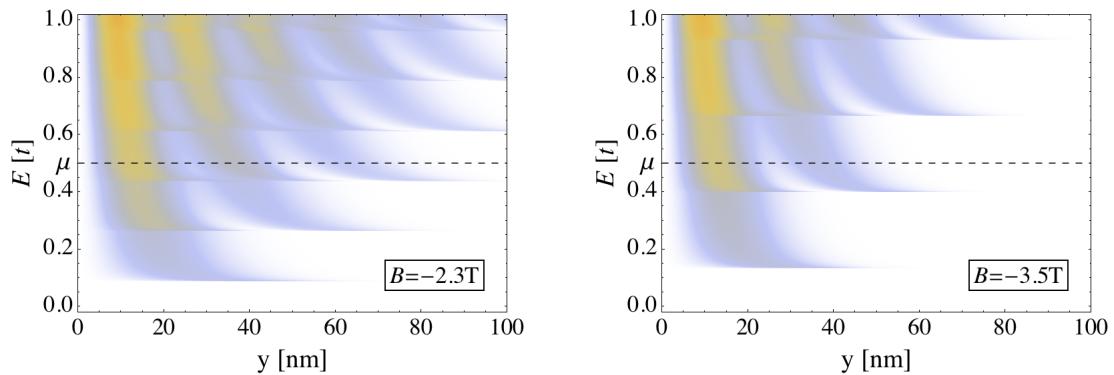
Figure 5.9: Energy resolved LDOS (color shading) of a 2DEG bounded by an infinite potential wall at $y = 0$. The LDOS (5.18) is calculated by the k_n from Figure 5.8 and the corresponding eigenfunctions (5.11). The Landau levels, which can be observed deep inside the 2DEG, are bent upwards in vicinity of the wall. When the Fermi energy is in between two Landau levels, as shown, the eigenstates are localized close to the edge. These edge states are perfect ballistic conductors, which give rise to the quantized resistance. The LDOS at the Fermi energy is also shown by the green curve in Figure 5.7 (second row).

In the edge channels backscattering is absent, because to reverse the momentum an electron has to be scattered to the opposite edge of the system. This is in turn impossible, because no allowed states exist inside the system and the probability for direct tunneling between opposite edges is exponentially small. Because of this absence of backscattering, each edge channel is a perfect ballistic conductor with transmission $T = 1$. Therefore, for the total transmission, we just have to count the number of edge channels, or in other words, the number of Landau levels below the Fermi energy.[3] For example, at $B = -2.3\,\mathrm{T}$ three

Landau levels are below the Fermi energy, three edge channels are occupied and the Hall resistance $R_{xy} = 1/3$, see Figure 5.7 (left column). The distance of the Landau levels $\hbar\omega_c$ increases with the magnetic field. However, as long as the Fermi energy is in between two Landau levels the number of edge channels is constant and thus, the Hall resistance shows an extended plateau. Only when a Landau level is pushed above the Fermi energy, an edge channel is depleted and the Hall resistance jumps to the next plateau.

In real experiments the Fermi energy is not constant but the charge density. In an idealized system, the Fermi energy would be pinned always at a Landau level, because the number of edge states is much less compared to the number of bulk states condensed onto the Landau levels. When the Fermi energy lies in a Landau level, allowed states exist also inside the system and backscattering takes place as in Ohmic conductors. The resistance plateaus would be shrunk to single points and the conventional Hall line would be observed. However, in real systems some degree of disorder is always present, which induces additional localized states [148, Chapter 1 and 3]. These states do not contribute to transport but help to stabilize the Fermi energy between two Landau levels. In this case the DOS is broadened as in our magnetotransport device, see Figure 5.7 (fourth row). However, the origin of these states is different in our case: The Landau levels are broadened due to the finite lifetime of the states and additional states can be induced by the contacts [73]. Our device is also relatively small, which makes the number of edge and bulk states comparable. Thus, the assumption of a constant Fermi energy displaces slightly the transitions between the Hall plateaus but does not change qualitatively our results, see also [65].

Note that the quantized Hall resistance has the same form as the quantized resistance of a ballistic conductor, see Figure 3.11. However, in the experiment the quantization in ballistic conductors is usually not very precise, because the transport takes place in the whole system and backscattering due to some disorder cannot be avoided. In contrast, the quantization of the Hall resistance can be extremely precise, because backscattering is topologically forbidden. Moreover, we have learned that some disorder can help to observe distinct plateaus. As a result, the quantum Hall effect will be used for the redefinition of the SI system.[4] Figure 5.10 shows the Hall resistance (left) and the DOS (right) as a function of the magnetic field and the energy. The resistance plateaus as well as the so-called Landau fan of the spreading energy levels can be clearly seen. The Landau fan can also be found in the bottom left-hand corner of Hofstadter's butterfly shown on the cover page of this thesis.

5.2.4 Anomalous resistance oscillations

In Figure 5.4, the quantum Hall staircase is found at a positive magnetic field only, if a diffusive wall is introduced in between injector S and collector P_1, see the dashed red curve. If the reflections at the boundary are specular, we observe for $B > 2\,\text{T}$ an additional set of resistance oscillations, which cannot be explained by classical trajectories. The frequency of these oscillations increases rapidly whenever a Landau level is pushed towards the Fermi energy and a transition between Hall plateaus appears (compare solid blue and dashed red curves in Figure 5.4). Moreover, when only two edge channels are occupied

---

[3]Alternatively, we can simplify at first (5.15) under the constraint that the only non-zero transmission functions are $T_{P_2 S} = T_{D P_2} = T_{P_1 D} = T_{S P_1} = n$, where n is the total number of occupied Landau levels. We obtain then for the Hall resistance $R_{xy} = 1/n$.

[4]For further information to this ongoing project see: `www.bipm.org/en/si/new_si`
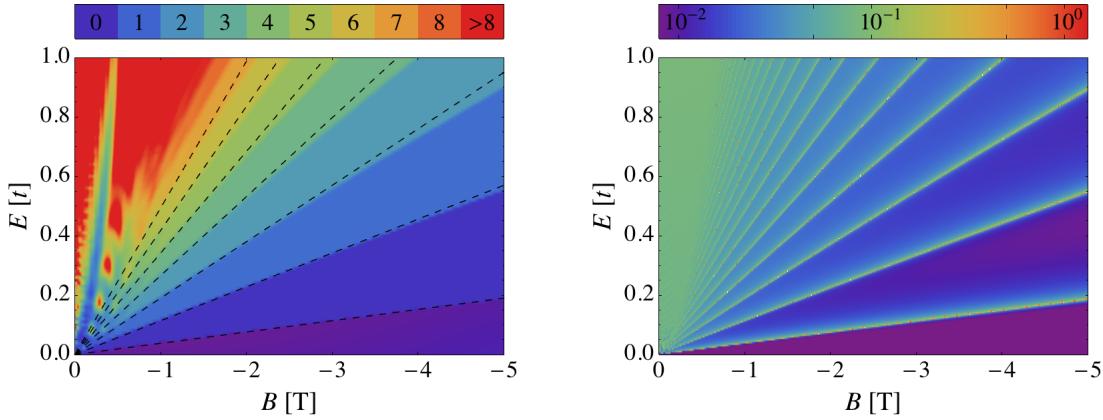
Figure 5.10: Left: Hall resistance $R_{xy} = 1/n$ as a function of the magnetic field and the energy. The color shading gives the number n of occupied Landau levels. At low magnetic field a residual focusing peak appears, when the cyclotron diameter equals the distance between S and P_2. The expected positions of the Landau levels (5.10) are indicated by dashed lines. Deviations can be observed at higher energies and higher magnetic fields, because the finite differences approximation of the 2DEG looses its validity. Right: DOS as a function of the magnetic field and the energy. The so-called Landau fan of the spreading energy levels can be clearly seen. This figure can be found also in the bottom left hand corner of Hofstadter's butterfly shown on the cover page.

$(2.7\,\text{T} < B < 4.5\,\text{T})$, the oscillations become very clear and regular. Finally, the oscillations vanish completely, when only a single edge channel is occupied $(B > 4.5\,\text{T})$, and the Hall plateau $R_{xy} = 1$ can be observed.

This suggests that these oscillations are an interference phenomenon between the occupied edge channels. Let us consider again the minimal model consisting of an infinitely extended 2DEG bounded by an infinite potential wall along the x-axis. The eigenenergy spectrum of the 2DEG is shown in Figure 5.8 to the left, while the k_n of the occupied edge channels as a function of the magnetic field are depicted to the right. We take into account only the plane wave part of the edge states (5.11), which propagate along the infinite wall, and calculate the superposition of the different k_n with equal weights. The normalized absolute square is given by

$$|\psi_{\text{coherent}}|^2 = \frac{1}{n^2} \left\langle \left| \sum_{i=1}^{n} e^{ik_i \Delta x} \right|^2 \right\rangle_{S,P_1}, \tag{5.19}$$

where $\langle \cdot \rangle_{S,P_1}$ means spatial averaging over the finite width of the injector and collector. The absolute square value of the superimposed plane waves shows remarkable agreement with the NEGF calculation of the focusing spectrum, see Figure 5.11. Thus, the focusing peaks in low magnetic fields, which correspond to classical trajectories, can also be explained by the interference of multiple edge channels [18, 181]. Moreover, this explanation of the focusing spectrum is valid for every strength of the magnetic field and allows to understand the anomalous peaks.
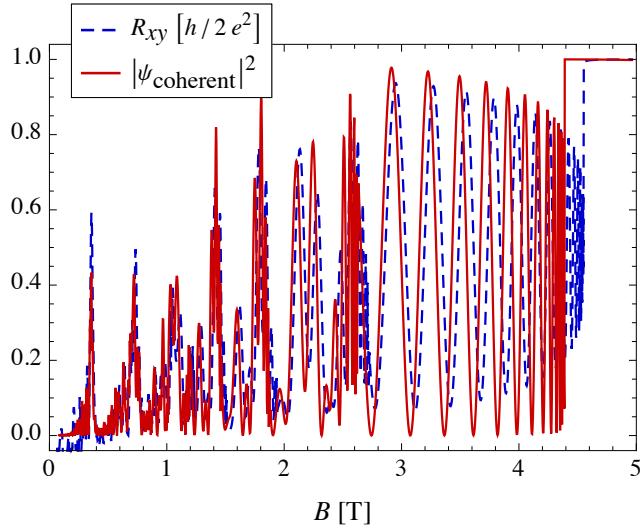
Figure 5.11: Normalized absolute square of the superimposed plane wave part of the occu-
pied edge channels (5.19), (solid red curve). A remarkable agreement with the
NEGF calculation of Figure 5.4 (dashed blue curve) can be observed. Thus,
all resistance oscillations can be understood by the interference of the edge
channels. The anomalous resistance oscillations are beatings, which appear
when only some few edge channels are occupied.

In intermediate fields, the current is carried by only a few edge channels and the focus-
ing spectrum shows beatings due to the superposition of plane waves. In particular, when
only two edge channels are occupied, only two plane waves are superimposed and a beating
appears, whose frequency is determined by the difference of k_1 and k_2. The frequency of
the oscillations increases rapidly, whenever the highest occupied Landau level approaches
the Fermi energy, because its intersection point and thus, the corresponding $k_{\max}$ increases
strongly, see solid, dashed and dotted blue curve in Figure 5.8 (left) as well as the diver-
gencies in Figure 5.8 (right). The difference of $k_{\max}$ to the other, much smaller k_n leads to
a high frequency beating. Finally, when only a single edge channel is occupied, the beating
and thus, the oscillations in the focusing spectrum vanish. The current then flows along
an edge channel parallel to the wall, see the top of Figure 5.12. This figure also illustrates
that although the focusing peaks in intermediate fields cannot be explained by classical
trajectories, the local current resembles to some extent cyclotron motion along the wall.

The clear and distinct oscillations due to the occupation of only two edge channels can
also be understood as a new commensurability between the magnetic flux enclosed within
the two edge channels and the flux quantum. At the maximum of the oscillations the
two plane waves interfere constructively and thus, the difference of their momenta fulfills
$\Delta k = 2\pi/\Delta x$. If we relate this momentum difference to the distance between the edge
channels $\Delta y_k = \ell_B^2 \Delta k$, we obtain

$$\Delta x \Delta y_k B = \frac{h}{e}. \tag{5.20}$$

Thus, between two successive focusing peaks, the magnetic flux within the area enclosed
by the two edge channels increases by one flux quantum. In this way, we can relate the

focusing spectrum to the distance of the edge channels and the difference of their momenta. For the experimental observation of such interference effects with a fixed distance between the edge channels, see e.g. [49] and references therein.

When the electron phase is randomized by diffusive scattering at the walls, we do not have to sum up the plane waves but their absolute value

$$|\psi_{\text{incoherent}}|^2 = \frac{1}{n^2} \left\langle \sum_{i=1}^{n} \left| e^{ik_i \Delta x} \right|^2 \right\rangle_{S,P_1} = \frac{1}{n}, \tag{5.21}$$

which leads to the quantum Hall staircase. Note that indeed many properties of the system can be understood by basic quantum calculations. However, this cannot replace the NEGF approach, which allows to include contacts in a controlled way and to obtain quantitative results for the Hall resistance. Moreover, the superposition of plane waves with equal weights is justified only by its good agreement with the NEGF calculation. The NEGF method can also be used to study the effect of partial diffusive scattering at the boundary as well as the effect of decoherence. It can also be applied easily to more complicated geometries. We use this flexibility to study in the next Section the robustness of the anomalous oscillations.
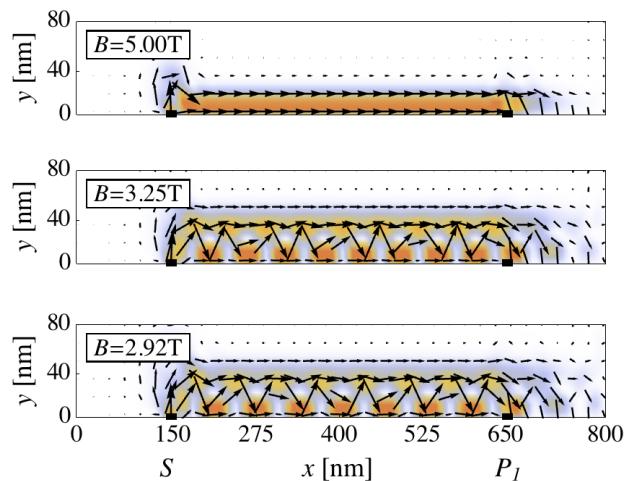
Figure 5.12: The local current and the LDOS of the electrons originating from S with energy μ. The transport through the interfering edge channels in the lower figures resembles to some extent a cyclotron motion, while at $B = 5\,\mathrm{T}$ the current is carried through a single edge channel straight along the wall. Only the relevant part of the system is shown.

5.2.5 Effects of decoherence, non-specularity, boundary conditions and contact geometry

Let us study the effect of decoherence on the focusing experiment by means of our statistical model, discussed in Chapter 4. The decoherence averaged focusing spectrum in Figure 5.13 shows that with increasing degree of phase and momentum randomization all oscillations

are suppressed and the surprisingly robust Hall plateaus appear [64, 65, 194]. The classical focusing peaks are even stronger suppressed than the anomalous oscillations, because the latter are located in a much narrower part of the system and thus, are less influenced by the decoherence reservoirs. The LDOS and the local current of electrons originating from the source show distinct edge states while the cyclotron orbits are vanishing, because the interference between the edge channels is annihilated by the decoherence. Note that the LDOS is also strongly broadened by the decoherence. As expected, when the degree of decoherence is further increased ($p > 0.05$) the quantum Hall plateaus vanish and the classical linear Hall resistance appears.

Our model also allows us to study the effects of partially specular reflections by introducing between S and P_1 a diffusive wall with the broadening parameter η_{dw}. In this way, we can tune the scattering from specular ($\eta_{\mathrm{dw}} = 0$) to diffusive ($\eta_{\mathrm{dw}} \sim t$). Figure 5.14 (left) shows that the oscillations in the focusing spectrum are suppressed gradually with increasing degree of non-specularity and increasing number of reflections at the boundary. By means of the NEGF method, we can also study easily the influence of the contact geometry on the focusing spectrum. Using contacts with a width of $30\,\mathrm{nm}$, attached via $120\,\mathrm{nm}$ long leads, we observe in Figure 5.14 (right) qualitatively the same focusing spectrum, which clearly shows classical focusing peaks as well as anomalous oscillations. Moreover, our findings are not dependent on the chosen boundary conditions (i.e. hard wall). When a parabolic confining edge potential is used, qualitatively similar results are obtained.

5.2.6 Experimental observability

To our knowledge, in focusing experiments such system parameters have been used that the regime of coherent electron focusing and the quantum Hall effect are well separated, see e.g. Figure 10 in [181]. The reason for this separation is that the number of observable focusing peaks is limited in the experiment, because decoherence and diffusive scattering at the boundary cannot be completely avoided. In order to observe anomalous resistance oscillations due to the interference of some few edge channels, the distance Δx between injector and collector as well the Fermi energy μ have to be tuned in such a way that the maximal number of possible specular reflections fulfills the rule of thumb

$$n_{\mathrm{max}} \sim \frac{1}{6} \frac{\Delta x}{a} \sqrt{\frac{\mu}{t}}, \tag{5.22}$$

which can be derived easily by (5.10) and (5.16). Of course, mean free path and phase coherence length also have to be comparable with Δx.

In our calculations we have used parameters ($m = 0.07 m_e$, $\mu = 10.9\,\mathrm{meV}$, $n_{\mathrm{2D}} = 3.3 \cdot 10^{11}\,\mathrm{cm}^{-2}$) of a high quality 2DEG in a GaAs-AlGaAs heterostructure. We expect that the omission of the spin splitting will not change the results qualitatively. Figure 5.13 shows that the oscillations can be observed up to a degree of decoherence of $p = 0.005$, which corresponds to a phase coherence length of approximately $1\,\mu\mathrm{m}$. Likewise, a distance between S and P_1 of $500\,\mathrm{nm}$ is easily achievable with today's nanolithography techniques. All this gives us confidence that the predicted oscillations can indeed be observed experimentally. Signs of these anomalous oscillations have already been observed in different geometries [59, 60].
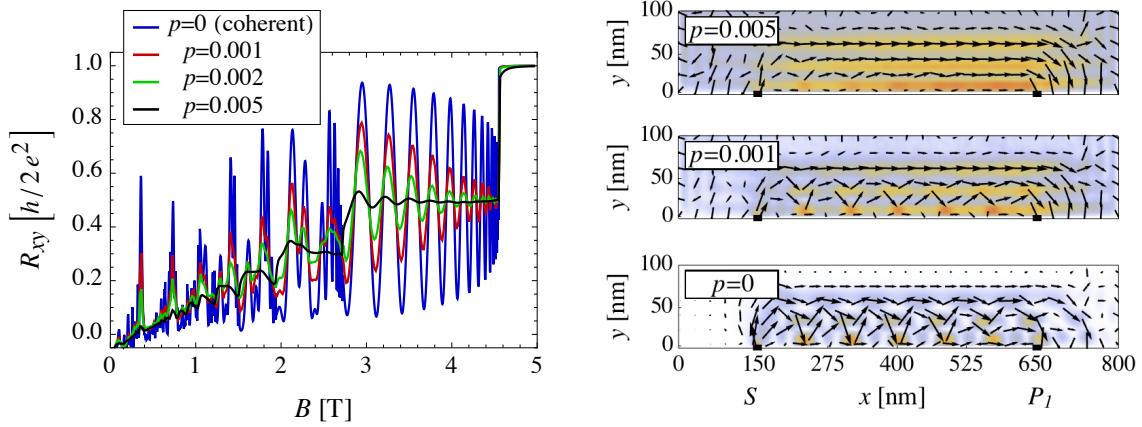
Figure 5.13: Influence of an increasing degree of decoherence on the focusing spectrum as well as the LDOS and local current ($B = 2.13\,\text{T}$) for electrons originating from the source. The oscillations are gradually suppressed and isolated edge channels remain. Averages are over 75 decoherence configurations.
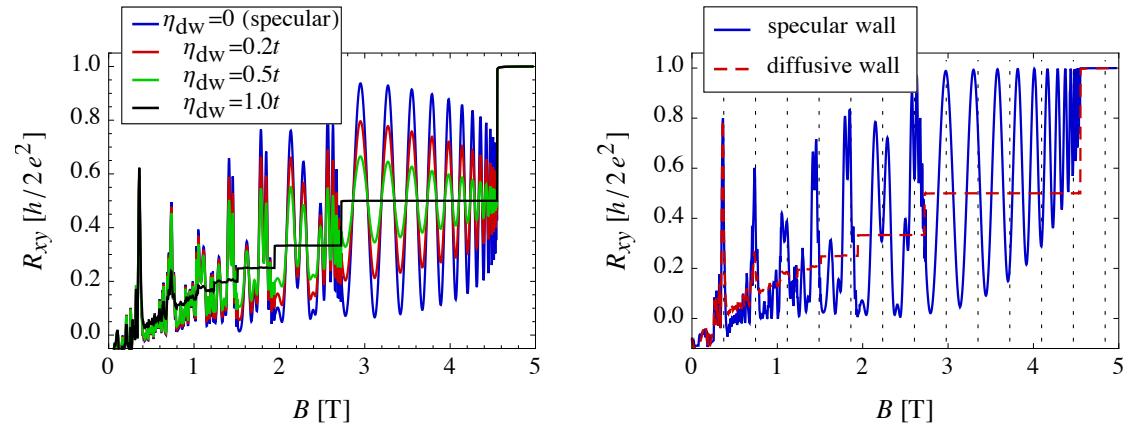
Figure 5.14: Left: Focusing spectra for an increasingly diffusive boundary. Oscillations in the focusing spectrum are suppressed gradually with increasing degree of non-specularity and increasing number of reflections. Right: Focusing spectrum in the case of 30 nm wide reservoirs attached via 120 nm long leads. Classical focusing peaks as well as anomalous oscillations can be observed clearly.

5.3 Graphene's relativistic 2D electron gas

In this Section, we extend our studies to the relativistic electron gas in graphene, a two-dimensional honeycomb lattice of carbon atoms, see Figure 5.15. Actually, much work discussed in this thesis has been performed with a graphene based device, namely an ordinary pencil used since ancient times.[5] The core of a pencil consists of graphite, which is a stack of graphene layers coupled weakly by van der Waals forces. When we write with a pencil, we rub off graphene stacks and somewhere maybe also an individual layer of graphene. However, a single layer of graphene has not been isolated until 2004 by Novoselov and Geim [131], who were awarded for their work with the Nobel prize in 2010. Nowadays, graphene is maybe the most studied material in condensed-matter physics,[6] because of its numerous exceptional properties and their potential technological applications, see [13, 66, 67, 129] and references therein for an overview. In the following, we give a very short introduction into the physics of graphene and discuss some of its remarkable properties. Afterwards, the magnetotransport along the boundary of graphene nanoribbons is studied. As a starting point, we can recommend the review paper by Castro Neto et al. [31] as well as [41, 71, 84, 100, 143].

5.3.1 The graphene lattice and its electronic structure

In graphene the atomic orbitals of the carbon atoms are sp^2 hybridized, which leads to a trigonal planar structure with a strong σ bond between neighboring atoms. The remaining p_z orbital is perpendicular to the plane and gives rise to a π band of delocalized electrons. Crystallographically, graphene can be described by a triangular lattice with a basis of two carbon atoms per unit cell, see Figure 5.15. The lattice vectors can be written as

$$\boldsymbol{a}_1 = \frac{a}{2}\left(3, \sqrt{3}\right), \qquad \boldsymbol{a}_2 = \frac{a}{2}\left(3, -\sqrt{3}\right), \tag{5.23}$$

where $a = 0.142\,\text{nm}$ is the distance of two neighboring carbon atoms. Equivalently, we can also speak of two interpenetrating triangular sublattices A and B. Note that the lattice constant of graphene is more than one order of magnitude smaller than the discretization length used in Section 5.2.1 for the finite differences approximation of a nonrelativistic 2DEG. This increases the computational effort to study theoretically graphene devices.

The tight-binding Hamiltonian of graphene is given by

$$H = -t \sum_{\langle ij \rangle} |\phi_j^A\rangle \langle \phi_i^B| + \text{H.c.,} \tag{5.24}$$

where $\langle ij \rangle$ means nearest neighbors with coupling $t = 2.8\,\text{eV}$. The $|\phi_i^{A/B}\rangle$ are the p_z orbitals of the carbon atoms on sublattice A and B, respectively. In order to solve the Schrödinger equation, we make the ansatz

$$|\psi\rangle = \sum_j e^{i\boldsymbol{k}\cdot\boldsymbol{R}_j} \left(a\,|\phi_j^A\rangle + b\,|\phi_j^B\rangle\right) \tag{5.25}$$

---

[5]The first known illustration of a pencil dates back to a book by C. Gesner published in 1566 [70, 144].
[6]The Web of Science database lists almost 40 000 publications on graphene since 2004.
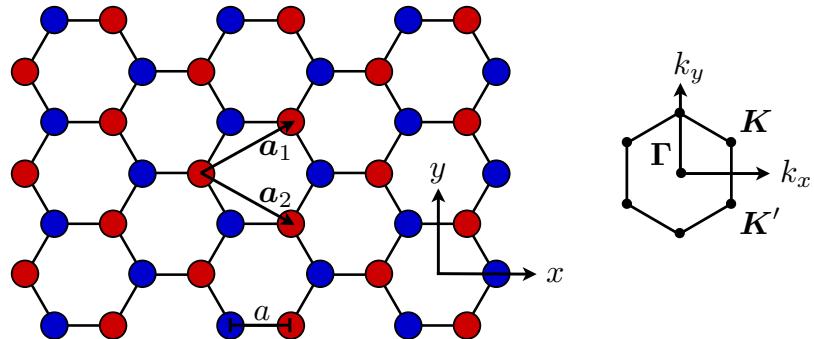
Figure 5.15: Left: Graphene is a two-dimensional honeycomb lattice of carbon atoms. It can be described by a triangular lattice with a basis of two carbon atoms, as indicated by the red and blue dots. The lattice vectors are $\boldsymbol{a}_1$ and $\boldsymbol{a}_2$. The carbon atoms are coupled to their nearest neighbors at a distance of $a = 0.142\,\mathrm{nm}$ by bonds of strength $t = 2.8\,\mathrm{eV}$. Right: The first Brillouin zone of graphene is also hexagonal. The physics of (neutral) graphene takes place close to the $\boldsymbol{K}$ and $\boldsymbol{K}'$ points at the corners of the Brillouin zone.

and obtain by multiplying with $\langle \phi_m^{A/B}|$ from left a linear equation system for the unknown coefficients a and b

$$\epsilon(\boldsymbol{k}) \begin{pmatrix} a \\ b \end{pmatrix} = \begin{pmatrix} 0 & h(\boldsymbol{k}) \\ h^*(\boldsymbol{k}) & 0 \end{pmatrix} \begin{pmatrix} a \\ b \end{pmatrix}, \tag{5.26}$$

where

$$h(\boldsymbol{k}) = -t\,\mathrm{e}^{3\mathrm{i}k_x a}\left[1 + 2\mathrm{e}^{-\mathrm{i}3k_x a/2}\cos\!\left(\sqrt{3}k_y a/2\right)\right]. \tag{5.27}$$

Using the condition that the coefficient determinant of (5.26) has to vanish, we obtain for the eigenenergies

$$\epsilon(\boldsymbol{k}) = \pm t\left[3 + 4\cos\!\left(\frac{3k_x a}{2}\right)\cos\!\left(\frac{\sqrt{3}k_y a}{2}\right) + 2\cos\!\left(\sqrt{3}k_y a\right)\right]^{1/2}. \tag{5.28}$$

The band structure of graphene, reported first in 1947 by Wallace [186], is shown in Figure 5.16. As in neutral graphene every p_z orbital is occupied with a single electron, the lower band is completely occupied, while the upper band is empty. Thus, the Fermi energy is in between the two bands, i.e. $\mu = 0$. At the Fermi energy the bands show minima, or *valleys*, which are located at the corners of the Brillouin zone. Only two valleys at the *Dirac points*

$$\boldsymbol{K} = \frac{2\pi}{3a}\left(1, \frac{1}{\sqrt{3}}\right), \qquad \boldsymbol{K}' = \frac{2\pi}{3a}\left(1, -\frac{1}{\sqrt{3}}\right) \tag{5.29}$$

are relevant, because the others can be transformed into the Dirac points by adding a reciprocal lattice vector. As the physics of graphene takes place near the Dirac points, we perform a Taylor expansion of (5.27) around $\boldsymbol{K}$ and $\boldsymbol{K}'$

$$h(\boldsymbol{k}) \approx -\hbar v_F\left(\mathrm{i}q_x \pm q_y\right), \tag{5.30}$$

to obtain the Hamiltonian[7]

$$H_{\boldsymbol{K}} = \hbar v_F \begin{pmatrix} 0 & q_x - iq_y \\ q_x + iq_y & 0 \end{pmatrix}, \qquad H_{\boldsymbol{K}'} = \hbar v_F \begin{pmatrix} 0 & q_x + iq_y \\ q_x - iq_y & 0 \end{pmatrix}, \qquad (5.32)$$

where

$$v_F \equiv \frac{3at}{2\hbar} \approx 10^6 \, \text{m/s} \qquad (5.33)$$

is the Fermi velocity and $\boldsymbol{q}$ the relative momentum. As this Hamiltonian has the form of the Dirac Hamiltonian, the electrons in graphene behave as relativistic massless fermions, apart from the fact that their velocity v_F is approximately 300 times smaller than the speed of light. The linear dispersion relation of the Dirac Hamiltonian

$$\epsilon(\boldsymbol{q}) = \hbar v_F \, |\boldsymbol{q}| \qquad (5.34)$$

can be clearly seen in Figure 5.16. Note that in addition to the real spin, we can assign to the electrons in graphene two *pseudospins*. The valley pseudospin, because two points $\boldsymbol{K}$ and $\boldsymbol{K}'$ in momentum space have to be taken into account, as well as the lattice pseudospin, because we have to deal with two sublattices. The linear dispersion and the presence of pseudospins result in many exceptional properties, which make graphene so interesting.
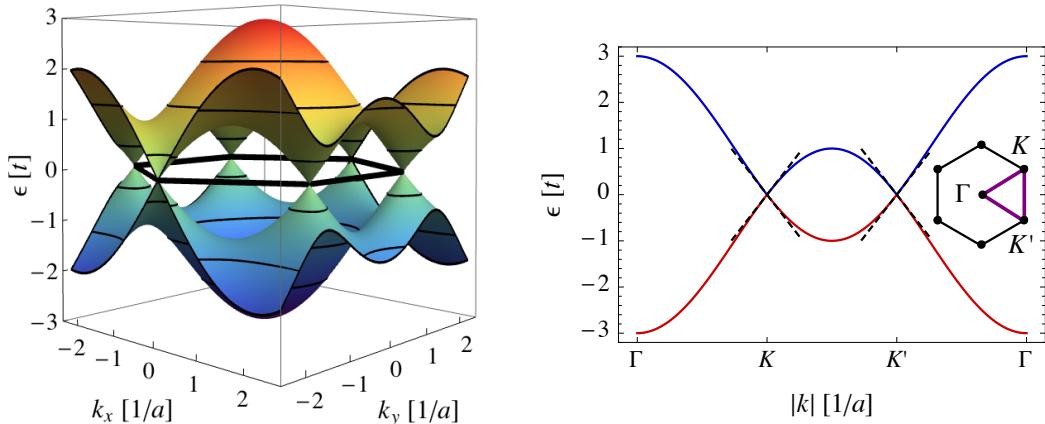
Figure 5.16: Left: Band structure of graphene (5.28). The first Brillouin zone is sketched by black lines. At the Fermi energy of neutral graphene $\mu = 0$, the energy bands show minima, or valleys, which are located at the corners of the Brillouin zone, also called Dirac points. Close to the Dirac points the dispersion has a conical shape. Right: Dispersion relation along straight lines between $\boldsymbol{\Gamma}$, $\boldsymbol{K}$, and $\boldsymbol{K}'$, see the inset. The linear dispersion (5.34) close to the Dirac points is indicated by dashed lines.

---

[7]In order to get the Hamiltonian in its most common notation, see e.g. [31, 67, 100, 200], we also applied a unitary transformation with

$$U = \begin{pmatrix} 1 & 0 \\ 0 & i \end{pmatrix}. \qquad (5.31)$$

In the following, we return to natural units and measure energies in multiples of t and lengths in multiples of a. Close to the Dirac points the DOS per unit area can be calculated directly from (5.34)

$$D(E) = \int \frac{\mathrm{d}^2 q}{4\pi^2} \, \delta\left(E - \epsilon(\boldsymbol{q})\right) = \frac{8\,|E|}{9\pi}, \tag{5.35}$$

where we took into account that each unit cell contains two carbon atoms and assumed degeneracy of the real spin. An analytic expression for the DOS per unit area can also be derived for the entire band structure of graphene [86]

$$D(E) = \frac{8\,|E|}{3\sqrt{3z_\beta}\,\pi^2} \, \mathcal{K}\left(\frac{z_\alpha}{z_\beta}\right) \, \theta\left(1 - |E|/3\right) \tag{5.36}$$

where

$$z_{\alpha/\beta} = \begin{cases} \frac{1}{4}\left(3 - |E|\right)\left(1 + |E|\right)^3 & \text{for } \begin{cases} \alpha: \; 1 < |E| < 3 \\ \beta: \; |E| < 1 \end{cases} \\ 4\,|E| & \text{else} \end{cases} \tag{5.37}$$

Note that $\mathcal{K}$, the complete elliptic integral of first kind, appeared also in the DOS of a tight-binding square grid, see (3.10). In Figure 5.18, we compare these analytical results with the DOS in graphene nanoribbons studied numerically by the NEGF method.

5.3.2 Effect of a magnetic field

Let us study the effect of a homogeneous magnetic field $\boldsymbol{B} = -B\boldsymbol{e}_z$ on graphene's relativistic 2DEG. The Dirac Hamiltonian (5.32) at the $\boldsymbol{K}$ valley is transformed from momentum space into real space by replacing $\hbar\boldsymbol{q} \to \boldsymbol{p} - e\boldsymbol{A}$, where $\boldsymbol{A} = By\boldsymbol{e}_x$ is the vector potential of the magnetic field. To solve the Dirac equation, we insert the two linear equations into each other, keeping in mind that $[p_x, p_y] = -\mathrm{i}eB\hbar$, and obtain for sublattice B the quadratic equation

$$\epsilon^2 \psi_B = v_F^2 \left[(p_x - eBy)^2 + p_y^2 - eB\hbar\right] \psi_B. \tag{5.38}$$

By means of the ansatz $\psi_B(\boldsymbol{r}) = \mathrm{e}^{\mathrm{i}kx}\chi(y)$, we obtain the Schrödinger equation of a harmonic oscillator

$$\tilde{\epsilon}\,\chi(y) = \left[\frac{p_y^2}{2m} + \frac{1}{2}m\omega_c^2\left(y - y_k\right)^2\right]\chi(y), \tag{5.39}$$

which is not only shifted by y_k as in the nonrelativistic case, see Section 5.1.2, but also rescaled in energy

$$\tilde{\epsilon} \equiv \frac{\epsilon^2}{2mv_F^2} + \frac{\hbar\omega_c}{2}, \tag{5.40}$$

where $\omega_c = \frac{eB}{m}$, $y_k = \ell_B^2 k$, and $\ell_B^2 = \frac{\hbar}{eB}$. Thus, the eigenenergies of a relativistic 2DEG in a magnetic field are given by

$$\epsilon_\nu = \pm\sqrt{2mv_F^2\,\hbar\omega_c\,\nu}, \qquad \nu \geq 0. \tag{5.41}$$

The eigenstates on sublattice B read $\psi_B(\boldsymbol{r}) = c_\nu\, \mathrm{e}^{\mathrm{i}kx} \mathcal{D}_\nu\left((y - y_k)/\ell_B\right)$, as in the nonrelativistic case (5.11). The eigenstates on sublattice A follow directly from ψ_B, the Dirac equation and the recursion relation $(\partial_y + y)\,\mathcal{D}_\nu(y) = \sqrt{2\nu}\mathcal{D}_{\nu-1}(y)$, see [3]. The solution of the Dirac equation at the $\boldsymbol{K}'$ valley can be obtained easily by interchanging the two sublattices, see (5.32). The eigenenergy spectrum is unchanged and hence, twofold degenerated. The eigenfunctions of a relativistic 2DEG in a magnetic field are given by

$$\psi_{\boldsymbol{K}}(\boldsymbol{r}) = c_\nu\, \mathrm{e}^{\mathrm{i}kx} \begin{pmatrix} \mp\mathcal{D}_{\nu-1}(\xi) \\ \mathrm{i}\mathcal{D}_\nu(\xi) \end{pmatrix}, \qquad \psi_{\boldsymbol{K}'}(\boldsymbol{r}) = c_\nu\, \mathrm{e}^{\mathrm{i}kx} \begin{pmatrix} \mathcal{D}_\nu(\xi) \\ \mp\mathrm{i}\mathcal{D}_{\nu-1}(\xi) \end{pmatrix}, \tag{5.42}$$

where $\xi \equiv \left(y - \ell_B^2 k\right)/\ell_B$, the c_ν are normalization constants and the $\mathcal{D}_\nu(\xi)$ are rescaled parabolic cylinder functions (5.12) with $\mathcal{D}_{\nu<0} \equiv 0$. The different signs of the eigenstates correspond to the signs of the eigenenergies. We also applied the unitary transformation (5.31) in order to get the correct phase between the wavefunctions on the sublattices. Equivalently, we can choose for the vector potential $\boldsymbol{A} = -Bx\boldsymbol{e}_y$, to get the eigenstates

$$\psi_{\boldsymbol{K}}(\boldsymbol{r}) = c_\nu\, \mathrm{e}^{\mathrm{i}ky} \begin{pmatrix} \mp\mathrm{i}\mathcal{D}_{\nu-1}(\zeta) \\ \mathrm{i}\mathcal{D}_\nu(\zeta) \end{pmatrix}, \qquad \psi_{\boldsymbol{K}'}(\boldsymbol{r}) = c_\nu\, \mathrm{e}^{\mathrm{i}ky} \begin{pmatrix} \mathcal{D}_\nu(\zeta) \\ \pm\mathcal{D}_{\nu-1}(\zeta), \end{pmatrix}, \tag{5.43}$$

where $\zeta \equiv \left(x + \ell_B^2 k\right)/\ell_B$. We will use both of these equivalent sets of eigenstates to calculate the eigenenergy spectrum of a relativistic 2DEG in vicinity of boundaries. In an infinitely extended system, the condition of normalizable eigenstates limits ν to integer values $n = 0, 1, 2 \dots$. Thus, the linearly increasing DOS (5.35) of a relativistic 2DEG is condensed onto discrete Landau levels. However, in contrast to the nonrelativistic case (5.10), the distance of the Landau levels is no longer increasing linearly with B and independent of n, but changes with $\sqrt{B\,n}$. Moreover, the Landau level to $n = 0$ stays at $E = 0$ for every B. This peculiar electronic structure of graphene in a magnetic field becomes noticeable in the quantum Hall effect, which is discussed in the following Section.

5.4 Magnetotransport along the boundary of graphene nanoribbons

We study in this Section magnetotransport along the boundaries of graphene nanoribbons. We show that the resistance oscillations, reported in the previous Section for a nonrelativistic 2DEG, can also be observed in graphene nanoribbons. Also the effect of the different edge geometries on the magnetotransport is discussed.

5.4.1 System

We consider a graphene nanoribbon with a size of $140\,\mathrm{nm} \times 90\,\mathrm{nm}$, which corresponds approximately to a half million carbon atoms. Metallic contacts with a width of $3\,\mathrm{nm}$ are attached at the edges of the ribbon separated by a distance of $L = 110\,\mathrm{nm}$, see Figure 5.17. The wiring of these contacts is the same as in the case of a nonrelativistic 2DEG, see Figure 5.2. Graphene nanoribbons have two elementary edge structures. The ribbon shown to the left of Figure 5.17 has a *zigzag* edge between the contacts S and P_1, whereas the ribbon to the right has an *armchair* edge between these contacts. In rectangular ribbons

zigzag and armchair edges appear perpendicular to each other. Other edge reconstructions are also possible in graphene, see e.g. [54, 83, 91], but are not considered here. The Fermi energy is set to $\mu = 0.06t = 168\,\text{meV}$. For simplicity, we do not consider the Zeeman spin splitting, see remarks in Section 5.4.5. We assume that the influence of the temperature is negligible and thus, set it to zero. Diffusive walls are used at those boundaries, which are not important for the focusing experiment, see the dashed walls in Figure 5.17.
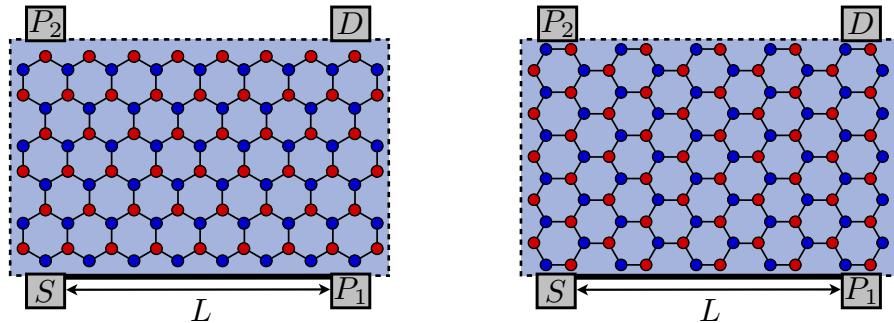

Figure 5.17: Graphene nanoribbons studied in this Section. Both ribbons have a size of $140\,\text{nm} \times 90\,\text{nm}$. Metallic contacts with a width of $3\,\text{nm}$ are attached at the boundaries separated by a distance of $L = 110\,\text{nm}$. The wiring of the contacts is the same as in Figure 5.2. The Fermi energy is set to $\mu = 0.06t = 168\,\text{meV}$. The ribbon to the left has a zigzag edge in between the contacts S and P_1, whereas the ribbon to the right has an armchair edge in between these contacts. Note that at a zigzag edge carbon atoms of only one sublattice appear, while atoms from both sublattices are located at an armchair edge.

The average DOS of the studied graphene nanoribbons, calculated numerically by the NEGF method, is shown in Figure 5.18. As expected, the DOS of the zigzag ribbon (blue curve) and the armchair ribbon (red curve) are nearly identical, and agree well with the DOS of the graphene lattice (5.36) indicated by the black curve. In the region close to the Dirac points $E = 0$, which is shown enlarged on the right side of Figure 5.18, the DOS is increasing linearly in almost perfect agreement with the DOS (5.35) from the Dirac Hamiltonian (green curve). However, the zigzag ribbon shows a distinct peak at $E = 0$, which cannot be observed in the case of an armchair ribbon. This peak can be attributed to a state on the surface of the ribbon, which is dispersionless and hence, does not contribute to electron transport.[8] A surface state is possible at a zigzag edge, because only carbon atoms of a single sublattice appear there. Thus, at the edge the wave function has to vanish only on one sublattice, while the surface state resides on the other sublattice. At an armchair edge atoms from both sublattices appear and a surface state is not possible, see [31, 83, 128, 185] for details. However, in Figure 5.18 the DOS of the armchair ribbon is also nonzero at $E = 0$. These are states induced by the contacts [73], which contribute to the observed finite conductivity of graphene at the Dirac points [35, 130, 131, 172, 198]. As a consequence of this, the carrier densities in the zigzag ribbon $n_{\text{zz}} = 3.7 \cdot 10^{12}\,\text{cm}^{-2}$ and the armchair ribbon $n_{\text{ac}} = 3.3 \cdot 10^{12}\,\text{cm}^{-2}$ are slightly higher than expected from the linear DOS of the Dirac Hamiltonian $n_{\text{di}} = 2.5 \cdot 10^{12}\,\text{cm}^{-2}$. Note that Figure 5.18 also

---

[8]We refer to this state as a *surface state* in order to distinguish it from the edge states, which are also localized close to surface but current carrying. However, the naming is not consistent in the literature.

shows that the electrons in graphene can behave as a nonrelativistic 2DEG, if the Fermi energy is shifted to the band edges $E = \pm 3$. In theoretical studies this is feasible, but to our knowledge this is impossible in the experiment.
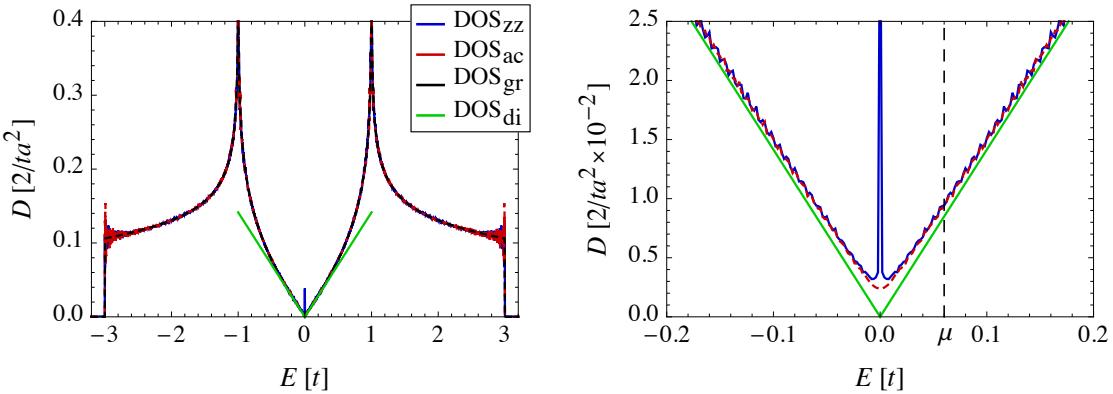
Figure 5.18: Average DOS in the studied graphene nanoribbons. The left figure covers the complete energy band, whereas the right figure shows the region close to the Dirac points at $E = 0$. The blue curve gives the DOS in the zigzag ribbon, while the red curve gives the DOS in the armchair ribbon, see Figure 5.17. The DOS of both ribbons agrees almost perfectly with the DOS of the graphene lattice (5.36) (black curve) and the DOS from the Dirac Hamiltonian (5.35) (green curve). The peak in the DOS of the zigzag ribbon at $E = 0$ is caused by a dispersionless surface state, which does not exist in armchair ribbons. However, also the armchair ribbon has a nonzero DOS at $E = 0$, because of contact induced states. The dashed vertical line indicates the Fermi energy.

5.4.2 Electron focusing, resistance oscillations and the quantum Hall effect

As in the case of a nonrelativistic 2DEG, see Section 5.2, electrons are injected at the contact S and focused onto the contact P_1 by a perpendicular magnetic field B. The focusing spectrum, defined as the generalized 4-point Hall resistance R_{xy} as a function of B, is shown in Figure 5.19 for the zigzag ribbon (left) and the armchair ribbon (right). The blue curve gives the focusing spectrum in the case of specular reflections in between S and P_1, whereas for the red curve the scattering at this boundary is diffusive. First focusing experiments in graphene have been reported recently [174].

At first sight, the focusing spectra of the graphene nanoribbons look very similar to the focusing spectrum of a nonrelativistic 2DEG, compare with Figure 5.4. They start with equidistant peaks located approximately at

$$B_n = \frac{2\mu}{ev_F L} n, \qquad n = 1, 2, 3, \ldots, \tag{5.44}$$

see the dashed vertical lines. At these magnetic fields a multiple n of the cyclotron diameter $2 |\boldsymbol{p}| /eB$ equals the distance L between injector and collector. Note that (5.44) differs from the nonrelativistic case (5.16), because of different dispersion relations, but the essential physics remains the same. Cyclotron orbits can be clearly seen in Figure 5.20, which

shows the local current and the LDOS of electrons originating from S with energy μ. Note that the shown local current and the LDOS have been averaged over the honeycomb cells. In a strong magnetic field $B > 13\,\mathrm{T}$, we observe anomalous resistance oscillations, which cannot be explained by classical cyclotron orbits. When the boundary scattering is diffusive or when the direction of the magnetic field is reversed, the quantum Hall staircase can be observed clearly. The current is carried through edge channels along the boundaries, see Figure 5.21. However, at second sight, we find some striking differences to the nonrelativistic case, compare with Figure 5.4 and Figure 5.7. The hight of the quantum Hall plateaus differs as well as the shape of the edge channels. Moreover, we observe that a substantial current flows at an armchair edge, which is not present at a zigzag edge. In order to understand this behavior, we solve in the following Section the Dirac equation of a bounded relativistic 2DEG under the effect of a magnetic field. We also discuss the observed slight displacement of the classical focusing peaks in the armchair ribbon and show that in graphene all resistance oscillations can be explained by the interference of the occupied edge channels.
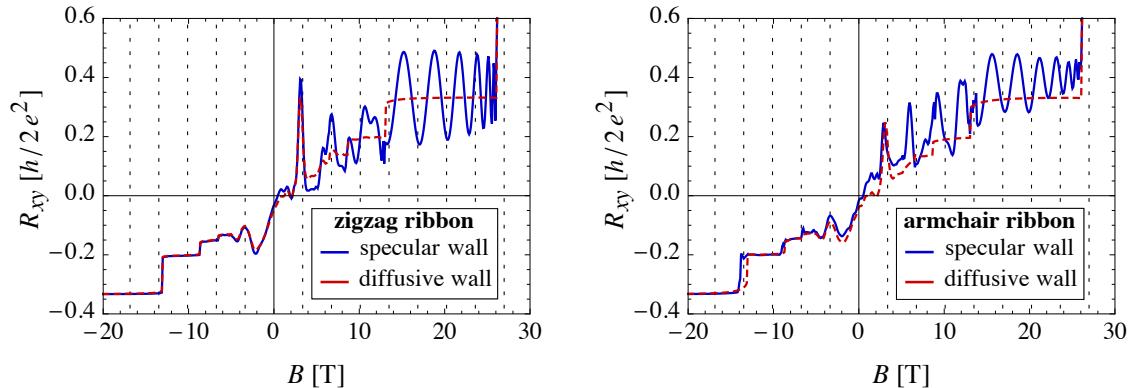
Figure 5.19: Generalized 4-point Hall resistance R_{xy} as a function of the perpendicular magnetic field B for the zigzag ribbon (left) and the armchair ribbon (right). The blue curve gives R_{xy} in the case of specular reflections at the boundary in between S and P_1, whereas for the red curve the scattering at this boundary is diffusive. The focusing spectra start with peaks, which can be understood by classical cyclotron orbits (5.44), see the dashed vertical lines. In a strong magnetic field $B > 13\,\mathrm{T}$, we observe superimposed upon the quantum Hall plateaus anomalous resistance oscillation, which cannot be explained by cyclotron orbits. As in the nonrelativistic case, all resistance oscillations can be explained by the interference of the occupied edge channels.
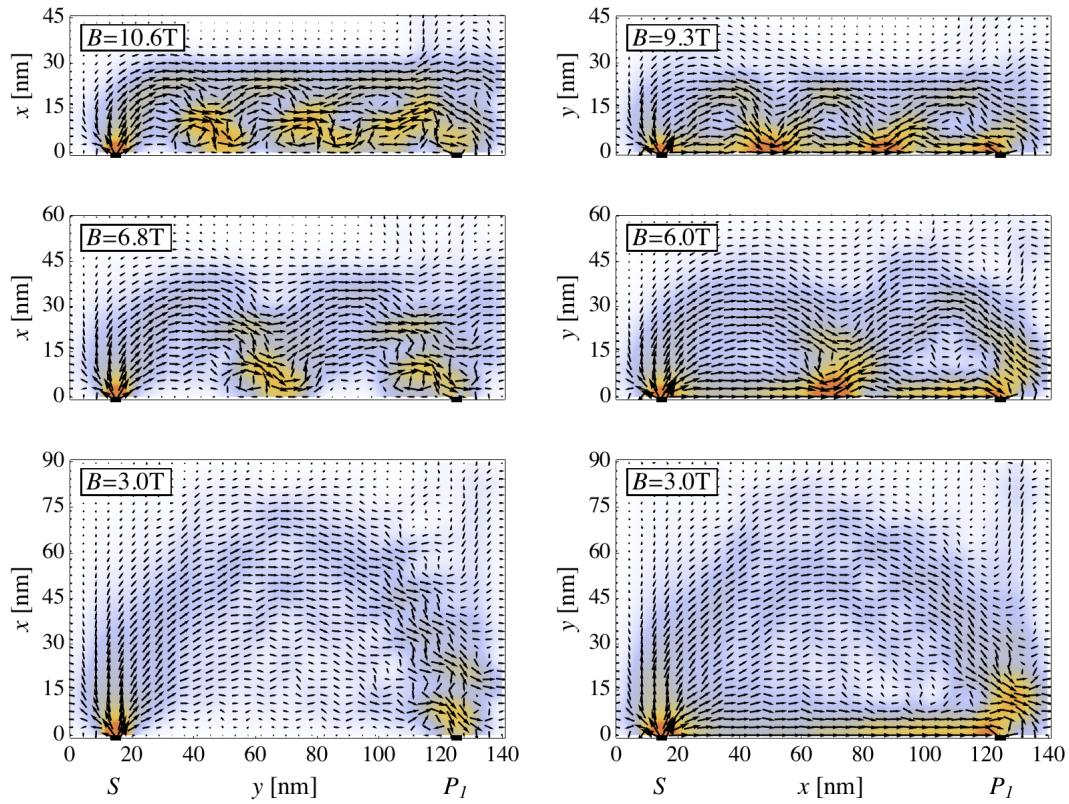
Figure 5.20: Local current (arrows) and LDOS (shading) of electrons originating from S with energy μ. In the zigzag ribbon (left column) and the armchair ribbon (right column) cyclotron orbits can be clearly seen. At the armchair edge a distinct edge current can be observed, which is not present at the zigzag edge. Note that the shown local current and the LDOS have been averaged over the honeycomb cells.
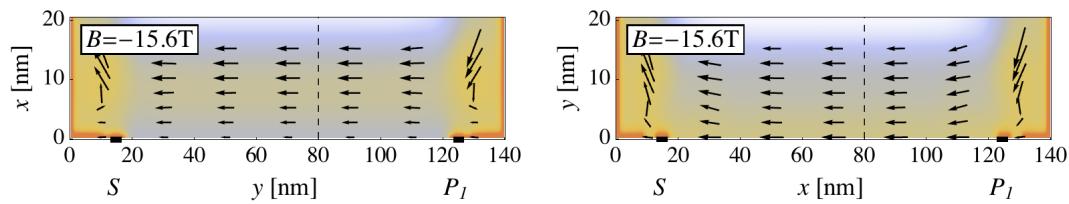
Figure 5.21: The edge channel transport of the quantum Hall effect can be observed clearly, when the direction of the magnetic field is reversed. A finite current flows at the armchair edge (right), whereas the current vanishes at the zigzag edge (left). This can also be seen in the transverse current through the dashed vertical line in Figure 5.24. In the LDOS only a single broadened edge channel can be recognized, instead of spatially separated edge channels as in the nonrelativistic 2DEG, see Figure 5.7 (top).

5.4.3 Graphene ribbons in a magnetic field: Dirac equation

To understand the magnetotransport in graphene nanoribbons, we solve the Dirac equation of a relativistic 2DEG bounded by an edge under the effect of a magnetic field. In general, the solution of the Dirac equation is given by a linear combination of the solutions at both valleys

$$\Psi(\boldsymbol{r}) = c_1 \, \mathrm{e}^{\mathrm{i}\boldsymbol{K}\cdot\boldsymbol{r}} \psi_{\boldsymbol{K}}(\boldsymbol{r}) + c_2 \, \mathrm{e}^{\mathrm{i}\boldsymbol{K}'\cdot\boldsymbol{r}} \psi_{\boldsymbol{K}'}(\boldsymbol{r}), \tag{5.45}$$

where c_1 and c_2 are complex constants. At the zigzag edge, we obtain by means of (5.43)[9]

$$\Psi_{\mathrm{zz}}(\boldsymbol{r}) = \mathrm{e}^{\mathrm{i}\left(\frac{2\pi}{3}x+ky\right)} \left[c_1 \, \mathrm{e}^{\mathrm{i}\frac{2\pi}{3\sqrt{3}}y} \begin{pmatrix} \mp\mathrm{i}\mathcal{D}_{\nu-1}(\zeta) \\ \mathrm{i}\mathcal{D}_{\nu}(\zeta) \end{pmatrix} + c_2 \, \mathrm{e}^{-\mathrm{i}\frac{2\pi}{3\sqrt{3}}y} \begin{pmatrix} \mathcal{D}_{\nu}(\zeta) \\ \pm\mathcal{D}_{\nu-1}(\zeta) \end{pmatrix} \right], \tag{5.46}$$

where $\zeta = \left(x + \ell_B^2 k\right)/\ell_B$. As at a zigzag edge only carbon atoms of one sublattice appear, see Figure 5.17, the wave function has to vanish only on one of the two sublattices. The condition $\Psi_A(x=0) = 0$ leads to the two solutions

$$c_1 = 1, \; c_2 = 0 : \quad \mathcal{D}_{\nu-1}(\ell_B k) \overset{!}{=} 0, \tag{5.47a}$$

$$c_1 = 0, \; c_2 = 1 : \quad \mathcal{D}_{\nu}(\ell_B k) \overset{!}{=} 0. \tag{5.47b}$$

Thus, for given $\ell_B k = \sqrt{\hbar k^2/eB}$ the index ν is determined by the zeros of the rescaled parabolic cylinder functions. The first set of solutions is located at the $\boldsymbol{K}$ valley, whereas the second set is located at the $\boldsymbol{K}'$ valley. The resulting energy bands (5.41) are depicted in Figure 5.22 (left). At large k the discrete Landau levels for integer values of $\nu = n$ can be observed. The distance of these Landau levels decreases with $\sqrt{n}$. When the edge is approached by decreasing k, the energy bands are bent upwards and their degeneracy is lifted. Also the dispersionless surface state $E_{\nu=0} = 0$ at the $\boldsymbol{K}$ valley can be seen. The occupied edge states at the Fermi energy (dashed horizontal line) are indicated by dots.

At an armchair edge, we obtain by means of (5.42)

$$\Psi_{\mathrm{ac}}(\boldsymbol{r}) = \mathrm{e}^{\mathrm{i}\left(\frac{2\pi}{3}+k\right)x} \left[c_1 \, \mathrm{e}^{\mathrm{i}\frac{2\pi}{3\sqrt{3}}y} \begin{pmatrix} \mp\mathcal{D}_{\nu-1}(\xi) \\ \mathrm{i}\mathcal{D}_{\nu}(\xi) \end{pmatrix} + c_2 \, \mathrm{e}^{-\mathrm{i}\frac{2\pi}{3\sqrt{3}}y} \begin{pmatrix} \mathcal{D}_{\nu}(\xi) \\ \mp\mathrm{i}\mathcal{D}_{\nu-1}(\xi) \end{pmatrix} \right], \tag{5.48}$$

where $\xi = \left(y - \ell_B^2 k\right)/\ell_B$. As at armchair edges both sublattices appear, see Figure 5.17, the wave function has to vanish on both of them. The condition $\Psi_A(y = 0) = \Psi_B(y = 0) = 0$ requieres that the coefficient determinant of the linear equation system for c_1 and c_2 vanishes

$$\mathcal{D}_{\nu-1}(-\ell_B k) \mp \mathcal{D}_{\nu}(-\ell_B k) = 0 \tag{5.49}$$

and leads to the solutions

$$c_1 = 1, \quad c_2 = \pm 1. \tag{5.50}$$

Thus, at an armchair edge both valleys are intermixed. The two eigenenergy bands in Figure 5.22 (right) show not only that their degeneracy is lifted in vicinity of the edge but also shallow valleys, which are not present at a zigzag edge. The solution of the Dirac equation at zigzag and armchair edges in a magnetic field can also be found in [1, 22, 48, 187].

---

[9]Note that the graphene lattice is not rotated. Zigzag boundaries run along the y-axis, whereas armchair edges are oriented along the x-axis, see Figure 5.15.
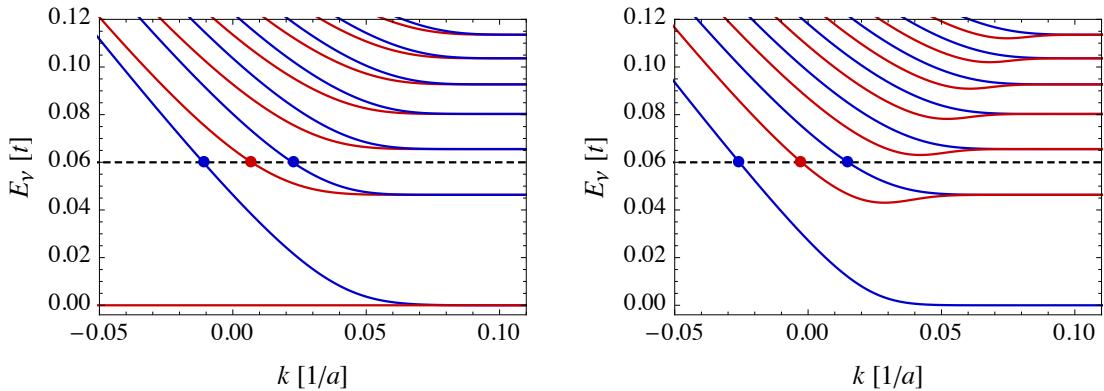
Figure 5.22: Energy bands of graphene bounded by an edge in a magnetic field of $B = 15.6\,\mathrm{T}$. At large k we observe discrete Landau levels. When the edge is approached by decreasing k, the energy bands are bent upwards and their degeneracy is lifted. In the case of a zigzag edge (left) the red curve indicates solutions at the $\boldsymbol{K}$ valley, while the blue curve gives solutions at the $\boldsymbol{K}'$ valley. Also the dispersionless surface state can be seen at the $\boldsymbol{K}$ valley. In the case of an armchair edge (right) the valleys are mixed, which leads to two sets of solutions indicated by the blue and red curve. The occupied edge states at the Fermi energy (dashed horizontal line) are marked by blue and red dots.

5.4.4 Answers to our questions

The quantum Hall effect in graphene can be understood easily by the eigenenergy spectra shown in Figure 5.22. The number of the occupied edge states at the Fermi energy equals $2n + 1$, where n is the Landau level index. As every occupied edge state is a ballistic conductor, which contributes with $2e^2/h$ to the total conductance, the Hall resistance reads

$$R_{xy} = \frac{h}{2e^2} \frac{1}{2n + 1}, \qquad n = 0, 1, 2 \ldots . \tag{5.51}$$

This explains the quantum Hall staircase observed in Figure 5.19, which is one of the definitive fingerprints of a relativistic 2DEG [79, 93, 130, 132, 198], because it differs significantly from the nonrelativistic case. Note that the width of the Hall plateaus is proportional to $1/B$ in both cases. In Figure 5.19 we can also observe that the transitions between the Hall plateaus differ slightly in the two ribbons. This can be explained by the shallow valleys in the band structure at an armchair edge, which are not present at a zigzag edge or when the scattering at all boundaries is diffusive.

The average DOS of the studied ribbons, calculated numerically by the NEGF method, is depicted in Figure 5.23 (blue curve). It has peaks at the positions of the Landau levels (red vertical lines). Note that only the dataset of the zigzag ribbon is shown, because the average DOS of the armchair ribbon is nearly identical. The DOS increases linearly similar to the case of zero magnetic field, see the green curve, which is due to the decreasing distance of the broadened Landau levels. The DOS measured in experiments [11, 112, 122] is similar to our calculations. From Figure 5.23 we can also learn that the gap in between the zeroth and the first Landau level is quite large ($100\,\mathrm{meV}$ at $10\,\mathrm{T}$), which makes it possible to observe the quantum Hall effect in graphene even at room temperature [93, 132].

$$D [2/ta^2]$$

$$E [t]$$
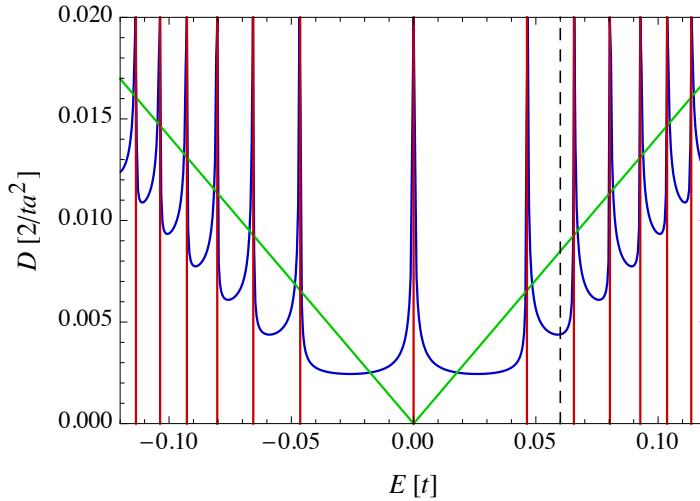
Figure 5.23: Average DOS of the studied graphene nanoribbons (blue curve) at $B = 15.6\,\mathrm{T}$. It has peaks at the positions of the Landau levels (5.41) (red vertical lines), and increases linearly similar to the case of zero magnetic field (5.35) (green curve), because of the decreasing distance of the broadened Landau levels. Note that only the dataset of the zigzag ribbon is shown, because the DOS is almost identical in both ribbons.

In Figure 5.21 we observe that a finite current flows at the armchair edge, whereas the current vanishes at the zigzag edge. This can be seen clearly in Figure 5.24 (blue curve), which shows the transverse current through the dashed vertical lines in Figure 5.21. It can be understood, if we calculate the transverse current by means of the eigenstates of the Dirac equation [100, 101, 126, 187]

$$I_{\mathrm{di}}(\boldsymbol{r}) \propto \sum_{i=1}^{2n+1} \psi_{A,k_i} \psi_{B,k_i} \propto \sum_{i=1}^{2n+1} c_i \, \mathcal{D}_{\nu,k_i} \mathcal{D}_{\nu-1,k_i}, \tag{5.52}$$

where c_i is a normalization constant and the sum is over the occupied edge states, see the dots in Figure 5.22. At zigzag edges the parabolic cylinder functions have to be zero, see (5.47), which results in zero edge current. At armchair edges, the sum of the parabolic cylinder functions has to be zero, see (5.49), which allows for a finite edge current. The transverse current calculated by means of (5.52) agrees well with the Green's functions calculations, see the red curves in Figure 5.24. In the transverse current, we can identify two spatially separated edge channels. Thus, as in the nonrelativistic case, the number of spatially separated edge channels in the local current, averaged over the honeycomb cells, equals the number of occupied Landau levels.[10] The lifting of their degeneracy at the edge is not resolved in the local current. Due to the boundary conditions, in the zigzag ribbon the two edge channels are more densely packed and harder to separate than in the armchair ribbon. Note that the total edge current is approximately independent from the edge geometry. The energy resolved transverse current in Figure 5.25 confirms these findings. Surprisingly, it also shows counterpropagating currents close to the Landau levels,

---

[10]In the case of graphene, the number of occupied Landau levels means the number of Landau levels for which $0 \le E \le \mu$ holds.

see the blue shaded regions, in which the current flows in the opposite direction as in the red shaded regions. These counterpropagating currents are found also in a nonrelativistic 2DEG. At this point, their origin is not understood, but they are also observed by Wang et al. [187] using the eigenstates of the Dirac equation. Also the dependency of the current on the edge geometry is reported in their work. Beyond that, we show in Figure 5.20 that a distinct armchair edge current appears also in the regime of coherent electron focusing.
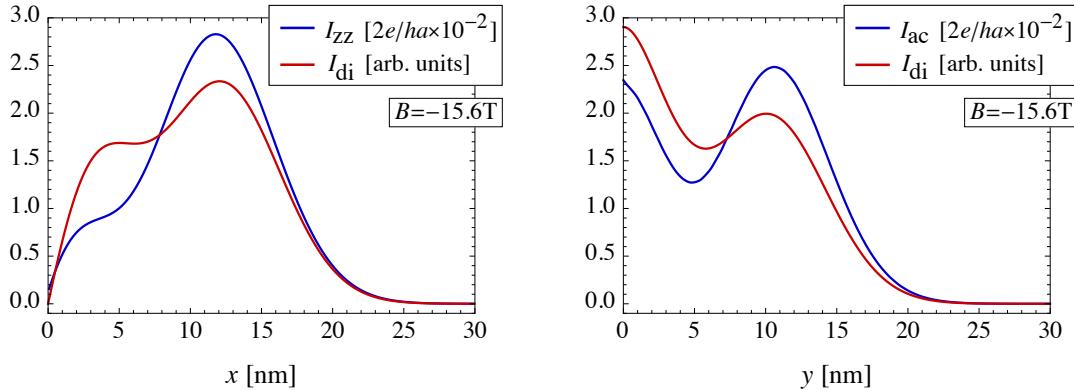
Figure 5.24: Transverse current (blue curves) through the dashed lines in Figure 5.21. A finite current flows at the armchair edge (right), while the current vanishes at the zigzag edge (left). The current, calculated by the eigenstates of the Dirac equation (red curve), agrees with the NEGF calculation and allows to attribute the different edge currents to the different boundary conditions of the ribbons. We can identify two spatially separated edge channels, which equals the number of occupied Landau levels (with $E \geq 0$). Due to the boundary conditions, the edge channels are more densely packed in the zigzag ribbon.
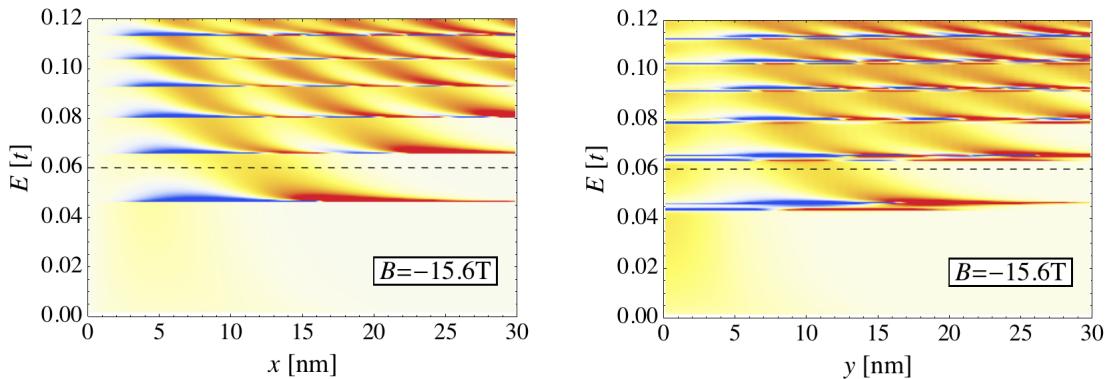
Figure 5.25: Energy resolved transverse current through the dashed lines in Figure 5.21. Warm colors indicate a current from P_1 to S while cold colors correspond to a current in the opposite direction. A distinct current is observed at the armchair edge (right), which is not present at the zigzag edge (left). The number of spatially separated edge channels equals the number of occupied Landau levels (with $E \geq 0$), although the two edge channels closest to a zigzag edge are hardly to separate. Surprisingly, close to the Landau levels regions of counterpropagating current can be observed (blue shaded regions).

The LDOS in Figure 5.21, averaged over the six carbon atoms of the honeycomb cells, shows only a single broadened edge channel. This can be seen clearly in Figure 5.26 (black curves), which gives the LDOS along the dashed vertical line in Figure 5.21. In order to make individual edge channels visible in the LDOS, we have to select only a subset of the carbon atoms, see the blue and red curves for which only the atoms marked in the inset are taken into account. When every carbon atom is considered individually, the LDOS oscillates rapidly between the blue and red curves in Figure 5.26. These oscillations have been reported in several theoretical studies [22, 23, 126, 196], but to our knowledge an experimental confirmation is missing.

The energy resolved LDOS, calculated numerically by means of the NEGF method, is depicted in Figure 5.27. Far from the edge the discrete Landau levels can be observed clearly. If the LDOS is averaged over the honeycomb cells (left column), the bending of the energy bands can be seen only slightly. It becomes more visible, if only a subset of the carbon atoms is taken into account (middle and right column). In this way, we can observe how in the zigzag ribbon (top row) the zeroth Landau level at $E = 0$ splits into a dispersive edge state on the sublattice B (right) and a non-dispersive surface state on the sublattice A (middle). This surface state is not present in the armchair ribbon. Similar results can also be obtained by means of the eigenstates of the Dirac equation, see [1]. Anyway, in the experiment it is not possible to select a subset of the carbon atoms. Thus, the measured LDOS looks similar to the figures in the left column [112].
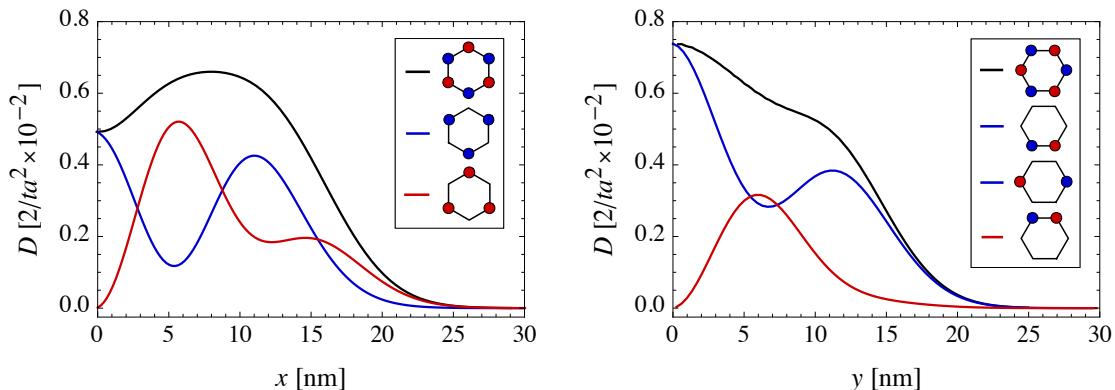
Figure 5.26: LDOS of the zigzag ribbon (left) and the armchair ribbon (right) along the dashed vertical lines in Figure 5.21. The LDOS averaged over the six carbon atoms of the honeycomb cells (black curve) shows a single broadened edge channel. Individual edge channels become visible, when only a subset of the atoms is taken into account, see marked atoms in the legend.

Finally, we explain the resistance oscillations in Figure 5.19 by means of the solution of the Dirac equation. In the zigzag ribbon the edge states are given by (5.46) and (5.47). As in the nonrelativistic case, see Section 5.2.4, we superimpose the plane wave part of the occupied edge states

$$
\left|\psi_{\text{coherent}}^{\text{gr}}\right|^2 = \frac{1}{(2n+1)^2} \left\langle \left| \sum_{i=1}^{n} e^{i\left(k_i + \frac{2\pi}{3\sqrt{3}}\right)L} + \sum_{i=1}^{n+1} e^{i\left(q_i - \frac{2\pi}{3\sqrt{3}}\right)L} \right|^2 \right\rangle_{S,P_1},
\tag{5.53}
$$
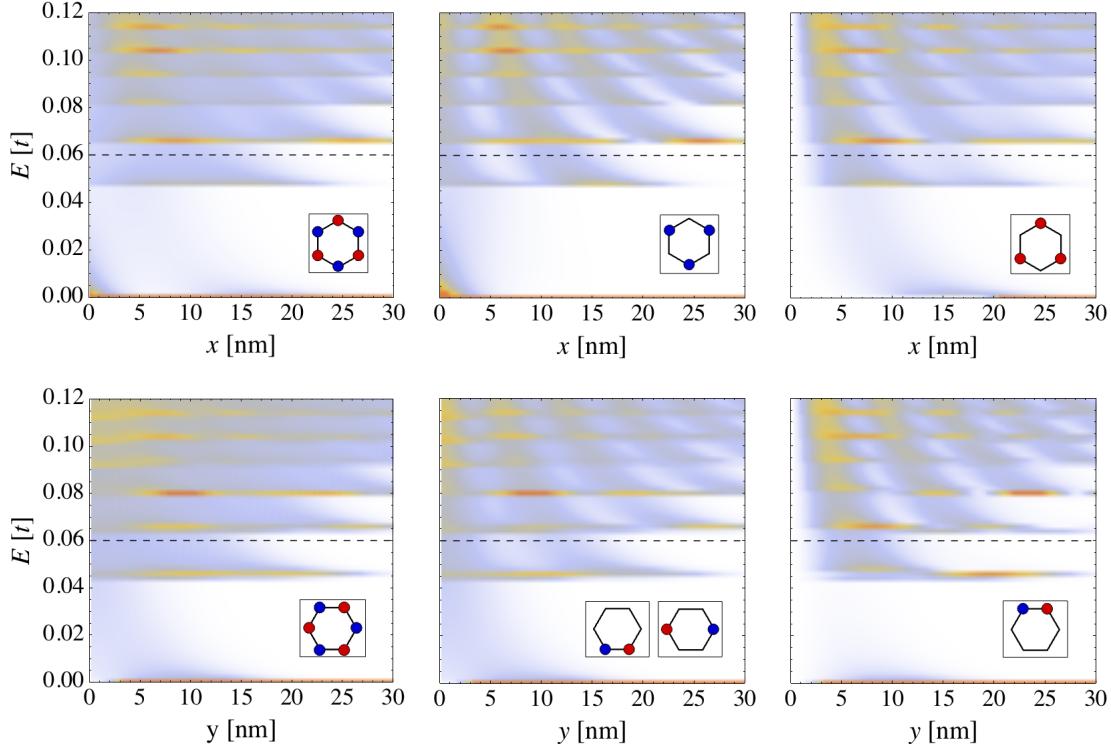
Figure 5.27: Energy resolved LDOS in the studied zigzag ribbon (top row) and armchair
ribbon (bottom row). In the left column the LDOS has been averaged over
the six carbon atoms of the honeycomb cells. Landau levels can be observed
far from the edges. However, the bending of the energy bands in vicinity of
the edge is seen more clearly, when the LDOS is averaged only over a subset
of the atoms (middle and right column). In the zigzag ribbon it can be seen
how the zeroth Landau level splits into an edge state (top, right) and a non-
dispersive surface state (top, middle). This surface state is not present in the
armchair ribbon.

where $\langle \cdot \rangle_{S,P_1}$ means spatial averaging over the finite width of the injector and collector
contacts. The occupied edge states in the $\boldsymbol{K}$ valley are denoted by k_i and the states in the
$\boldsymbol{K}'$ valley by q_i, see the red and blue dots in Figure 5.22. The normalized absolute square
of these superimposed plane waves agrees almost perfectly with the NEGF calculation, see
Figure 5.28 (left). Hence, also in graphene's relativistic 2DEG all focusing peaks can be
understood by the interference of the plane wave part of the occupied edge states. The
anomalous resistance oscillations are beatings, which appear when only some few edge
channels are occupied. In the armchair ribbon, the solution of the Dirac equation is more
complicated, see (5.48), (5.49), and (5.50), because the valleys are intermixed. We found
best agreement to our Green's function calculations, see Figure 5.28 (right), if we use also
for the armchair ribbon (5.53), where the k_i and q_i denote the two sets of solutions. The
beatings, which appear in the case of only two occupied Landau levels, can be used to
determine precisely the distance between the injector S and collector P_1. In Figure 5.28,
the almost perfect match of the positions of all extrema in the range $13\,\mathrm{T} < B < 26\,\mathrm{T}$
is obtained only, if $L = 110\,\mathrm{nm}$ is chosen in (5.53) for the distance between S and P_1.

In order to explain, why in armchair ribbons the classical focusing peaks deviate from their expected positions, see Figure 5.19 (right), we could assume a slightly larger distance $L = 120\,\text{nm}$ between injector and collector. In this case, the classical focusing peaks would appear exactly at the expected positions, but the beatings would absolutely not fit to (5.53). Also finite size effects can be ruled out as these deviations are not present in zigzag ribbons of the same size. One reason for the shift of the classical focusing peaks could be the distinct edge current observed only at armchair edges.
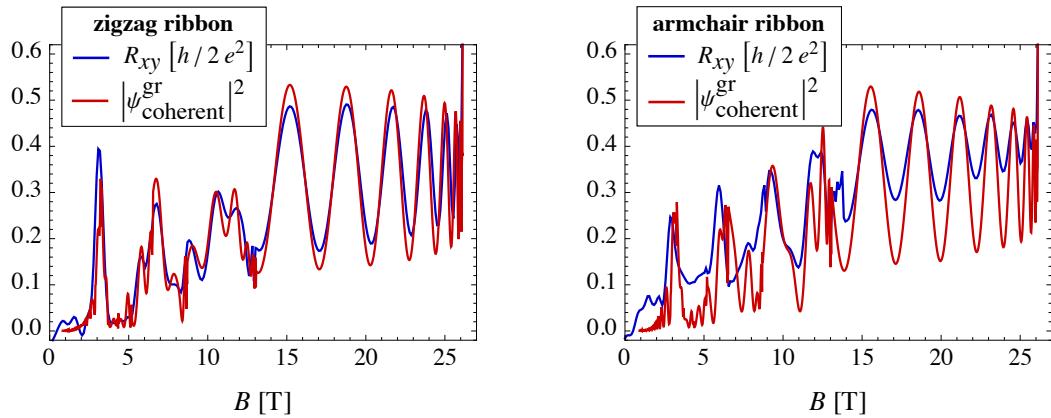
Figure 5.28: Normalized absolute square of the superimposed plane wave part of the occupied edge channels (5.53), (red curve) agrees well with the Green's function calculation of the focusing spectrum (blue curve). Thus, also in graphene's relativistic electron gas all resistance oscillations can be understood by the interference of the edge channels. The anomalous oscillations are beatings, which appear when only some few edge channels are occupied.

5.4.5 Experimental observability

In the preceding Sections, we have studied theoretically magnetotransport in graphene nanoribbons and found anomalous resistance oscillations as well as a distinct effect of the edge shape on the local current flow. However, due to computational limitations, the studied ribbons are relatively small ($L = 110\,\text{nm}$) and the considered magnetic fields are quite strong ($B_{\text{max}} = 30\,\text{T}$). In these strong fields, also the Zeeman spin splitting of the Landau levels can be relevant [78, 93, 197] but we do not expect that the spin splitting changes qualitatively our findings. Although it is technically possible to realize such system parameters, this is not essential to observe our findings in an experiment. As in the nonrelativistic case, the limiting factor is the maximal number of resolvable focusing peaks n_{max}. The distance between injector and collector L as well as the Fermi energy μ have to be tuned in such a way that this number fulfills the rule of thumb

$$n_{\text{max}} \sim \frac{1}{6} \frac{L}{a} \frac{\mu}{t},$$

(5.54)

which can be derived easily by (5.41) and (5.44). The effect of the edge shape on the local current flow could be studied in an experiment by contacting edge channels individually, as in [50, 193].

Because of the excellent agreement of the analytical minimal model (5.53) and the Green's function calculations, see Figure 5.28, we can use this minimal model to study larger ribbons, for which NEGF calculations are demanding. We consider ribbons at which 20 nm wide contacts are attached at a distance of 450 nm. This is approximately the same geometry used in the recent focusing experiment in graphene [174] as well as in a theoretical study [149]. When the Fermi energy is set to $\mu = 260$ meV corresponding to a carrier density of $n_{gr} = 6.0 \cdot 10^{12}$ cm^{-2}, the system is in the regime of classical equidistant focusing peaks ($n_{max} \sim 49$), see Figure 5.29 (right). In agreement to results reported by Rakyta et al. [149], the focusing peaks of higher order ($n > 4$) are clearly visible at armchair edges but are suppressed at zigzag edges. When Fermi energy $\mu = 80$ meV and carrier density $n_{gr} = 5.7 \cdot 10^{11}$ cm^{-2} are lowered, we intermix the regime of coherent electron focusing and the quantum Hall regime ($n_{max} \sim 15$), see Figure 5.29 (left). The focusing spectrum starts with equidistant classical peaks, but anomalous oscillations follow when the strength of the magnetic field is increased. This all gives us confidence that the predicted resistance oscillations can be observed experimentally not only in a nonrelativistic 2DEG but also in graphene.
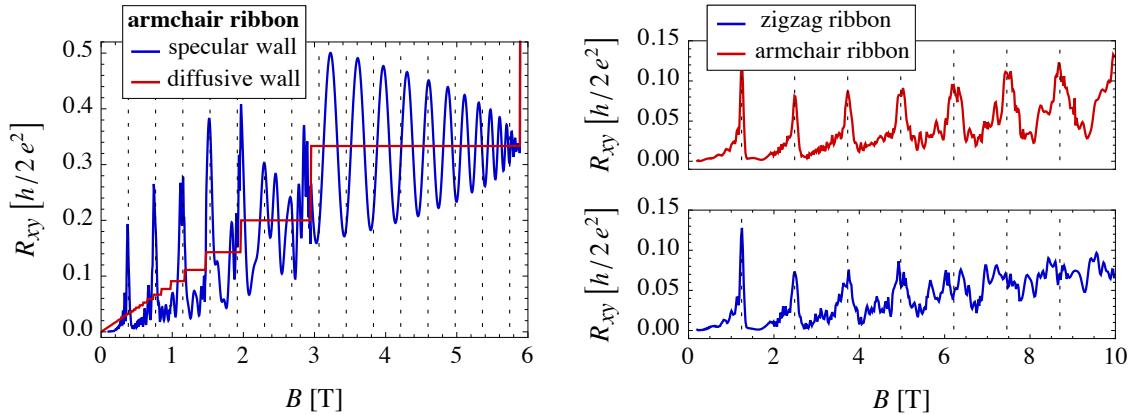
Figure 5.29: Focusing spectra of larger graphene ribbons calculated by means of (5.53). Contacts with a width of 20 nm are attached at a distance of 450 nm. Right: When the Fermi energy is set to $\mu = 260$ meV, corresponding to a carrier density of $n_{gr} = 6.0 \cdot 10^{-12}$ cm^{-2}, only classical equidistant focusing peaks can be observed. As reported in [149], the classical focusing peaks of higher order ($n > 4$) are clearly visible at armchair edges (top) but are suppressed at zigzag edges (bottom). Left: When Fermi energy $\mu = 80$ meV and carrier density $n_{gr} = 5.7 \cdot 10^{-11}$ cm^{-2} are lowered, we find classical equidistant focusing peaks followed by anomalous oscillations.

5.5 Tight-binding lattice in a magnetic field: Hofstadter's butterfly

Finally, in order to discuss the cover picture of this thesis, we study tight-binding lattices in a perpendicular magnetic field $\boldsymbol{B} = -B\boldsymbol{e}_z$ with vector potential $\boldsymbol{A} = By\boldsymbol{e}_x$. Applying the Peierls substitution (2.2), the Hamiltonian of the lattice reads

$$H = \sum_{i=-\infty}^{\infty} \sum_{j=-\infty}^{\infty} |i,j\rangle \langle i,j+1| + \mathrm{e}^{\mathrm{i}2\pi\alpha j} |i,j\rangle \langle i+1,j| + \text{H.c.}, \tag{5.55}$$

where we assumed $\varepsilon = 0$ and $t = 1$ for simplicity. The parameter

$$\alpha = \frac{eBa^2}{h} = \frac{\phi}{\phi_0} = \frac{a^2}{2\pi\ell_B^2} \tag{5.56}$$

gives the number of magnetic flux quanta per unit cell. It can also be written as the ratio of the intersite distance a and the magnetic length $\ell_B = \sqrt{\hbar/eB}$ and determines crucially the properties of the system.[11]

To solve the Schrödinger equation, we make the ansatz $|k,q\rangle = \sum_{l,m} g_m \, \mathrm{e}^{\mathrm{i}(kl+qm)} |l,m\rangle$ and obtain the linear equation system

$$\sum_{i=-\infty}^{\infty} \sum_{j=-\infty}^{\infty} \underbrace{\left[(2\cos(2\pi\alpha j + k) - \epsilon) g_j + \mathrm{e}^{\mathrm{i}q} g_{j+1} + \mathrm{e}^{-\mathrm{i}q} g_{j-1} \right]}_{D_j(\epsilon,\alpha,k,q)} \mathrm{e}^{\mathrm{i}(ki+qj)} |i,j\rangle = 0. \tag{5.57}$$

The eigenenergies ϵ are determined by the condition of a vanishing coefficient determinant

$$\det\big(D(\epsilon,\alpha,k,q)\big) \overset{!}{=} 0. \tag{5.58}$$

In absence of a magnetic field $\alpha = 0$, we can choose $g_j = 1$ and obtain directly the energy bands $\epsilon_0(k,q) = 2\left(\cos(k) + \cos(q)\right)$, discussed already in Section 3.1.2. In presence of a magnetic field, we assume that $\alpha = u/v$ is a rational number. In this case the coefficient matrix is periodic $D_j = D_{j+v}$ and the coefficient determinant is a polynomial of degree v in ϵ. Thus, the energy bands split up in v subbands. For $\alpha = 1/2$, we can choose again $g_j = 1$ and obtain

$$\det \begin{pmatrix} -2\cos(k) - \epsilon & 2\cos(q) \\ 2\cos(q) & 2\cos(k) - \epsilon \end{pmatrix} \overset{!}{=} 0, \tag{5.59}$$

which leads to the two energy bands $\epsilon_{1/2}(k,q) = \pm 2\sqrt{\cos^2(k) + \cos^2(q)}$. Solving (5.58) numerically[12] for rational α, we obtain the eigenenergy spectrum shown in Figure 5.30 (right). This beautiful fractal structure is known as Hofstadter's butterfly [87] due to its characteristic shape and its discoverer D. R. Hofstadter.[13] Note that the zero-measure

---

[11]Note that a nonrelativistic 2DEG can be approximated by a tight-binding Hamiltonian, see (5.13), if $\alpha \ll 1$. However, this constraint does not hold generally.

[12]In order to solve (5.58) numerically, it is useful to take into account that k and q cause only a periodic modulation and hence, we can solve equivalently $|\det(D(\epsilon, u/v, \pi/v, 0))| \le 4$.

[13]Douglas Richard Hofstadter is also author of the famous book "Gödel, Escher, Bach" [88], for which he was awarded with the Pulitzer prize. He is the son of the nobel laureate Robert Hofstadter.

Cantor set of irrational α is irrelevant, because every physical quantity has some uncertainty, which justifies rational α. A finite degree of decoherence may also be present, which smears out the fractal spectrum.

Hofstadter's butterfly can also be studied by means of the NEGF approach. We consider a ribbon of length $N = 40$ and width $M = 20$ with broad contacts attached to all four edges. The resulting average DOS of this system is shown on the cover page and is also given in Figure 5.30 (left) with axis and colorscaling. Note that at the tips of the butterfly (i.e. the corners of the figure) the discrete Landau levels can be seen clearly, compare with Figure 5.10. The advantage of the Green's function method is that we can study easily the effects of the fractal energy spectrum on transport properties of the system. In this way, we observe that Hofstadter's butterfly also settles down in the Hall resistance, see Figure 5.31.

Since the discovery of Hofstadter's butterfly in 1976 [87], it has attracted enormous attention and numerous studies have been performed. However, its experimental observation is still challenging, because in atomic lattices like graphene the required magnetic field strengths are in the order of 10^5 T, which is impossible to realize experimentally. Therefore, superlattices have been studied, which should possess the butterfly at lower magnetic field strengths. However, to our knowledge only fingerprints of the fractal spectrum have been found in superlattices realized in semiconductor heterostructures [8, 68, 158]. The first direct observation of the butterfly has been reported by Kuhl et al. [108] in a microwave experiment. Very recently, the hunt for Hofstadter's butterfly made important progress. The fractal energy spectrum has been observed clearly in superlattices of excellent quality, which can be obtained by placing graphene on hexagonal boron nitride [46, 89, 147].
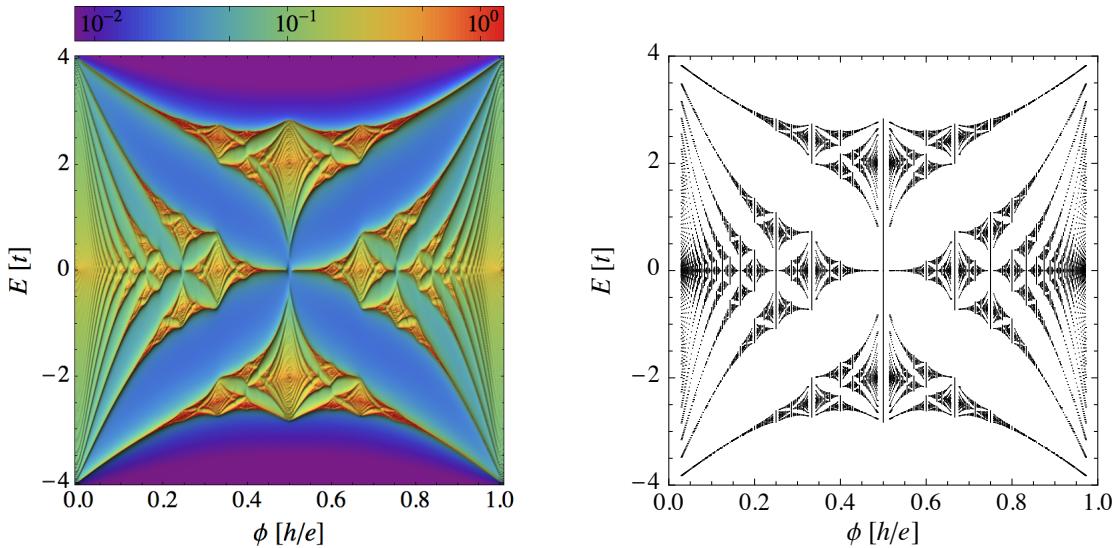
Figure 5.30: Right: Fractal energy spectrum of a tight-binding lattice as a function of the magnetic flux per unit cell and the energy. For the calculation of Hofstadter's butterfly by means of (5.58), we used rational $\alpha = u/v$ with $0 < u, v < 36$. Left: Average DOS (in multiples of $2/ta^2$) in a tight-binding ribbon of size 40×20, calculated numerically by the NEGF approach. This visualization of Hofstadter's butterfly is also shown on the cover page of this thesis.

The Hofstadter Hamiltonian (5.55) has also been realized with ultracold atoms in optical lattices [7, 123], which gives good chances to catch the butterfly also in this system.

5.6 Conclusions

In this Chapter, we have studied magnetotransport in two-dimensional electron systems. After a short introduction to the basic physics of a nonrelativistic two-dimensional electron gas (2DEG), we have studied magnetotransport along the boundary of a finite 2DEG, as it can be realized experimentally in semiconductor heterostuctures. In this system electrons are injected at one point of the boundary and focused by a perpendicular magnetic field on another point of that boundary, see Figure 5.2. We have calculated the 4-point generalized Hall resistance as a function of the magnetic field, see Figure 5.4. In weak fields equidistant focusing peaks appear, which correspond to classical cyclotron orbits (5.16), see Figure 5.5. When the magnetic field strength is increased, anomalous resistance oscillations are observed, which cannot be explained by classical cyclotron motion [169].

In order to understand these anomalous resistance oscillations, we have given an elementary introduction to the quantum Hall effect, which can be observed in the studied system, if the scattering at the boundary in between the injector and collector is diffusive, or if the direction of the magnetic field is reversed. We have shown in Figure 5.7 (third row) that
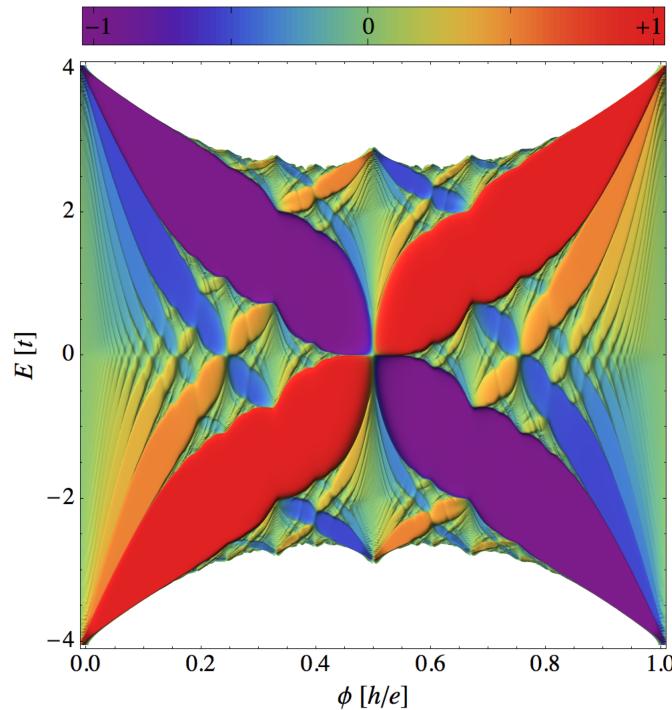
Figure 5.31: Hall resistance R_{xy} of a tight-binding ribbon of size 40×20. Hofstadter's butterfly is also found in this transport quantity. In the wings of the butterfly only a single Landau level is occupied and $R_{xy} = \pm 1$. In the white regions at the top and bottom zero Landau levels are occupied and R_{xy} is infinite.

the discrete Landau levels, on which the DOS of a 2DEG is condensed by the magnetic field, are bent upwards close to the system edge. This behavior can also be obtained within a minimal model, an infinitely extended 2DEG bounded by a single infinite potential wall, see Figure 5.9. The bending of the Landau levels gives rise to edge channels, which carry the current ballistically along the boundary of the system, see Figure 5.7 (first and second row). Backscattering is topologically forbidden, because the group velocity of all edge channels has the same sign, see Figure 5.8. Thus, for the total resistance (5.17), we just have to count the number of edge channels at the Fermi energy, which equals the number of occupied Landau levels.

By means of the minimal model, we have shown that all resistance oscillations can be understood by the interference of the plane wave part of the occupied edge channels, see Figure 5.11. The anomalous resistance oscillations are beatings, which appear when only some few edge channels are occupied and only some few plane waves are superimposed. Thus, the oscillations are very clear and distinct, if only two Landau levels are occupied. In this case the oscillations can also be understood as a new commensurability (5.20) between the magnetic flux enclosed within the two edge channels and the flux quantum. The frequency of the resistance oscillations increases rapidly, when the magnetic field is increased and a Landau level is depleted, because the momentum of the corresponding plane wave is also increasing rapidly, as shown in Figure 5.8. Using the flexibility of the NEGF method, we have studied the robustness of our findings. We have shown in Figure 5.13 that a finite degree of decoherence suppresses the classical focusing peaks even stronger than the anomalous oscillations. We have also demonstrated in Figure 5.14 that the resistance oscillations can be observed, when the boundary scattering is partially diffusive and another contact geometry is used.

In order to observe resistance oscillations, it is necessary that the occupied edge channels can interfere. If the edge chanels are not superimposed coherently (5.19) but incoherently (5.21), the quantum Hall staircase is observed. Thus, mean free path and phase coherence length should be comparable with the distance between injector and collector. As in the experiment the scattering at the boundary is always partially diffusive, we have also given a rule of thumb (5.22) for the required number of specular reflections.

We have also extended our studies to the relativistic 2DEG found in graphene. After a short introduction to the basic physics of graphene, we have studied magnetotransport along the boundary of graphene nanoribbons sketched in Figure 5.17. The generalized Hall resistance of the nanoribbons in Figure 5.19 shows qualitatively the same properties as in the nonrelativistic case, but the details differ. The position of the classical focusing peaks (5.44) changes, because of graphene's linear dispersion relation, but cyclotron orbits can still be observed in the local current, see Figure 5.20. Also the quantum Hall staircase differs. We have shown by a minimal model, an infinitely extended relativistic 2DEG bounded by an edge, that the Hall resistance (5.51) is still determined by the number of occupied edge states. However, this number differs from the nonrelativistic case, because the electronic structure is changed, compare Figures 5.8 and 5.22.

Studying the effect of the edge shape of the graphene ribbons on the magnetotransport, we found that a finite current flows at the armchair edge, whereas the current vanishes at the zigzag edge, see Figures 5.20 and 5.24. By means of the minimal model, the different edge currents can be traced back to the fact that at an armchair edge carbon atoms of both sublattices appear, while at a zigzag edge only atoms of one sublattice are present, see

Figure 5.17. We have also shown in Figure 5.24 that the number of spatially separated edge channels in the local current equals the number of occupied Landau levels (with $E \geq 0$). The discrete Landau levels can be seen clearly in the LDOS in Figure 5.27. However, the bending of the Landau levels in vicinity of the edge as well as spatially separated edge channels can be hardly recognized, if the LDOS is averaged over the six carbon atoms of the honeycomb cells. They can be made visible, if the LDOS is averaged only over a subset of the carbon atoms.

We have shown in Figure 5.28 that also in graphene the resistance oscillations can be understood by superimposing the plane wave part of the occupied edge channels (5.53). Due to computational limitations, the studied graphene ribbons have been relatively small and the magnetic field has been relatively strong. However, due to the good agreement of the minimal model with the NEGF calculations, we have used this minimal model to show that our findings are expected to appear also in larger ribbons at lower magnetic fields. As the resistance oscillations, classical focusing peaks as well as the beatings, are due to the interference of the edge channels, we have also given a rule of thumb (5.54) for the required number of specular reflections.

We have concluded this Chapter with some notes on Hofstadter's butterfly, which is depicted on the cover page of this thesis. Using the NEGF method, we have shown that the butterfly takes place not only in the DOS but also in the Hall resistance, see Figures 5.30 and 5.31.

6 Conclusions and outlook

Quantum transport through nanostructures has been studied in this thesis. In addition to the detailed conclusions given at the end of each Chapter, here we would like to highlight our main results.

We have studied the effects of decoherence on electron transport by means of a novel statistical model. We have demonstrated that homogeneous tight-binding lattices are driven by decoherence from the quantum-ballistic to the classical-Ohmic regime. It has also been shown that the quasi-Fermi level of a ballistic conductor drops entirely at the interfaces to the reservoirs, whereas under the effect of decoherence the linearly decreasing quasi-Fermi level of an Ohmic conductor is found, see Figure 4.14. One main result, mentioned also in the subtitle of this thesis, is the effect of decoherence on Anderson localization. We have shown that Anderson localization can survive up to a critical degree of decoherence, if the decoherence is distributed randomly over the system, see Figure 4.15. In contrast, any finite degree of homogeneously distributed decoherence destroys Anderson localization and leads to Ohmic conduction. We have also discussed how transport in disordered tight-binding lattices can be enhanced by decoherence. Our model has been extended to obtain pure dephasing in one-dimensional systems. In this case of pure phase randomization, only transmission resonances are suppressed but the average transmission is conserved, see Figure 4.24. The critical degree of decoherence, at which randomly distributed decoherence causes an insulator-metal transition in the Anderson model, is independent of whether phase randomization goes along with momentum randomization or not. We have also discussed that our model can be applied to study the effect of spin randomizing and spin conserving decoherence on electron transport in topological insulators.

Another main result, given in the subtitle of this thesis, regards magnetotransport in two-dimensional electron systems. A finite two-dimensional electrons gas (2DEG) is considered, where electrons are injected at one point on the boundary and focused by a perpendicular magnetic field on another point of that boundary, see Figure 5.2. We have studied how the system properties change with the magnetic field. In a weak magnetic field, the generalized 4-point Hall resistance in Figure 5.4 shows equidistant peaks, which can be explained by classical cyclotron motion, see Figure 5.5. When the magnetic field is increased, we find superimposed upon the quantum Hall plateaus anomalous resistance oscillations, which have been identified as beatings due to the interference of the occupied edge states. These resistance oscillations can be observed not only in a nonrelativistic 2DEG, as it can be realized in semiconductor heterostructures, but also in the relativistic 2DEG found in graphene. As we have proven the robustness of our findings, we are confident that these resistance oscillations can be observed experimentally. Studying the local current flow in graphene, we have found a finite current at armchair edges, which is not present at zigzag edges, see Figure 5.20. This edge current can be traced back to the fact that at an armchair edge carbon atoms of both graphene sublattices are present, whereas at a zigzag edge only atoms of one sublattice appear. As to our knowledge, this finite edge current is rarely discussed in the literature, it deserves definitely further studies.

We hope that with this thesis, we have contributed a small part to the knowledge on quantum transport in nanostructures. Nevertheless, research has to be continued further in order to get a comprehensive understanding of the physics at the nanoscale. In this way, we consider to extend our model to a finite energy window, which requieres to take into account at the decoherence regions not only phase randomization but also energy dissipation. By means of this model, we plan to study how a local nonequilibrium energy distribution function evolves in space and time to a Fermi distribution. Moreover, the extension of our model to phonon transport is in preparation, which will allow us to study the effects of decoherence on heat flow in nanosystems.

A Appendix

A.1 Dyson's equation

We consider a system for which the Hamiltonian

$$H = H_0 + V \tag{A.1}$$

is composed of an unperturbed Hamiltonian H_0 and a perturbation V. When the Green's function of the unperturbed system is known

$$g = (E + \mathrm{i}\nu - H_0)^{-1}, \tag{A.2}$$

we can write for the (inverse) Green's function of the perturbed system

$$G^{-1} = E + \mathrm{i}\nu - H = g^{-1} - V. \tag{A.3}$$

By multiplication with G from right and g from left, we obtain *Dyson's equation*

$$G = g + gVG, \tag{A.4}$$

which relates the Green's function of the pertubated to the Green's function of the unperturbed system. Dyson's equation can be very useful for the calculation of Green's function in many situations, see for example Appendix A.2. In particular, it can be used recursively to build up Green's functions in blocks, which allows to save computation time and memory, see e.g. [192] and references therein.

A.2 Surface Green's function of the semi-infinite chain

In this Appendix, we calculate the surface Green's function of the semi-infinite tight-binding chain described by the Hamiltonian (3.11). Our derivation is based on [39, Section 5.3.2] and [201, Section 3.2.1]. In order to apply Dyson's equation, we decompose the chain into an unperturbed system and a perturbation. In the unperturbed system the surface site is decoupled from the rest of the chain and thus, its Green's function fulfills

$$g_{11} = (E - \varepsilon)^{-1}, \quad g_{12} = g_{21} = 0. \tag{A.5}$$

The perturbation is the coupling between the two subsystems

$$V = t\left(|1\rangle\langle 2| + |2\rangle\langle 1|\right), \tag{A.6}$$

which means that only two matrix elements are nonzero $V_{12} = V_{21} = t$, see Figure A.1.

By means of Dyson's equation, we obtain for the Green's function of the chain

$$G_{11} = g_{11} + g_{11}V_{12}G_{21}, \tag{A.7a}$$

$$G_{21} = g_{22}V_{21}G_{11}. \tag{A.7b}$$

Taking into account that $g_{22} = G_{11}$, because after removing the surface site the remaining chain is again semi-infinitely long, we get a quadratic equation

$$t^2 G_{11}^2 - (E - \varepsilon)\, G_{11} + 1 = 0, \tag{A.8}$$

with the solution

$$G_{11} = \frac{E - \varepsilon}{2t^2} \pm \frac{1}{2t^2}\sqrt{(E - \varepsilon)^2 - 4t^2}. \tag{A.9}$$

To lift the ambiguity and to obtain (3.12), we use that $\mathrm{Im}\,(G) < 0$ and that the Green's function is continuous.
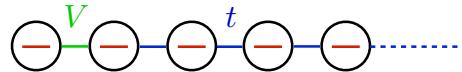
Figure A.1: Semi-infinite tight-binding chain. In order to calculate the surface Green's function by means of Dyson's equation, the chain is decomposed in an unperturbed system and a perturbation. In the unperturbed system the first site and the rest of the chain are decoupled. The perturbation V is the coupling between these subsystems.

A.3 Coherent transport in tight-binding chains: Exact results

In this Appendix, we derive analytically some exact results on the coherent transport in tight-binding chains. We consider a chain of length N described by the Hamiltonian (3.18), which is connected to two reservoirs by the self-energy

$$\Sigma = \nu + \mathrm{i}\eta \tag{A.10}$$

acting on the first and last site of the chain. This self-energy includes both, semi-infinite chains (3.13) as well as wide-band reservoirs (3.17). At first, we show how the transmission can be calculated recursively. Using this recursion formula, the disorder averaged coherent resistance is then calculated by means of generating functions.

A.3.1 Recursion formula for the transmission

The coherent transmission through the chain is determined by the matrix element G_{1N} of the Green's function, see (3.19). Because of the tridiagonal structure of G^{-1} this matrix element can be calculated recursively, as has been shown in a similar way by M. Zilly et al. [202].

From the identity $G^{-1}G = 1$, we infer that the matrix element G_{1N} is given by the first element of the vector x_j, which is the solution of the linear equation system

$$\sum_j G_{ij}^{-1} x_j = \delta_{iN}. \tag{A.11}$$

We apply a LU decomposition on G^{-1}

$$G^{-1} = \begin{pmatrix} \alpha_1 & -1 & 0 & \cdots & 0 \\ -1 & \alpha_2 & -1 & 0 & \vdots \\ 0 & -1 & \alpha_3 & -1 & \vdots \\ \vdots & & & \ddots & \vdots \\ 0 & \cdots & 0 & -1 & \alpha_N \end{pmatrix} \tag{A.12}$$

$$= \begin{pmatrix} 1 & 0 & 0 & \cdots & 0 \\ l_1 & 1 & 0 & 0 & \vdots \\ 0 & l_2 & 1 & 0 & \vdots \\ \vdots & & & \ddots & \vdots \\ 0 & \cdots & 0 & l_{N-1} & 1 \end{pmatrix} \begin{pmatrix} u_1 & -1 & 0 & \cdots & 0 \\ 0 & u_2 & -1 & 0 & \vdots \\ 0 & 0 & u_3 & -1 & \vdots \\ \vdots & & & \ddots & \vdots \\ 0 & \cdots & 0 & 0 & u_N \end{pmatrix}, \tag{A.13}$$

with

$$\alpha_i = E - \varepsilon_i - \Sigma \left(\delta_{i1} + \delta_{iN} \right), \quad l_i = -\frac{1}{u_i}, \quad u_i = \alpha_i + l_{i-1}, \quad u_1 = \alpha_1. \tag{A.14}$$

The linear equation system (A.11) reads then

$$\sum_{k,j} L_{ik} \underbrace{U_{kj} x_j}_{y_k} = \delta_{iN}. \tag{A.15}$$

From the structure of L and U, we obtain by forward substitution $y_k = \delta_{kN}$ and finally, by backward substitution

$$x_1 = G_{1N} = \prod_{i=1}^{N} \frac{1}{u_i}. \tag{A.16}$$

Using the definition of the u_i, the polynom $P_N \equiv \prod_{i=1}^{N} u_i$ is given by the recursion

$$\begin{aligned} P_N &= \left(E - \varepsilon_N - \Sigma \right) P_{N-1} - P_{N-2}, \\ P_i &= \left(E - \varepsilon_i \right) P_{i-1} - P_{i-2}, \\ P_1 &= E - \varepsilon_1 - \Sigma, \quad P_0 = 1. \end{aligned} \tag{A.17}$$

Finally, we subdivide P_N into its real and imaginary part and obtain for the transmission of the N sites long chain

$$T_N(E) = -4\text{Im} \left(\Sigma \right)^2 |G_{1N}|^2 = \frac{4\eta^2}{|r_N - \Sigma r_{N-1} - \Sigma s_N + \Sigma^2 s_{N-1}|^2} \tag{A.18}$$

with the polynomials

$$\begin{aligned} r_i &= \left(E - \varepsilon_i \right) r_{i-1} - r_{i-2}, & s_i &= \left(E - \varepsilon_i \right) s_{i-1} - s_{i-2}, \\ r_0 &= 1, & s_1 &= 1, \\ r_{-1} &= 0, & s_0 &= 0. \end{aligned} \tag{A.19}$$

A.3.2 Disorder averaged resistance

We calculate analytically the disorder averaged coherent resistance of a tight-binding chain. This proof has been performed by O. Ujsághy and we have published it in [168]. Using a recursive scattering approach, Stone et al. [171] arrived at the same result.

Using the recursion relations (A.18), we obtain for the disorder averaged resistance

$$
\left\langle \frac{1}{T_N} \right\rangle = \int \frac{1}{T_N} \prod_{i=1}^{N} w(\varepsilon_i) \mathrm{d}\varepsilon_i = \frac{1}{4\eta^2} \Big[R_N + 2\left|\Sigma\right|^2 R_{N-1} + \left|\Sigma\right|^4 R_{N-2} - 4\nu S_N
$$
$$
- 4\nu \left|\Sigma\right|^2 S_{N-1} + 4\nu^2 U_N + 2\left|\Sigma\right|^2 \Big], \quad \text{(A.20)}
$$

with

$$
R_N = \left\langle r_N^2 \right\rangle = \int r_N^2 \prod_{i=1}^{N} w(\varepsilon_i) \mathrm{d}\varepsilon_i = \left(E^2 + \sigma^2 \right) R_{N-1} - 2E S_{N-1} + R_{N-2}, \quad \text{(A.21)}
$$

$$
S_N = \left\langle r_N r_{N-1} \right\rangle = \int r_N r_{N-1} \prod_{i=1}^{N} w(\varepsilon_i) \mathrm{d}\varepsilon_i = E R_{N-1} - S_{N-1}, \quad \text{(A.22)}
$$

$$
U_N = \left\langle r_N s_{N-1} \right\rangle = \int r_N s_{N-1} \prod_{i=1}^{N} w(\varepsilon_i) \mathrm{d}\varepsilon_i = E S_{N-1} - U_{N-1} - 1 \quad \text{(A.23)}
$$

and the initial conditions $R_0 = 1, R_{-1} = S_0 = U_1 = 0$.

In order solve this recursion, we calculate the generating functions $F_P(z) = \sum_{N=1}^{\infty} P_N z^{N-1}$ of the polynomials $P \in \{R, S, U\}$ and with these the generating function

$$
F_{\langle \frac{1}{T_N} \rangle}(z) = \sum_{N=1}^{\infty} \left\langle \frac{1}{T_N} \right\rangle z^{N-1} = \frac{1}{\eta^2} \Big[F_R(z) + \left(2\left|\Sigma\right|^2 + z\left|\Sigma\right|^4 \right) \left(1 + z F_R(z) \right)
$$
$$
- 4\nu \left(1 + z\left|\Sigma\right|^2 \right) F_S(z) + 4\nu^2 F_U(z) + \frac{2\left|\Sigma\right|^2}{1-z} \Big]
$$
$$
= \frac{1}{2\left(1-z\right)} - \frac{1}{4\eta^2} \frac{A(z)}{N_1(z)}, \quad \text{(A.24)}
$$

where

$$
A(z) = \Big[1 + \left(2\nu^2 - 1 \right)\left(E^2 - \sigma^2 \right) + 2\left|\Sigma\right|^2 \left(1 - 2\nu E \right) + \left|\Sigma\right|^4 \Big] z
$$
$$
+ \Big[1 - 2\nu^2 + \left|\Sigma\right|^4 \Big] z^2 + \Big[E^2 + \sigma^2 + 2\left|\Sigma\right|^2 - 4\nu E + 2\nu^2 \Big], \quad \text{(A.25)}
$$

$$
N_1(z) = z^3 - \left(E^2 - \sigma^2 - 1 \right) z^2 + \left(E^2 + \sigma^2 - 1 \right) z - 1, \quad \text{(A.26)}
$$

generalizing [202] beyond the wide-band approximation. We perform a partial fraction decomposition of $F_{\langle 1/T_N \rangle}$, or for simplicity rather of

$$
\frac{A(z)}{N_1(z)} = -4\eta^2 \sum_{N=1}^{\infty} \left(\left\langle \frac{1}{T_N} \right\rangle - \frac{1}{2} \right) z^{N-1} = \sum_{k=1}^{3} \frac{\alpha_k}{z - z_k}, \quad \text{(A.27)}
$$

where the z_k are the roots of the polynomial $N_1(z)$, for which Vieta's formulas hold

$$
\begin{aligned}
z_1 + z_2 + z_3 &= E^2 - \sigma^2 - 1, \\
z_1 z_2 + z_1 z_3 + z_2 z_3 &= E^2 + \sigma^2 - 1, \\
z_1 z_2 z_3 &= 1.
\end{aligned}
\tag{A.28}
$$

In the same way, the α_k are determined as

$$
\alpha_k = \frac{A(z_k)}{3z_k^2 - 2z_k\left(E^2 - \sigma^2 - 1\right) + E^2 + \sigma^2 - 1} = \frac{A(z_k)}{N_1'(z_k)}.
\tag{A.29}
$$

Using the formal power-series

$$
\frac{\alpha_k}{z - z_k} = -\frac{\alpha_k}{z_k} \sum_{N=1}^{\infty} \left(\frac{z}{z_k}\right)^{N-1}
\tag{A.30}
$$

in (A.27), we get finally the analytical formula

$$
\left\langle \frac{1}{T_N} \right\rangle = \frac{1}{2} + \frac{1}{4\eta^2} \sum_{k=1}^{3} \frac{\alpha_k}{z_k^N} = \frac{1}{2} + \frac{1}{4\eta^2} \sum_{k=1}^{3} \alpha_k e^{-N \ln(z_k)}.
\tag{A.31}
$$

This is the main result of this Appendix. It gives, together with z_k from (A.28) and α_k from (A.29), the disorder averaged resistance of the coherent tight-binding chain of length N, which is connected at its ends to reservoirs by arbitrary self-energies. To our knowledge such a compact analytical formula, namely a constant plus a sum of three exponential functions, has never been reported before in the literature. In the band-center $E = 0$ the roots are given by

$$
z_{1,2} = -\frac{\sigma^2}{2} \pm \sqrt{\frac{\sigma^4}{4} + 1}, \qquad z_3 = -1,
\tag{A.32}
$$

and (A.31) simplifies to (3.21).

In the following, we discuss possible values of the roots z_k of the polynomial $N_1(z)$, which determine the behavior of the exponential functions in (A.31) and thus, the behavior of the resistance. At first, we note that $N_1(z)$ is independent of the reservoir's self-energy Σ and thus, also its roots are independent of the modeling of the reservoirs [202]. From $N_1(z = 0) = -1$ and $N_1(z = 1) = 2\sigma^2 > 0$, we learn that $N_1(z)$ has at least one single real root in the interval $]0, 1[$, which is denoted by z_1 and leads to the exponential increase of the resistance. More information on the z_k can be gained by the discriminant

$$
\Delta = \sigma^8 - 2\sigma^4\left(E^4 + 10E^2 - 2\right) + E^2\left(E^2 - 4\right)^3.
\tag{A.33}
$$

For $\Delta < 0$, we have the real root z_1 and two complex conjugate roots $z_3 = z_2^*$. From the third Vieta formula we learn that $z_2 z_3 = |z_2|^2 = 1/z_1 > 1$. Therefore, the complex roots cause by their phase an oscillation, which is exponentially suppressed with the chain length. For $\Delta \geq 0$ all three roots are real. Again, we learn from the third Vieta formula $z_2 z_3 = 1/z_1 > 1$. If $z_2, z_3 > 0$, only one of them can be less than 1. However, two roots in the intervall $]0, 1[$ contradict to $N_1(0) = -1$ and $N_1(1) = 2\sigma^2 > 0$, which allows only an odd number of roots in this interval. Therefore both, z_2 and z_3 are larger than 1. If

$z_2, z_3 < 0$, only one of them can be in the interval $]-1, 0[$, which contradicts to $N_1(0) = -1$ and $N_1(-1) = -2E^2 < 0$ allowing only an even number of roots in this interval. Therefore both, z_2 and z_3 are less than -1. In both cases their contributions to the resistance are exponentially suppressed.

To summarize, we have only a single real root z_1 in the interval $]0, 1[$, which dominates the resistance for $N \to \infty$

$$\left\langle \frac{1}{T_N} \right\rangle = \frac{\alpha_1}{4\eta^2} e^{N|\ln(z_1)|}. \tag{A.34}$$

This equation also clarifies that the decoherence induced transition, discussed in Section 4.5, appears also in the case of arbitrary energies E and self-energies Σ.

A.4 Resistivity of disorder and decoherence averaged tight-binding chains

We calculate analytically the resistivity of infinitely long, disordered tight-binding chains under the effect of decoherence (4.10). Using (3.21) and (4.6) we obtain

$$\rho = \sum_{j=1}^{N} \frac{u_j}{N} \left\langle \frac{1}{T_j} \right\rangle \xrightarrow{N \to \infty} \frac{p^2}{2} \sum_{j=1}^{\infty} e^{-(j-1)/\ell} \left[1 + \alpha_+ e^{j/\xi} + \alpha_- e^{-j/\xi} (-1)^j \right]$$

$$= \frac{p^2}{2} \left(\sum_{j=0}^{\infty} e^{-j/\ell} + \alpha_+ e^{1/\xi} \sum_{j=0}^{\infty} \left[e^{1/\xi - 1/\ell} \right]^j - \alpha_- e^{-1/\xi} \sum_{j=0}^{\infty} \left[-e^{-1/\xi - 1/\ell} \right]^j \right). \tag{A.35}$$

While the first and third geometric series converge for any finite degree of decoherence $\ell > 0$, the second geometric series converges only if $\xi > \ell$. In this case by performing the sums we get

$$\rho = \frac{p^2}{2} \left[\frac{1}{1 - e^{-1/\ell}} + \frac{\alpha_+ e^{1/\xi}}{1 - e^{1/\xi - 1/\ell}} - \frac{\alpha_- e^{-1/\xi}}{1 + e^{-1/\xi - 1/\ell}} \right]. \tag{A.36}$$

Substituting (3.23) in (3.22), we can express $\alpha_\pm$ as a function of the disorder σ

$$2\alpha_\pm = 1 \pm \frac{1}{\sqrt{\frac{\sigma^4}{4} + 1}}. \tag{A.37}$$

Using $e^{-1/\ell} = 1 - p$ and $e^{\pm 1/\xi} = \pm \frac{\sigma^2}{2} + \sqrt{\frac{\sigma^4}{4} + 1}$, we obtain after straightforward algebra (4.11). If $\xi < \ell$, from the second series in (A.35) follows directly (4.12).

Bibliography

[1] D. A. Abanin, P. A. Lee, and L. S. Levitov. Charge and spin transport at the quantum Hall edge of graphene. *Solid State Commun.*, 143:77, 2007.

[2] E. Abrahams, P. W. Anderson, D. C. Licciardello, and T. V. Ramakrishnan. Scaling theory of localization: Absence of quantum diffusion in two dimensions. *Phys. Rev. Lett.*, 42:673, 1979.

[3] M. Abramowitz and I. Stegun. *Handbook of Mathematical Functions.* Dover Publications, 1972.

[4] M. Ahlskog, R. Menon, A. J. Heeger, T. Noguchi, and T. Ohnishi. Metal-insulator transition in oriented poly(p-phenylenevinylene). *Phys. Rev. B*, 55:6777, 1997.

[5] A. Ahmadi Fouladi, S. A. Ketabi, S. M. Elahi, and S. A. Sebt. Effects of dephasing on the spin-dependent currents and noise power in a molecular junction. *Eur. Phys. J. B*, 85:1, 2012.

[6] K. E. Aidala, R. E. Parrott, T. Kramer, E. J. Heller, R. M. Westervelt, M. P. Hanson, and A. C. Gossard. Imaging magnetic focusing of coherent electron waves. *Nat. Phys.*, 3:464, 2007.

[7] M. Aidelsburger, M. Atala, M. Lohse, J. T. Barreiro, B. Paredes, and I. Bloch. Realization of the Hofstadter Hamiltonian with ultracold atoms in optical lattices. *Phys. Rev. Lett.*, 111:185301, 2013.

[8] C. Albrecht, J. H. Smet, K. von Klitzing, D. Weiss, V. Umansky, and H. Schweizer. Evidence of Hofstadter's fractal energy spectrum in the quantized Hall conductance. *Phys. Rev. Lett.*, 86:147, 2001.

[9] P. W. Anderson. Absence of diffusion in certain random lattices. *Phys. Rev.*, 109:1492, 1958.

[10] P. W. Anderson, D. J. Thouless, E. Abrahams, and D. S. Fisher. New method for a scaling theory of localization. *Phys. Rev. B*, 22:3519, 1980.

[11] E. Y. Andrei, G. Li, and X. Du. Electronic properties of graphene: A perspective from scanning tunneling microscopy and magnetotransport. *Rep. Prog. Phys.*, 75:056501, 2012.

[12] A. Aspect and M. Inguscio. Anderson localization of ultracold atoms. *Phys. Today*, 62:30, 2009.

[13] P. Avouris. Graphene: Electronic and photonic properties and devices. *Nano Lett.*, 10:4285, 2010.

[14] A. Bachtold, M. S. Fuhrer, S. Plyasunov, M. Forero, E. H. Anderson, A. Zettl, and P. L. McEuen. Scanned probe microscopy of electronic transport in carbon nanotubes. *Phys. Rev. Lett.*, 84:6082, 2000.

[15] A. Bachtold, C. Strunk, J.-P. Salvetat, J.-M. Bonard, L. Forro, T. Nussbaumer, and C. Schonenberger. Aharonov-Bohm oscillations in carbon nanotubes. *Nature*, 397:673, 1999.

[16] S. Bandopadhyay, D. Chaudhuri, and A. M. Jayannavar. A comparative study of two phenomenological models of dephasing in series and parallel resistors. *Phys. Lett. A*, 374:813, 2010.

[17] D. M. Basko, I. L. Aleiner, and B. L. Altshuler. Metal–insulator transition in a weakly interacting many-electron system with localized single-particle states. *Ann. Phys.*, 321:1126, 2006.

[18] C. W. J. Beenakker and H. van Houten. Quantum transport in semiconductor nanostructures. *Solid State Physics*, 44:1, 1991.

[19] Z. Bihary and M. A. Ratner. Dephasing effects in molecular junction conduction: An analytical treatment. *Phys. Rev. B*, 72:115439, 2005.

[20] F. Bloch. Über die Quantenmechanik der Elektronen in Kristallgittern. *Z. Phys.*, 52:555, 1929.

[21] K. I. Bolotin, K. J. Sikes, J. Hone, H. L. Stormer, and P. Kim. Temperature-Dependent transport in suspended graphene. *Phys. Rev. Lett.*, 101:096802, 2008.

[22] L. Brey and H. A. Fertig. Edge states and the quantized Hall effect in graphene. *Phys. Rev. B*, 73:195408, 2006.

[23] L. Brey and H. A. Fertig. Electronic states of graphene nanoribbons studied with the Dirac equation. *Phys. Rev. B*, 73:235411, 2006.

[24] L. Brillouin. Les électrons libres dans les métaux et le role des réflexions de Bragg. *J. Phys. Radium*, 1:377, 1930.

[25] M. Büttiker. Four-terminal phase-coherent conductance. *Phys. Rev. Lett.*, 57:1761, 1986.

[26] M. Büttiker. Role of quantum coherence in series resistors. *Phys. Rev. B*, 33:3020, 1986.

[27] M. Büttiker. Symmetry of electrical conduction. *IBM J. Res. Dev.*, 32:317, 1988.

[28] M. Büttiker. Quantum coherence and phase randomization in series resistors. In L. Chang, E. Mendez, and C. Tejedor, editors, *Resonant Tunneling in Semiconductors – Physics and Applications*, page 213. Plenum Press, 1991.

[29] T. Can and D. K. Morr. Atomic resolution imaging of currents in nanoscopic quantum networks via scanning tunneling microscopy. *Phys. Rev. Lett.*, 110:086802, 2013.

[30] C. Caroli, R. Combescot, P. Nozieres, and D. Nozieres. Direct calculation of the tunneling currents. *J. Phys. C*, 4:916, 1971.

[31] A. H. Castro Neto, F. Guinea, N. M. R. Peres, K. S. Novoselov, and A. K. Geim. The electronic properties of graphene. *Rev. Mod. Phys.*, 81:109, 2009.

[32] C. J. Cattena, R. A. Bustos-Marún, and H. M. Pastawski. Crucial role of decoherence for electronic transport in molecular wires: Polyaniline as a case study. *Phys. Rev. B*, 82:144201, 2010.

[33] C.-Z. Chang, J. Zhang, X. Feng, J. Shen, Z. Zhang, M. Guo, K. Li, Y. Ou, P. Wei, L.-L. Wang, Z.-Q. Ji, Y. Feng, S. Ji, X. Chen, J. Jia, X. Dai, Z. Fang, S.-C. Zhang, K. He, Y. Wang, L. Lu, X.-C. Ma, and Q.-K. Xue. Experimental observation of the quantum anomalous Hall effect in a magnetic topological insulator. *Science*, 340:167, 2013.

[34] J. G. Checkelsky, J. Ye, Y. Onose, Y. Iwasa, and Y. Tokura. Dirac-fermion-mediated ferromagnetism in a topological insulator. *Nat. Phys.*, 8:729, 2012.

[35] J.-H. Chen, C. Jang, S. Adam, M. S. Fuhrer, E. D. Williams, and M. Ishigami. Charged-impurity scattering in graphene. *Nat. Phys.*, 4:377, 2008.

[36] A. Cresti. Holstein model and Datta model of dephasing in one-dimensional chains. *Ann. Phys.*, 323:2881, 2008.

[37] A. Cresti, R. Farchioni, G. Grosso, and G. P. Parravicini. Keldysh-Green function formalism for current profiles in mesoscopic systems. *Phys. Rev. B*, 68:075306, 2003.

[38] A. Cresti, G. Grosso, and G. Pastori Parravicini. Electronic conductance of one-dimensional chains with phonon dephasing disorder. *J. Phys. Cond. Mat*, 18:10059, 2006.

[39] J. C. Cuevas and E. Scheer. *Molecular Electronics: An Introduction to Theory and Experiment*. World Scientific, 2010.

[40] J. L. D'Amato and H. M. Pastawski. Conductance of a disordered linear chain including inelastic scattering events. *Phys. Rev. B*, 41:7411, 1990.

[41] S. Das Sarma, S. Adam, E. H. Hwang, and E. Rossi. Electronic transport in two-dimensional graphene. *Rev. Mod. Phys.*, 83:407, 2011.

[42] S. Datta. *Electronic Transport in Mesoscopic Systems*. Cambridge University Press, 1997.

[43] S. Datta. *Quantum Transport: Atom to Transistor*. Cambridge University Press, 2005.

[44] S. Datta. *Lessons from Nanoelectronics: A New Perspective on Transport*. World Scientific, 2012.

[45] R. de Picciotto, H. L. Stormer, L. N. Pfeiffer, K. W. Baldwin, and K. W. West. Four-terminal resistance of a ballistic quantum wire. *Nature*, 411:51, 2001.

[46] C. R. Dean, L. Wang, P. Maher, C. Forsythe, F. Ghahari, Y. Gao, J. Katoch, M. Ishigami, P. Moon, M. Koshino, T. Taniguchi, K. Watanabe, K. L. Shepard, J. Hone, and P. Kim. Hofstadter's butterfly and the fractal quantum Hall effect in moire superlattices. *Nature*, 497:598, 2013.

[47] A. Dedigama, D. Deen, S. Murphy, N. Goel, J. Keay, M. Santos, K. Suzuki, S. Miyashita, and Y. Hirayama. Current focusing in InSb heterostructures. *Physica E*, 34:647, 2006.

[48] P. Delplace and G. Montambaux. WKB analysis of edge states in graphene in a strong magnetic field. *Phys. Rev. B*, 82:205412, 2010.

[49] E. V. Deviatov, A. Ganczarczyk, A. Lorke, G. Biasiol, and L. Sorba. Quantum Hall Mach-Zehnder interferometer far beyond equilibrium. *Phys. Rev. B*, 84:235313, 2011.

[50] E. V. Deviatov, A. A. Kapustin, V. T. Dolgopolov, A. Lorke, D. Reuter, and A. D. Wieck. Equilibration between edge states in the fractional quantum Hall effect regime at high imbalances. *Phys. Rev. B*, 74:073303, 2006.

[51] M. Di Ventra. *Electrical Transport in Nanoscale Systems*. Cambridge University Press, 2008.

[52] P. Drude. Zur Elektronentheorie der Metalle. *Ann. Phys.*, 306:566, 1900.

[53] X. Du, I. Skachko, A. Barker, and E. Y. Andrei. Approaching ballistic transport in suspended graphene. *Nat. Nano.*, 3:491, 2008.

[54] S. M.-M. Dubois, A. Lopez-Bezanilla, A. Cresti, F. Triozon, B. Biel, J.-C. Charlier, and S. Roche. Quantum transport in graphene nanoribbons: Effects of edge reconstruction and chemical reactivity. *ACS Nano*, 4:1971, 2010.

[55] E. N. Economou. *Green's Functions in Quantum Physics*. Springer, 2006.

[56] F. Evers and A. D. Mirlin. Anderson transitions. *Rev. Mod. Phys.*, 80:1355, 2008.

[57] D. K. Ferry, S. M. Goodnick, and J. Bird. *Transport in Nanostructures*. Cambridge University Press, 2009.

[58] R. P. Feynman, R. B. Leighton, and M. Sands. *The Feynman Lectures on Physics*, volume 3. Addison-Wesley, 1963.

[59] C. J. B. Ford, S. Washburn, M. Büttiker, C. M. Knoedler, and J. M. Hong. The Hall effect in ballistic junctions. *Surf. Sci.*, 229:298, 1990.

[60] C. J. B. Ford, S. Washburn, R. Newbury, C. M. Knoedler, and J. M. Hong. Resonant suppression of the quantized Hall effect in ballistic junctions. *Phys. Rev. B*, 43:7339, 1991.

[61] S. Frank and D. Jacob. TT 101.10: Orbital dependent absorbing boundary conditions for nanoscale spin transport. In *Verhandlungen der Deutschen Physikalischen Gesellschaft*, 2014.

[62] S. Frank, P. Poncharal, Z. L. Wang, and W. A. de Heer. Carbon nanotube quantum resistors. *Science*, 280:1744, 1998.

[63] K. M. Gaab and C. J. Bardeen. The effects of connectivity, coherence, and trapping on energy transfer in simple light-harvesting systems studied using the Haken-Strobl model with diagonal disorder. *J. Chem. Phys.*, 121:7813, 2004.

[64] F. Gagel and K. Maschke. Influence of dissipation on quantum Hall plateaus. *Phys. Rev. B*, 54:13885, 1996.

[65] F. Gagel and K. Maschke. Influence of potential barriers, disorder and dissipation on the quantum Hall effect. *phys. stat. sol. (b)*, 205:363, 1998.

[66] A. K. Geim. Graphene: Status and prospects. *Science*, 324:1530, 2009.

[67] A. K. Geim and K. S. Novoselov. The rise of graphene. *Nat. Mat.*, 6:183, 2007.

[68] M. C. Geisler, J. H. Smet, V. Umansky, K. von Klitzing, B. Naundorf, R. Ketzmerick, and H. Schweizer. Detection of a Landau band-coupling-induced rearrangement of the Hofstadter butterfly. *Phys. Rev. Lett.*, 92:256801, 2004.

[69] M. E. Gershenson, Y. B. Khavin, A. G. Mikhalchuk, H. M. Bozler, and A. L. Bogdanov. Crossover from Weak to Strong Localization in Quasi-One-Dimensional Conductors. *Phys. Rev. Lett.*, 79:725, 1997.

[70] C. Gesner. *De Omni Rerum Fossilium*. Gesnerus, 1566.

[71] M. O. Goerbig. Electronic properties of graphene in a strong magnetic field. *Rev. Mod. Phys.*, 83:1193, 2011.

[72] R. Golizadeh-Mojarad and S. Datta. Nonequilibrium Green's function based models for dephasing in quantum transport. *Phys. Rev. B*, 75:081301, 2007.

[73] R. Golizadeh-Mojarad and S. Datta. Effect of contact induced states on minimum conductivity in graphene. *Phys. Rev. B*, 79:085410, 2009.

[74] C. González-Santander, F. Domínguez-Adame, M. Hilke, and R. A. Römer. Localisation and finite-size effects in graphene flakes. *EPL*, 104:17012, 2013.

[75] I. V. Gornyi, A. D. Mirlin, and D. G. Polyakov. Interacting electrons in disordered wires: Anderson localization and low-T transport. *Phys. Rev. Lett.*, 95:206603, 2005.

[76] B. Grbić, R. Leturcq, T. Ihn, K. Ensslin, D. Reuter, and A. D. Wieck. Aharonov–Bohm oscillations in p-type GaAs quantum rings. *Physica E*, 40:1273, 2008.

[77] A.-M. Guo and Q.-f. Sun. Spin-selective transport of electrons in DNA double helix. *Phys. Rev. Lett.*, 108:218102, 2012.

[78] V. P. Gusynin, V. A. Miransky, S. G. Sharapov, and I. A. Shovkovy. Edge states, mass and spin gaps, and quantum Hall effect in graphene. *Phys. Rev. B*, 77:205409, 2008.

[79] V. P. Gusynin and S. G. Sharapov. Unconventional integer quantum Hall effect in graphene. *Phys. Rev. Lett.*, 95:146801, Sep 2005.

[80] A. Haque and A. N. Khondker. Electron transport in the presence of random impurities: Transition from ballistic to diffusive regimes. *Phys. Rev. B*, 52:11193, 1995.

[81] M. Z. Hasan and C. L. Kane. *Colloquium*: Topological insulators. *Rev. Mod. Phys.*, 82:3045, 2010.

[82] H. Haugen, A. Brataas, X. Waintal, and G. E. W. Bauer. Focused crossed Andreev reflection. *EPL*, 93:67005, 2011.

[83] P. Hawkins, M. Begliarbekov, M. Zivkovic, S. Strauf, and C. P. Search. Quantum transport in graphene nanoribbons with realistic edges. *J. Phys. Chem. C*, 116:18382, 2012.

[84] T. Heikkilä. *The Physics of Nanoelectronics: Transport and Fluctuation Phenomena at Low Temperatures*. Oxford University Press, 2013.

[85] S. Hershfield. Equivalence of the multilead approach to dephasing and the self-consistent Born approximation. *Phys. Rev. B*, 43:11586, 1991.

[86] J. P. Hobson and W. A. Nierenberg. The statistics of a two-dimensional, hexagonal net. *Phys. Rev.*, 89:662, 1953.

[87] D. R. Hofstadter. Energy levels and wave functions of Bloch electrons in rational and irrational magnetic fields. *Phys. Rev. B*, 14:2239, 1976.

[88] D. R. Hofstadter. *Gödel, Escher, Bach: An Eternal Golden Braid.* Basic Books, 1979.

[89] B. Hunt, J. D. Sanchez-Yamagishi, A. F. Young, M. Yankowitz, B. J. LeRoy, K. Watanabe, T. Taniguchi, P. Moon, M. Koshino, P. Jarillo-Herrero, and R. C. Ashoori. Massive Dirac fermions and Hofstadter butterfly in a van der Waals heterostructure. *Science*, 340:1427, 2013.

[90] T. Ihn. *Semiconductor Nanostructures.* Oxford University Press, 2010.

[91] S. Ihnatsenka and G. Kirczenow. Effect of edge reconstruction and electron-electron interactions on quantum transport in graphene nanoribbons. *Phys. Rev. B*, 88:125430, 2013.

[92] H. Jiang, S. Cheng, Q.-f. Sun, and X. C. Xie. Topological insulator: A new quantized spin Hall resistance robust to dephasing. *Phys. Rev. Lett.*, 103:036803, 2009.

[93] Z. Jiang, Y. Zhang, Y.-W. Tan, H. L. Stormer, and K. Kim. Quantum Hall effect in graphene. *Solid State Commun.*, 143:14, 2007.

[94] Y. S. Joe, S. H. Lee, and E. R. Hedin. Electron transport through asymmetric DNA molecules. *Phys. Lett. A*, 374:2367, 2010.

[95] E. Joos, H. D. Zeh, K. C., D. Giulini, and I.-O. Kupsch, J. Stamatescu. *Decoherence and the Appearance of a Classical World in Quantum Theory.* Springer, 2003.

[96] S. K. Joshi, D. Sahoo, and A. M. Jayannavar. Modeling of stochastic absorption in a random medium. *Phys. Rev. B*, 62:880, 2000.

[97] L. P. Kadanoff and G. Baym. *Quantum Statistical Mechanics.* W. A. Benjamin, 1962.

[98] C. L. Kane and E. J. Mele. Quantum spin Hall effect in graphene. *Phys. Rev. Lett.*, 95:226801, 2005.

[99] I. Kassal and A. Aspuru-Guzik. Environment-assisted quantum transport in ordered systems. *New J. Phys.*, 14:053041, 2012.

[100] M. Katsnelson. *Graphene: Carbon in two dimensions.* Cambridge University Press, 2012.

[101] M. I. Katsnelson. Zitterbewegung, chirality, and minimal conductivity in graphene. *Eur. Phys. J. B*, 51:157, 2006.

[102] L. V. Keldysh. Diagram technique for nonequilibrium processes. *Sov. Phys. JETP*, 20:1018, 1965.

[103] Y. B. Khavin, M. E. Gershenson, and A. L. Bogdanov. Strong localization of electrons in quasi-one-dimensional conductors. *Phys. Rev. B*, 58:8009, 1998.

[104] I. Knittel, F. Gagel, and M. Schreiber. Quantum transport and momentum-conserving dephasing. *Phys. Rev. B*, 60:916, 1999.

[105] M. Knop, U. Wieser, U. Kunze, D. Reuter, and A. D. Wieck. Ballistic rectification in an asymmetric mesoscopic cross junction. *Appl. Phys. Lett.*, 88:082110, 2006.

[106] M. König, S. Wiedmann, C. Brüne, A. Roth, H. Buhmann, L. W. Molenkamp, X.-L. Qi, and S.-C. Zhang. Quantum spin Hall insulator state in HgTe quantum wells. *Science*, 318:766, 2007.

[107] A. Kormányos. Semiclassical study of edge states and transverse electron focusing for strong spin-orbit coupling. *Phys. Rev. B*, 82:155316, 2010.

[108] U. Kuhl and H.-J. Stöckmann. Microwave realization of the Hofstadter butterfly. *Phys. Rev. Lett.*, 80:3232, 1998.

[109] A. Lagendijk, B. van Tiggelen, and D. S. Wiersma. Fifty years of Anderson localization. *Phys. Today*, 62:24, 2009.

[110] R. Landauer. Spatial variation of currents and fields fue to localized scatterers in metallic conduction. *IBM J. Res. Dev.*, 1:223, 1957.

[111] R. Landauer. Electrical transport in open and closed systems. *Z. Phys. B*, 68:217, 1987.

[112] G. Li, A. Luican-Mayer, D. Abanin, L. Levitov, and E. Y. Andrei. Evolution of Landau levels into edge states in graphene. *Nat. Commun.*, 4:1744, 2013.

[113] X.-Q. Li and Y. Yan. Partially coherent tunneling through a series of barriers: Inelastic scattering versus pure dephasing. *Phys. Rev. B*, 65:155326, 2002.

[114] G. Liu, S. Ahsan, A. G. Khitun, R. K. Lake, and A. A. Balandin. Graphene-based non-Boolean logic circuits. *J. Appl. Phys.*, 114:154310, 2013.

[115] J. Maassen, F. Zahid, and H. Guo. Effects of dephasing in molecular transport junctions using atomistic first principles. *Phys. Rev. B*, 80:125423, 2009.

[116] H. C. Manoharan. Topological insulators: A romance with many dimensions. *Nat. Nano.*, 5:477, 2010.

[117] P. C. Martin and J. Schwinger. Theory of many-particle systems. I. *Phys. Rev.*, 115:1342, 1959.

[118] D. Maryenko, F. Ospald, K. v. Klitzing, J. H. Smet, J. J. Metzger, R. Fleischmann, T. Geisel, and V. Umansky. How branching can change the conductance of ballistic semiconductor devices. *Phys. Rev. B*, 85:195329, 2012.

[119] K. Maschke and M. Schreiber. Unified description of coherent and dissipative electron transport. *Phys. Rev. B*, 44:3835, 1991.

[120] K. Maschke and M. Schreiber. Electron transport along a spatially disordered chain in the presence of dissipation. *Phys. Rev. B*, 49:2295, 1994.

[121] M. J. McLennan, Y. Lee, and S. Datta. Voltage drop in mesoscopic systems: A numerical study using a quantum kinetic equation. *Phys. Rev. B*, 43:13846, 1991.

[122] D. L. Miller, K. D. Kubista, G. M. Rutter, M. Ruan, W. A. de Heer, P. N. First, and J. A. Stroscio. Observing the quantization of zero mass carriers in graphene. *Science*, 324:924, 2009.

[123] H. Miyake, G. A. Siviloglou, C. J. Kennedy, W. C. Burton, and W. Ketterle. Realizing the Harper Hamiltonian with laser-assisted tunneling in optical lattices. *Phys. Rev. Lett.*, 111:185302, 2013.

[124] G. Modugno. Anderson localization in Bose–Einstein condensates. *Rep. Prog. Phys.*, 73:102401, 2010.

[125] G. E. Moore. Cramming more components onto integrated circuits. *Electronics*, 38:114, 1965.

[126] F. Muñoz Rojas, D. Jacob, J. Fernández-Rossier, and J. J. Palacios. Coherent transport in graphene nanoconstrictions. *Phys. Rev. B*, 74:195417, 2006.

[127] N. Nagaosa. A new state of quantum matter. *Science*, 318:758, 2007.

[128] K. Nakada, M. Fujita, G. Dresselhaus, and M. S. Dresselhaus. Edge state in graphene ribbons: Nanometer size effect and edge shape dependence. *Phys. Rev. B*, 54:17954, 1996.

[129] K. S. Novoselov, V. I. Fal'ko, L. Colombo, P. R. Gellert, M. G. Schwab, and K. Kim. A roadmap for graphene. *Nature*, 490:192, 2012.

[130] K. S. Novoselov, A. K. Geim, S. V. Morozov, D. Jiang, M. I. Katsnelson, I. V. Grigorieva, S. V. Dubonos, and A. A. Firsov. Two-dimensional gas of massless Dirac fermions in graphene. *Nature*, 438:197, 2005.

[131] K. S. Novoselov, A. K. Geim, S. V. Morozov, D. Jiang, Y. Zhang, S. V. Dubonos, I. V. Grigorieva, and A. A. Firsov. Electric field effect in atomically thin carbon films. *Science*, 306:666, 2004.

[132] K. S. Novoselov, Z. Jiang, Y. Zhang, S. V. Morozov, H. L. Stormer, U. Zeitler, J. C. Maan, G. S. Boebinger, P. Kim, and A. K. Geim. Room-temperature quantum Hall effect in graphene. *Science*, 315:1379, 2007.

[133] D. Nozaki, Y. Girard, and K. Yoshizawa. Theoretical study of long-range electron transport in molecular junctions. *J. Phys. Chem. C*, 112:17408, 2008.

[134] D. Nozaki, C. Gomes da Rocha, H. M. Pastawski, and G. Cuniberti. Disorder and dephasing effects on electron transport through conjugated molecular wires in molecular junctions. *Phys. Rev. B*, 85:155327, 2012.

[135] T. W. Odom, J.-L. Huang, and C. M. Lieber. STM studies of single-walled carbon nanotubes. *J. Phys. Cond. Mat.*, 14:R145, 2002.

[136] V. Oganesyan and D. A. Huse. Localization of interacting fermions at high temperature. *Phys. Rev. B*, 75:155111, 2007.

[137] S. Oh. The complete quantum Hall trio. *Science*, 340:153, 2013.

[138] H. Ohnishi, Y. Kondo, and K. Takayanagi. Quantized conductance through individual rows of suspended gold atoms. *Nature*, 395:780, 1998.

[139] M. G. Pala and G. Iannaccone. Effect of dephasing on the current statistics of mesoscopic devices. *Phys. Rev. Lett.*, 93:256803, 2004.

[140] M. G. Pala and G. Iannaccone. Statistical model of dephasing in mesoscopic devices introduced in the scattering matrix formalism. *Phys. Rev. B*, 69:235304, 2004.

[141] R. Peierls. Zur Theorie der elektrischen und thermischen Leitfähigkeit von Metallen. *Ann. Phys.*, 4:121, 1930.

[142] R. Peierls. Zur Theorie des Diamagnetismus von Leitungselektronen. *Z. Phys.*, 80:763, 1933.

[143] N. M. R. Peres. *Colloquium*: The transport properties of graphene: An introduction. *Rev. Mod. Phys.*, 82:2673, 2010.

[144] H. Petroski. *The Pencil: A History of Design and Circumstances.* Knopf, 1990.

[145] M. B. Plenio and S. F. Huelga. Dephasing-assisted transport: Quantum networks and biomolecules. *New J. Phys.*, 10:113019, 2008.

[146] P. K. Polinák, C. J. Lambert, J. Koltai, and J. Cserti. Andreev drag effect via magnetic quasiparticle focusing in normal-superconductor nanojunctions. *Phys. Rev. B*, 74:132508, 2006.

[147] L. A. Ponomarenko, R. V. Gorbachev, G. L. Yu, D. C. Elias, R. Jalil, A. A. Patel, A. Mishchenko, A. S. Mayorov, C. R. Woods, J. R. Wallbank, M. Mucha-Kruczynski, B. A. Piot, M. Potemski, I. V. Grigorieva, K. S. Novoselov, F. Guinea, V. I. Fal'ko, and A. K. Geim. Cloning of Dirac fermions in graphene superlattices. *Nature*, 497:594, 2013.

[148] R. E. Prange and S. M. Girvin. *The Quantum Hall Effect.* Springer, 1987.

[149] P. Rakyta, A. Kormányos, J. Cserti, and P. Koskinen. Exploring the graphene edges with coherent electron focusing. *Phys. Rev. B*, 81:115411, 2010.

[150] P. Rakyta, A. Kormányos, Z. Kaufmann, and J. Cserti. Andreev edge channels and magnetic focusing in normal-superconductor systems: A semiclassical analysis. *Phys. Rev. B*, 76:064516, 2007.

[151] P. Rebentrost, M. Mohseni, I. Kassal, S. Lloyd, and A. Aspuru-Guzik. Environment-assisted quantum transport. *New J. Phys.*, 11:033003, 2009.

[152] A. A. Reynoso, G. Usaj, and C. A. Balseiro. Magnetic breakdown of cyclotron orbits in systems with Rashba and Dresselhaus spin-orbit coupling. *Phys. Rev. B*, 78:115312, 2008.

[153] J. Rincón, K. Hallberg, A. A. Aligia, and S. Ramasesha. Quantum interference in coherent molecular conductance. *Phys. Rev. Lett.*, 103:266807, 2009.

[154] L. P. Rokhinson, V. Larkina, Y. B. Lyanda-Geller, L. N. Pfeiffer, and K. W. West. Spin separation in cyclotron motion. *Phys. Rev. Lett.*, 93:146601, 2004.

[155] A. Roth, C. Brüne, H. Buhmann, L. W. Molenkamp, J. Maciejko, X.-L. Qi, and S.-C. Zhang. Nonlocal transport in the quantum spin Hall state. *Science*, 325:294, 2009.

[156] D. Roy and A. Dhar. Electron transport in a one dimensional conductor with inelasticscattering by self-consistent reservoirs. *Phys. Rev. B*, 75:195110, 2007.

[157] F. J. Rueß, B. Weber, K. E. J. Goh, O. Klochan, A. R. Hamilton, and M. Y. Simmons. One-dimensional conduction properties of highly phosphorus-doped planar nanowires patterned by scanning probe microscopy. *Phys. Rev. B*, 76:085403, 2007.

[158] T. Schlösser, K. Ensslin, J. P. Kotthaus, and M. Holland. Internal structure of a Landau band induced by a lateral superlattice: A glimpse of Hofstadter's butterfly. *Europhys. Lett.*, 33:683, 1996.

[159] F. Schwierz. Graphene transistors. *Nat. Nano.*, 5:487, 2010.

[160] S.-Q. Shen. *Topological Insulators: Dirac Equation in Condensed Matters*. Springer, 2012.

[161] J. Shi and X. C. Xie. Dephasing and the metal-insulator transition. *Phys. Rev. B*, 63:045123, 2001.

[162] M. M. Shulaker, G. Hills, N. Patil, H. Wei, H.-Y. Chen, H.-S. P. Wong, and S. Mitra. Carbon nanotube computer. *Nature*, 501:526, 2013.

[163] R. H. M. Smit, C. Untiedt, G. Rubio-Bollinger, R. C. Segers, and J. M. van Ruitenbeek. Observation of a parity oscillation in the conductance of atomic wires. *Phys. Rev. Lett.*, 91:076805, 2003.

[164] A. Sommerfeld and H. Bethe. Elektronentheorie der Metalle. In *Handbuch der Physik*, volume 24, pages 333–622. Springer, 1933.

[165] A. M. Song, A. Lorke, A. Kriele, J. P. Kotthaus, W. Wegscheider, and M. Bichler. Nonlinear electron transport in an asymmetric microjunction: A ballistic rectifier. *Phys. Rev. Lett.*, 80:3831, 1998.

[166] T. Stegmann. Kohärenter elektrischer Transport in linearen Quantensystemen – Potentialprofile und *IV*-Charakteristiken. Master's thesis, Universität Duisburg-Essen, 2011.

[167] T. Stegmann, O. Ujsághy, and D. E. Wolf. Decoherence-induced conductivity in the one-dimensional Anderson model. *AIP Conf. Proc.*, 1610:83, 2014.

[168] T. Stegmann, O. Ujsághy, and D. E. Wolf. Localization under the effect of randomly distributed decoherence. *Eur. Phys. J. B*, 87:30, 2014.

[169] T. Stegmann, D. E. Wolf, and A. Lorke. Magnetotransport along a boundary: From coherent electron focusing to edge channel transport. *New J. Phys.*, 15:113047, 2013.

[170] T. Stegmann, M. Zilly, O. Ujsághy, and D. E. Wolf. Statistical model for the effects of phase and momentum randomization on electron transport. *Eur. Phys. J. B*, 85:264, 2012.

[171] A. D. Stone, J. D. Joannopoulos, and D. J. Chadi. Scaling studies of the resistance of the one-dimensional Anderson model with general disorder. *Phys. Rev. B*, 24:5583, 1981.

[172] Y.-W. Tan, Y. Zhang, K. Bolotin, Y. Zhao, S. Adam, E. H. Hwang, S. Das Sarma, H. L. Stormer, and P. Kim. Measurement of scattering rate and minimum conductivity in graphene. *Phys. Rev. Lett.*, 99:246803, 2007.

[173] L. Tapaszto, G. Dobrik, P. Lambin, and L. P. Biro. Tailoring the atomic structure of graphene nanoribbons by scanning tunnelling microscope lithography. *Nat. Nano.*, 3:397, 2008.

[174] T. Taychatanapat, K. Watanabe, T. Taniguchi, and P. Jarillo-Herrero. Electrically tunable transverse magnetic focusing in graphene. *Nat. Phys.*, 9:225, 2013.

[175] D. J. Thouless and S. Kirkpatrick. Conductivity of the disordered linear chain. *J. Phys. C*, 14:235, 1981.

[176] N. Tombros, A. Veligura, J. Junesch, M. H. D. Guimaraes, I. J. Vera-Marun, H. T. Jonkman, and B. J. van Wees. Quantized conductance of a suspended graphene nanoconstriction. *Nat. Phys.*, 7:697, 2011.

[177] M. A. Topinka, B. J. LeRoy, S. E. J. Shaw, E. J. Heller, R. M. Westervelt, K. D. Maranowski, and A. C. Gossard. Imaging coherent electron flow from a quantum point contact. *Science*, 289:2323, 2000.

[178] V. S. Tsoi, J. Bass, and P. Wyder. Studying conduction-electron/interface interactions using transverse electron focusing. *Rev. Mod. Phys.*, 71:1641, 1999.

[179] G. Usaj and C. A. Balseiro. Transverse electron focusing in systems with spin-orbit coupling. *Phys. Rev. B*, 70:041301, 2004.

[180] K. v. Klitzing, G. Dorda, and M. Pepper. New method for high-accuracy determination of the fine-structure constant based on quantized Hall resistance. *Phys. Rev. Lett.*, 45:494, 1980.

[181] H. van Houten, C. W. J. Beenakker, J. G. Williamson, M. E. I. Broekaart, P. H. M. van Loosdrecht, B. J. van Wees, J. E. Mooij, C. T. Foxon, and J. J. Harris. Coherent electron focusing with quantum point contacts in a two-dimensional electron gas. *Phys. Rev. B*, 39:8556, 1989.

[182] B. J. van Wees, H. van Houten, C. W. J. Beenakker, J. G. Williamson, L. P. Kouwenhoven, D. van der Marel, and C. T. Foxon. Quantized conductance of point contacts in a two-dimensional electron gas. *Phys. Rev. Lett.*, 60:848, 1988.

[183] J. Vavro, J. M. Kikkawa, and J. E. Fischer. Metal-insulator transition in doped single-wall carbon nanotubes. *Phys. Rev. B*, 71:155410, 2005.

[184] C. J. O. Verzijl, J. S. Seldenthuis, and J. M. Thijssen. Applicability of the wide-band limit in DFT-based molecular transport calculations. *J. Chem. Phys.*, 138:094102, 2013.

[185] K. Wakabayashi, Y. Takane, M. Yamamoto, and M. Sigrist. Electronic transport properties of graphene nanoribbons. *New J. Phys.*, 11:095016, 2009.

[186] P. R. Wallace. The band theory of graphite. *Phys. Rev.*, 71:622, 1947.

[187] W. Wang and Z. Ma. Edge states and distributions of edge currents in semi-infinite graphene. *Eur. Phys. J. B*, 81:431, 2011.

[188] C. Weeks, J. Hu, J. Alicea, M. Franz, and R. Wu. Engineering a robust quantum spin Hall state in graphene via adatom deposition. *Phys. Rev. X*, 1:021001, 2011.

[189] D. A. Wharam, T. J. Thornton, R. Newbury, M. Pepper, H. Ahmed, J. E. F. Frost, D. G. Hasko, D. C. Peacock, D. A. Ritchie, and G. A. C. Jones. One-dimensional transport and the quantisation of the ballistic resistance. *J. Phys. C*, 21:L209, 1988.

[190] A. Wilson. The theory of electronic semi-conductors. II. *Proc. R. Soc. Lond. A*, 134:277, 1931.

[191] A. H. Wilson. The theory of electronic semi-conductors. *Proc. R. Soc. Lond. A*, 133:458, 1931.

[192] M. Wimmer. *Quantum transport in nanostructures: From computational concepts to spintronics in graphene and magnetic tunnel junctions.* PhD thesis, Universität Regensburg, 2008.

[193] A. Würtz, R. Wildfeuer, A. Lorke, E. V. Deviatov, and V. T. Dolgopolov. Separately contacted edge states: A spectroscopic tool for the investigation of the quantum Hall effect. *Phys. Rev. B*, 65:075303, 2002.

[194] Y. Xing, Q.-f. Sun, and J. Wang. Influence of dephasing on the quantum Hall effect and the spin Hall effect. *Phys. Rev. B*, 77:115346, 2008.

[195] X. Y. Yu, H. Y. Zhang, P. Han, X.-Q. Li, and Y. Yan. Interplay between partial incoherence, partial inelasticity, resonance, and heterogeneity in long-range electron transfer and transport. *J. Chem. Phys.*, 117:2180, 2002.

[196] L. P. Zǎrbo and B. K. Nikolić. Spatial distribution of local currents of massless Dirac fermions in quantum transport through graphene nanoribbons. *EPL*, 80:47001, 2007.

[197] Y. Zhang, Z. Jiang, J. P. Small, M. S. Purewal, Y.-W. Tan, M. Fazlollahi, J. D. Chudow, J. A. Jaszczak, H. L. Stormer, and P. Kim. Landau-level splitting in graphene in high magnetic fields. *Phys. Rev. Lett.*, 96:136806, 2006.

[198] Y. Zhang, Y.-W. Tan, H. L. Stormer, and P. Kim. Experimental observation of the quantum Hall effect and Berry's phase in graphene. *Nature*, 438:201, 2005.

[199] H. Zheng, Z. Wang, Q. Shi, X. Wang, and J. Chen. Statistical model for analyzing the dephasing effects in a one-dimensional scattering chain. *Phys. Rev. B*, 74:155323, 2006.

[200] Y. Zheng and T. Ando. Hall conductivity of a two-dimensional graphite system. *Phys. Rev. B*, 65:245420, 2002.

[201] M. Zilly. *Electronic conduction in linear quantum systems: Coherent transport and the effects of decoherence.* PhD thesis, Universität Duisburg-Essen, 2010.

[202] M. Zilly, O. Ujsághy, M. Woelki, and D. E. Wolf. Decoherence-induced conductivity in the discrete one-dimensional Anderson model: A novel approach to even-order generalized Lyapunov exponents. *Phys. Rev. B*, 85:075110, 2012.

[203] M. Zilly, O. Ujsághy, and D. E. Wolf. Statistical model for the effects of dephasing on transport properties of large samples. *Eur. Phys. J. B*, 68:237, 2009.

[204] M. Zilly, O. Ujsághy, and D. E. Wolf. Conductance of DNA molecules: Effects of decoherence and bonding. *Phys. Rev. B*, 82:125125, 2010.

[205] M. Žnidarič. Dephasing-induced diffusive transport in the anisotropic Heisenberg model. *New J. Phys.*, 12:043001, 2010.

[206] M. Žnidarič and M. Horvat. Transport in a disordered tight-binding chain with dephasing. *Eur. Phys. J. B*, 86:1, 2013.

Danksagung

An erster Stelle danke ich Professor Dietrich E. Wolf für die Betreuung meiner Promotion, für die Möglichkeit auf diesem spannenden Gebiet forschen zu dürfen, für inspirierende und motivierende Diskussionen, sowie für die Ermöglichung zahlreicher Auslandsaufenthalte und Konferenzteilnahmen.

Professor Axel Lorke danke ich für unsere gute Zusammenarbeit, für zahlreiche Diskussionen und für alles, was ich von ihm in den letzten Jahren lernen durfte.

Professor Orsolya Ujsághy danke ich für unsere fruchtbare Zusammenarbeit und für ihre Gastfreundschaft an der Technischen und Wirtschaftswissenschaftlichen Universität in Budapest.

Weiterhin danke ich:

Professor Thomas H. Seligman für seine Gastfreundschaft an der Nationalen Autonomen Universität von Mexiko, für mehrfache Einladungen zu spannenden Workshops in Cuernavaca, sowie für hilfreiche Diskussionen.

Professor Supriyo Datta für seine Gastfreundschaft an der Purdue Universität in West Lafayette und für inspirierende Diskussionen.

Doktor Matías Zilly für hilfreiche Diskussionen zu Beginn meiner Promotion.

Doktor Nikodem Szpak für unsere Diskussionen zu gekrümmten Graphen.

Professor Markus Winterer für seine Hilfsbereitschaft bei der Organisation meiner Auslandsaufenthalte.

Professor Alfred Zawadowski und Mariella Zawadowski für ihre Gastfreundschaft in Budapest.

Meinem Bruder Philipp Stegmann für seine Anmerkungen zum Text.

Doktor Martin Magiera für sein Mathematica-Skript auf dem Rechenserver der AG Wolf.

Doktor Lothar Brendel für physikalische Diskussionen und seine Hilfsbereitschaft bei allen Problemen mit dem Computer.

Der AG Wolf und der AG Lorke für physikalische und nicht-physikalische Gespräche.

Erklärung

Ich versichere, dass ich die von mir vorgelegte Dissertation selbständig angefertigt, die benutzten Quellen und Hilfsmittel vollständig angegeben und die Stellen der Arbeit – einschließlich der Abbildungen –, die anderen Werken im Wortlaut oder dem Sinn nach entnommen sind, in jedem Einzelfall als Entlehnung kenntlich gemacht habe; dass diese Dissertation noch keiner anderen Fakultät oder Universität zur Prüfung vorgelegen hat; dass sie – abgesehen von unten angegebenen Teilpublikationen – noch nicht veröffentlich worden ist sowie, dass ich eine solche Veröffentlichung vor Abschluss des Promotionsverfahrens nicht vornehmen werde. Die Bestimmungen dieser Promotionsordnung sind mir bekannt. Die von mir vorgelegte Dissertation ist von Herrn Professor Dr. Dietrich E. Wolf betreut worden.

Duisburg, den 8. Juli 2014

Teilpublikationen

1. T. Stegmann, O. Ujsághy, D. E. Wolf: *Localization under the effect of randomly distributed decoherence*, Eur. Phys. J. B 87:30 (2014)

2. T. Stegmann, D. E. Wolf, A. Lorke: *Magnetotransport along a boundary: from coherent electron focusing to edge channel transport*, New J. Phys. 15:113047 (2013)

3. T. Stegmann, M. Zilly, O. Ujsághy, D. E. Wolf: *Statistical model for the effects of phase and momentum randomization on electron transport*, Eur. Phys. J. B 85:264 (2012)

4. T. Stegmann, O. Ujsághy, D. E. Wolf: *Decoherence-induced conductivity in the one-dimensional Anderson model*, AIP Conf. Proc. 1610:83 (2014)

Curriculum Vitae

Der Lebenslauf ist in der Online-Version dieser Dissertation aus Gründen des Datenschutzes nicht enthalten.